Energy Conversion and Management: X 30 (2026) 101584

Contents lists available at ScienceDirect

Energy Conversion and Management: X

journal homepage: www.sciencedirect.com/journal/energy-conversion-and-management-x

A quasi-2D multiphase flow proton exchange membrane fuel cell model for efficient distributed cell state prediction

Florian Altmann [a,b,c,*], Dominik Kuzdas [b,f], Dominik Murschenhofer [d], Johanna Bartlechner [c,e], Christoph Hametner [c,e], Stefan Jakubek [c], Stefan Braun [b]

[a] Institute of Applied Physics, TU Wien, Wiedner Hauptstraße 8-10, 1040 Vienna, Austria
[b] Institute of Fluid Mechanics and Heat Transfer, TU Wien, Getreidemarkt 9, 1060 Vienna, Austria
[c] Institute of Mechanics and Mechatronics, TU Wien, Getreidemarkt 9, 1060 Vienna, Austria
[d] German Aerospace Center (DLR), Institute of Engineering Thermodynamics, Pfaffenwaldring 38-40, 70569 Stuttgart, Germany
[e] Christian Doppler Laboratory for Digital Twins for Distributed Parameter Systems, TU Wien, Getreidemarkt 9, 1060 Vienna, Austria
[f] Competence Center Renewable Energy Technologies, University of Applied Sciences Technikum Wien, Giefinggasse 6, 1210 Vienna, Austria

ARTICLE INFO

Keywords:
Dynamic model
Transient response
Non-isothermal effects
Liquid water formation
High computational efficiency

ABSTRACT

To enhance the durability and performance of proton exchange membrane fuel cells, it is essential to capture both spatial and temporal variations of internal states during dynamic operation. While existing reduced-order models (0D/1D) lack spatial resolution, 3D models are often too computationally expensive for transient simulations. To bridge this gap, we present a quasi-2D, time-dependent multiphase model capable of predicting distributed cell states with high computational efficiency. The model accounts for key transport phenomena, including convection, multicomponent diffusion, capillary effects, and membrane water dynamics via electro-osmotic drag and diffusion. It also includes nitrogen crossover, finite-rate sorption/desorption at membrane interfaces, and heat generation from electrochemical reactions, proton conduction, and phase change. A linearisation scheme combined with Chebyshev collocation ensures low computational cost and near real-time capability. Validation against high-resolution 3D computational fluid dynamics simulations confirms the model's accuracy in predicting polarisation curves, gas species distributions, liquid water accumulation, and temperature profiles. Dynamic simulations under load transients further demonstrate its ability to capture key physical processes, underpinning the importance of spatially resolved water transport. By enabling fast and accurate simulations of both steady-state and dynamic fuel cell behaviour, the proposed model supports extensive parametric studies, control system development, and predictive diagnostics. Its computational efficiency makes it a valuable tool for improving fuel cell efficiency, longevity, and system-level control strategies.

1. Introduction

To achieve the targeted climate neutrality in the mobility sector, innovative approaches are necessary. Proton exchange membrane fuel cells (PEMFCs) are a promising technology due to their high energy density combined with high efficiency. However, dynamic operation of a fuel cell (FC) is still very challenging, and the issue of reduced durability and performance arising from unintended destructive operating states is hardly tackled. Over the last decades, water management of FCs was identified to be key in maintaining high performance [1–3]. Increased humidity is appreciated to prevent highly destructive membrane dehydration. However, the uncontrolled formation of liquid water leads to reduced FC efficiency and must therefore be avoided. The temperature distribution within the fuel cell is further crucial, as higher operating temperatures improve chemical reaction kinetics but can also accelerate degradation processes in the catalyst layers (CLs) and the proton exchange membrane (PEM) [4]. Additionally, hygrothermal stresses due to membrane sorption and desorption processes can significantly damage the membrane through elongation and the formation of cracks [5], which further enhances reactant crossover and thereby reduces FC performance.

To address these challenges, model-based control strategies are gaining increased attention. By leveraging physics-informed or data-driven models of the fuel cell system, such approaches enable real-time monitoring and predictive control of critical states such as membrane hydration,

* Corresponding author at: Institute of Applied Physics, TU Wien, Wiedner Hauptstraße 8-10, 1040 Vienna, Austria.
E-mail address: florian.altmann@tuwien.ac.at (F. Altmann).

https://doi.org/10.1016/j.ecmx.2026.101584
Received 4 July 2025; Received in revised form 22 December 2025; Accepted 16 January 2026
Available online 24 January 2026

Nomenclature

Generally, bold symbols and superscript tildes denote vector and dimensional quantities, respectively.

Latin symbols

$\Delta\tilde{S}$	Entropy change [J mol^{-1} K^{-1}]
$\mathscr{J}(s_l)$	Leverett function [−]
$\tilde{m}$	Phase change rate [kg m^{-3} s^{-1}]
$\tilde{\mathscr{D}}$	Binary diffusion coefficient [m^2 s^{-1}]
$\tilde{\mathscr{F}}$	Faraday constant [A s mol^{-1}]
$\tilde{\mathscr{M}}$	Molar mass [kg mol^{-1}]
$\tilde{\mathscr{R}}$	Universal gas constant [J mol^{-1} K^{-1}]
$\tilde{\mathrm{EW}}$	Equivalent weight [kg mol^{-1}]
$\tilde{\mathbf{u}}$	Velocity [m s^{-1}]
$\tilde{c}$	Isobaric specific heat capacity [J kg^{-1}]
$\tilde{D}$	Diffusion coefficient [m^2 s^{-1}]
$\tilde{E}$	Electric potential [V]
$\tilde{E}_{\mathrm{act}}$	Activation energy [J mol^{-1}]
$\tilde{H}$	Height [m]
$\tilde{h}$	Specific enthalpy [J kg^{-1} K^{-1}]
$\tilde{i}$	Current density [A m^{-2}]
$\tilde{j}$	Diffusive mass flux [kg m^{-2} s^{-1}]
$\tilde{k}$	Thermal conductivity [W m^{-1} K^{-1}]
$\tilde{n}$	Amount of substance [mol]
$\tilde{p}$	Pressure [Pa]
$\tilde{q}$	Heat flux [W m^{-2}]
$\tilde{r}$	Enthalpy flux [W m^{-2}]
$\tilde{T}$	Temperature [K]
$\tilde{t}$	Time [s]
$\tilde{W}$	Width [m]
$\tilde{x}$	Spatial coordinate [m]
$\mathbf{A}$	System matrix
$\mathbf{b}$	Right hand side vector
$\mathbf{x}$	Solution vector
C_{drag}	Electro-osmotic drag coefficient [−]
F	Shape/correction factor [−]
f_β	Mass transfer coefficient fitting parameter [−]
f_{PEM1}, f_{PEM2}	Proton conductivity fitting parameter [S m^{-1}]
K	Dimensionless group [−]
N	Number of computational nodes [−]
s	Saturation (= volume fraction) [−]

Greek symbols

α_{red}	Transfer coefficient of the reduction reaction [−]
γ_{C}	Pressure dependency factor [−]
κ_{r}	Relative permeability [−]
λ	Normalised PEM water content [−]
ν	Stoichiometric factor [−]
$\tilde{\alpha}$	Heat transfer coefficient [W m^{-2} K^{-1}]
$\tilde{\beta}$	Mass transfer coefficient [m s^{-1}]
$\tilde{\eta}$	Overpotential due to activation polarisation [V]
$\tilde{\gamma}_{\mathrm{cond}}$	Condensation rate coefficient [s^{-1}]
$\tilde{\gamma}_{\mathrm{evap}}$	Evaporation rate coefficient [s^{-1} Pa^{-1}]
$\tilde{\gamma}_{\mathrm{sorp}}$	Sorption mass transfer coefficient [s^{-1}]
$\tilde{\kappa}$	Permeability [m^2]
$\tilde{\nu}$	Kinematic viscosity [m^2 s^{-1}]
$\tilde{\psi}$	Capillary diffusion flux [kg m^{-2} s^{-1}]
$\tilde{\rho}$	Density [kg m^{-3}]
$\tilde{\sigma}$	Proton conductivity [−]
$\tilde{\theta}_{\mathrm{c}}$	Contact angle [°]

$\tilde{\varsigma}$	Surface tension [N m^{-1}]
ξ	Mass fraction [−]
ζ	Mobility [−]

Subscripts and superscripts

g	Gas
l	Liquid
m	Multiphase mixture
OC	Open circuit
r	Reference
k	Phase
avg	Average
in	Channel inlet
out	Channel outlet

Abbreviations

H_2O	Water
H_2	Hydrogen
N_2	Nitrogen
O_2	Oxygen
ANO	Anode
CAT	Cathode
CFD	Computational fluid dynamics
CL	Catalyst layer
EB	Multiphase mixture energy balance
EOS	Gas phase equation of state
FC	Fuel cell
GC	Gas channel
GDL	Gas diffusion layer
GMB	Gas phase mass balance
LIT	Linearisation in time
LMB	Liquid phase mass balance
MEA	Membrane electrode assembly
MOB	Multiphase mixture momentum balance
PDE	Partial differential equation
PEM	Proton exchange membrane
PEMFC	Proton exchange membrane fuel cell
SL	Inner slice
SMB	Species mass balance in the gas phase
TMB	Multiphase mixture total mass balance

temperature distribution, and reactant flows [6,7]. In particular, model-based control can help mitigate harmful operating conditions by dynamically adjusting appropriate system parameters, thus avoiding membrane dehydration or flooding and maintaining the FC within its optimal efficiency range. Furthermore, advanced distributed parameter observers derived from these models enable the estimation of internal states that are difficult to be measured directly, such as gas species concentrations, membrane water content, and temperature distributions [8,9], thereby facilitating the development of model-based control strategies for mitigating degradation mechanisms during FC operation.

These control strategies rely on sufficiently accurate, yet computationally efficient, models to predict FC behaviour under dynamic conditions. Due to their complexity, currently available 3D computational fluid dynamics (CFD) simulation environments are extremely time-, memory-, and computation-costly, rendering them inefficient and of limited applicability, especially when transient simulations are required. To this end, a FC model based on rational physical grounds is desirable for affordable testing, control unit adjustment, online monitoring, and to perform widespread parameter studies with a minimum of computation effort.

Computationally efficient simulation environments are typically obtained using reduced spatial dimensionality, so-called 0D or quasi-1D models. Amphlett and co-workers were the first to develop a transient model based on simple heat and mass balance equations for a whole PEMFC stack [10]. Several authors followed similar approaches to capture essential FC dynamics [11–13]. However, all of these models neglect the generation and transport of liquid water, which is crucial in many operating scenarios of a PEMFC and to mitigate potential flooding. The efforts of some researchers therefore focused on the development of various reduced-dimensionality models that also incorporate the phase change of water [14–16].

Especially for adequate transient FC simulation, some spatial resolution of liquid water transport is required. Ziegler and co-workers proposed a 1D model that incorporates transport of liquid water in the porous electrodes governed by Darcy's law [17]. Siegel developed a similar model that achieved even real-time simulation capability [18]. Both latter models are isothermal, assume constant gas compositions in the gas channels and

neglect multi-component diffusion in the gas diffusion layers (GDLs). Goshtasbi et al. [19] further refined this approach and proposed a pseudo-2D, transient model of a PEMFC incorporating liquid water transport and non-isothermal effects. The model domain also explicitly accounts for channel-land effects at the interface between the membrane electrode assembly (MEA) and the bipolar plate (BP), but, due to the reduced dimensionality, neglects any spatial variations along the channel. Kang et al. [20] developed a quasi-3D non-isothermal and multiphase model, whereas Kravos [21] and co-workers used a seven regions modelling approach to obtain spatial resolution in both, the MEA and the channels. Their model also accounts for water droplet generation in the latter. However, both models completely neglect diffusive fluxes in the channels, which might become dominant for low stoichiometry or anode dead-end operation.

A different manner that takes into account spatial variations along the channel axis and in the direction of the MEA is the quasi-2D approach introduced by Dannenberg et al. [22]. Here, the gas channels are connected with a number of inner slices for the MEA, each of them treated quasi-1D. Murschenhofer and co-workers [23] utilised this approach to obtain a model for isothermal operating conditions that accounts for effects such as multicomponent diffusion in porous layers, membrane water transport driven by diffusion and electro-osmotic drag as well as membrane nitrogen crossover forced by partial pressure differences. Wang and co-workers [24] utilised a quasi-2D perspective to obtain a model for non-isothermal conditions that also accounts for the generation of liquid water to study the effects of anode-recirculation. However, the explicit numerical solution scheme requires relatively small time-steps that could render the applicability of the model for fuel cell control tasks impractical.

The present work advances the model developed by Murschenhofer and co-workers [23,25] further by incorporating non-isothermal effects and the generation and transport of liquid water — both of which are crucial for capturing cell dynamics and mitigating degradation. Building on the efficient numerical scheme introduced in their work, which combines linearisation-in-time (LIT) with a highly accurate spatial discretisation based on Chebyshev spectral collocation, the present model extends these capabilities while preserving its high computational efficiency. The model is particularly designed for diagnostic applications in real-time control tasks, control unit adjustments, and the design of fuel cell experiments. It fills the gap between highly complex 3D models, which are computationally too expensive for transient simulations, and fast 0D models lacking spatial resolution depth. The intended applications of the model do not require an extremely high spatial resolution of the PEMFC domains in most cases, but only a sufficiently accurate representation of key transport phenomena and their dynamic behaviour to capture critical operating conditions, such as water flooding, membrane dehydration, and strong thermal gradients. The model equations are derived in Section 2 by means of cross-sectional averaging of the relevant quantities, i.e. by a quasi-1D treatment of the integral conservation laws for multiphase heat, mass, and momentum transport in combination with dimensional analysis and rational reasoning based on order of magnitude estimates for all occurring dimensionless groups to reduce the model's complexity. The entire PEMFC model is finally represented by a system of coupled, non-linear partial differential equations (PDEs), which must be solved numerically. The adapted numerical scheme and the structure of the system of equations are presented in Section 3. Finally, the steady-state results for typical polarisation curves as well as distributions of the gas species, liquid water, membrane water, and temperature obtained from the LIT model are validated against the commercial CFD package AVL Fire™ M for relevant operating conditions. Additionally, we report on simulations that have been performed for time dependent PEMFC operation during dynamic cell potential changes. The results are presented in Section 4, followed by conclusions and an outlook in Section 5.

2. Physical–mathematical model

In the following, general assumptions, the modelled domains and their quasi-2D treatment as well as the approaches used to describe various phenomena are presented. Moreover, the principle procedures in the derivation of the model equations are shown. Finally, the coupling of the single domains and the required boundary conditions are presented.

For the entire PEMFC model the governing equations are obtained assuming non-isothermal multiphase flow conditions. In the gas channels and GDLs a mixture of liquid water and multicomponent gas is present. The gas mixture is assumed to be composed of ideal gases and its properties such as viscosity, diffusion coefficients, heat capacity, etc., depend on the gas compositions, i.e. species mass fractions. All material properties are approximated to be constant within the expected operating temperature and pressure ranges during the PEMFC operating states. Furthermore, for low velocities and small temperature differences, which typically occur in FCs, the flow can be treated as incompressible and the gas density depends on the species and temperature distributions only. Both FC channels are supplied with humidified air and H_2 on the cathode and anode sides, respectively. In order to capture the effect of nitrogen accumulation on the anode side due to membrane crossover, N_2 is a further component and consequently multicomponent diffusion is considered on both sides of the PEMFC. Membrane crossover of reactant gases and the GDL's Ohmic resistance are neglected throughout.

2.1. Multiphase quasi-2D approach

To account for the formation and transport of liquid water due to the electrochemical reaction and phase change processes, a multiphase and multicomponent flow description is necessary. To keep the computational cost of dynamic PEMFC simulations low, a quasi-2D multiphase mixture approach [26] is applied in the derivation of the heat, mass, and momentum transport equations. This represents a drastic simplification [27–29], which is, however, justified in view of the anyway limited accuracy demands of the model for FC control tasks and the expected error due to the reduced spatial dimensionality, see also Appendix D. Therefore, the phases are treated as constituents of a single multiphase mixture with density $\tilde{\rho}_\mathrm{m}$ and velocity $\tilde{\mathbf{u}}_\mathrm{m}$,

$$\tilde{\rho}_\mathrm{m} = s_\mathrm{l}\tilde{\rho}_\mathrm{l} + (1 - s_\mathrm{l})\tilde{\rho}_\mathrm{g}\,, \tag{1a}$$

$$\tilde{\rho}_\mathrm{m}\tilde{\mathbf{u}}_\mathrm{m} = s_\mathrm{l}\tilde{\rho}_\mathrm{l}\tilde{\mathbf{u}}_\mathrm{l} + (1 - s_\mathrm{l})\tilde{\rho}_\mathrm{g}\tilde{\mathbf{u}}_\mathrm{g}\,. \tag{1b}$$

For the two phase system present in the PEMFC gas channels and the GDLs, the mixture variables depend on the liquid water saturation s_l, the density $\tilde{\rho}_k$ and velocity $\tilde{\mathbf{u}}_k$ of the liquid and gas phases. In the following, the subscripts $k = \mathrm{g},\mathrm{l}$ represent the gas and liquid phases, whereas subscript $k = \mathrm{m}$ denotes a multiphase mixture variable. Generally, bold faces and superscript tilde denote vector and dimensional quantities, respectively. The modelled spatial domain is obtained from a typical 3D PEMFC geometry by cutting through the channel's symmetry plane, see Fig. 1(a). Further, a quasi-2D approach is applied by considering only the principal directions for gradients of the corresponding variables in each subdomain. The 2D domain is therefore divided into two parallel gas channels connected with a freely selectable number of 'inner slices', each composed of cathode and anode GDLs, catalyst layers and a PEM in between, see Fig. 1(b). For each domain a quasi-1D formulation of the model

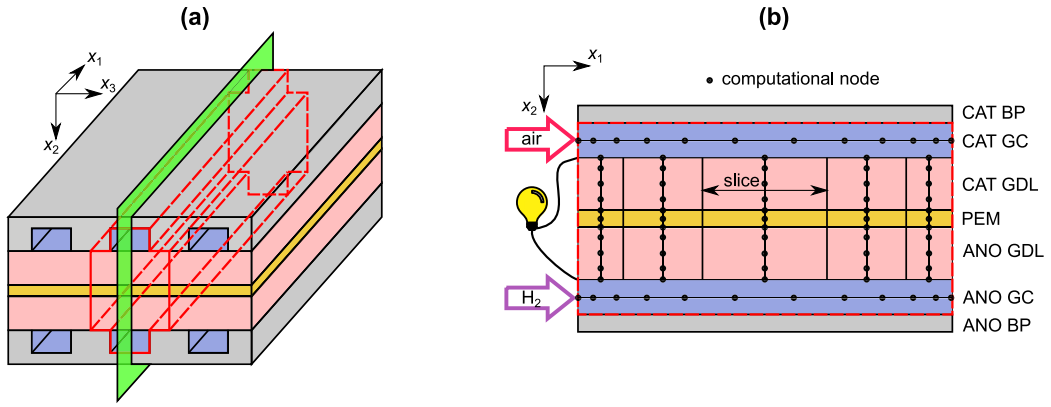

Fig. 1. (a) 3D PEMFC geometry (not to scale) with the modelled (single cell) domain, bounded by red lines and the considered 2D symmetry plane in green. (b) Discretised quasi-2D model domain used in the simulations, Section 3, with $N_{\mathrm{GC}}^{\mathrm{C,A}} = 12$, $N_{\mathrm{GDL}}^{\mathrm{C,A}} = 5$ and $N_{\mathrm{PEM}} = 3$ computation nodes for the gas channels, the GDLs and membrane, respectively, and the number of so-called 'inner slices' $N_{\mathrm{SL}} = 5$. (For interpretation of the references to colour in this figure legend, the reader is referred to the web version of this article.)

equations is derived from the 3D integral conservation laws for the multiphase mixture heat, mass, and momentum transport, Appendix D, and the application of cross-sectional averaging of the relevant variables, e.g. for the velocity profile $\tilde{u}_{\mathrm{m},1}(\tilde{\mathbf{x}},\tilde{t})$ with $\tilde{\mathbf{x}} = (\tilde{x}_1,\tilde{x}_2,\tilde{x}_3)^T$ in a channel,

$$\bar{\tilde{u}}_{\mathrm{m},1}(\tilde{x}_1,\tilde{t}) = \frac{1}{\tilde{W}_{\mathrm{GC}}\tilde{H}_{\mathrm{GC}}}\int_0^{\tilde{W}_{\mathrm{GC}}}\int_0^{\tilde{H}_{\mathrm{GC}}} \tilde{u}_{\mathrm{m},1}(\tilde{\mathbf{x}},\tilde{t})\,\mathrm{d}\tilde{x}_2\,\mathrm{d}\tilde{x}_3\ . \tag{2}$$

Here, $\bar{\tilde{u}}_{\mathrm{m},1}$ is the desired quantity (the multiphase mixture velocity) to be determined, $\tilde{W}_{\mathrm{GC}}\tilde{H}_{\mathrm{GC}}$ is the constant cross-sectional area of the channel and $\tilde{t}$ denotes time. The respective velocity profiles are indicated in Fig. 2 (blue).

Since the gas channel's height and width are typically small compared to its length, $\tilde{H}_{\mathrm{GC}}/\tilde{L}_{\mathrm{GC}} \ll 1$ and $\tilde{W}_{\mathrm{GC}}/\tilde{L}_{\mathrm{GC}} \ll 1$, the species and temperature variations in the $\tilde{x}_2$- and $\tilde{x}_3$-directions are expected to be rather small compared to that along the $\tilde{x}_1$-direction. Hence, for the species mass fractions $\xi_{\mathrm{g}}^{\gamma}$ in the gas phase, and the temperature $\tilde{T}$ we take the respective cross-sectional averaged quantities which depend on the main stream direction $\tilde{x}_1$ only (purple profile in Fig. 2),

$$\xi_{\mathrm{g}}^{\gamma} = \bar{\xi}_{\mathrm{g}}^{\gamma}(\tilde{x}_1,\tilde{t}) \quad \text{and} \quad \tilde{T} = \bar{\tilde{T}}(\tilde{x}_1,\tilde{t})\,. \tag{3}$$

Here, superscript $\gamma = \mathrm{H_2}, \mathrm{O_2}, \mathrm{N_2}, \mathrm{H_2O}$ denotes the gas species on the anode and cathode sides. Because the saturation pressure $\tilde{p}_{\mathrm{sat}}$ depends on $\bar{\tilde{T}}$ only, the liquid-phase saturation s_{l} and all liquid and multiphase mixture variables in the gas channels likewise become functions of $\tilde{x}_1$ only. In contrast, in the MEA $\tilde{x}_2$ is found to be the principal direction for species transport. Summarising, variable changes for the gas channels are only taken into account in $\tilde{x}_1$ direction, whereas in the GDL and PEM variables depend on $\tilde{x}_2$ only. Therefore, 'inner slices' are solely connected via the gas channels.

In addition to convective transport (blue vector in Fig. 2), mass transfer within the gas phase is accounted for by a generalised Fick's law of diffusion [30] (green vector). For the considered three-component gas mixture, two diffusive fluxes for reactants $\alpha = \mathrm{H_2}, \mathrm{O_2}$ and $\mathrm{H_2O}$ in the direction $a = 1,2$ may be written as

$$\begin{aligned}
\tilde{j}_{\mathrm{g},a}^{\alpha} &= -\tilde{\rho}_{\mathrm{g}}\left(\tilde{\mathscr{D}}_{\alpha,\alpha}^{\mathrm{eff}}\frac{\partial \xi_{\mathrm{g}}^{\alpha}}{\partial \tilde{x}_a} + \tilde{\mathscr{D}}_{\alpha,\mathrm{H_2O}}^{\mathrm{eff}}\frac{\partial \xi_{\mathrm{g}}^{\mathrm{H_2O}}}{\partial \tilde{x}_a}\right),\\
\tilde{j}_{\mathrm{g},a}^{\mathrm{H_2O}} &= -\tilde{\rho}_{\mathrm{g}}\left(\tilde{\mathscr{D}}_{\mathrm{H_2O},\alpha}^{\mathrm{eff}}\frac{\partial \xi_{\mathrm{g}}^{\alpha}}{\partial \tilde{x}_a} + \tilde{\mathscr{D}}_{\mathrm{H_2O},\mathrm{H_2O}}^{\mathrm{eff}}\frac{\partial \xi_{\mathrm{g}}^{\mathrm{H_2O}}}{\partial \tilde{x}_a}\right),
\end{aligned} \tag{4}$$

whereas the third flux of $\mathrm{N_2}$ is used to close the system,

$$\tilde{j}_{\mathrm{g},a}^{\alpha} + \tilde{j}_{\mathrm{g},a}^{\mathrm{N_2}} + \tilde{j}_{\mathrm{g},a}^{\mathrm{H_2O}} = 0\,. \tag{5}$$

Here, the effective multicomponent diffusion coefficients $\tilde{\mathscr{D}}_{v,\omega}^{\mathrm{eff}} = [\varepsilon(1-s_{\mathrm{l}})]^q\,\tilde{\mathscr{D}}_{v,\omega}$ account for hindrance effects in structures with porosity ε and the presence of liquid water by the Bruggeman exponent q. The diffusion coefficients of the pure gas mixture $\tilde{\mathscr{D}}_{v,\omega}$ are related to the mass fractions [31], and are computed based on a model for binary diffusion coefficients [32]. Moreover, $\mathrm{H_2}$, $\mathrm{O_2}$ and $\mathrm{N_2}$ are assumed to be insoluble in the liquid phase. Consequently, only one conservation law is required to describe liquid phase mass transport.

The exchange rate of mass between the liquid and the gas phases due to condensation and evaporation depends on the difference between the partial pressure $\tilde{p}^{\mathrm{H_2O}}$ of $\mathrm{H_2O}$, and the temperature dependent saturation pressure $\tilde{p}_{\mathrm{sat}}(\tilde{T})$. The expression for the corresponding source term $\tilde{m}_{\mathrm{l}}$ in the liquid-phase mass-balance equation (C.7) is given by [33],

$$\tilde{m}_{\mathrm{l}} = \left(\tilde{p}^{\mathrm{H_2O}} - \tilde{p}_{\mathrm{sat}}(\tilde{T})\right) f_{\mathrm{sw}}\tilde{\gamma}_{\mathrm{cond}}(1-s_{\mathrm{l}})\frac{\tilde{\mathscr{M}}^{\mathrm{H_2O}}}{\tilde{\mathscr{R}}\tilde{T}} + \left(\tilde{p}^{\mathrm{H_2O}} - \tilde{p}_{\mathrm{sat}}(\tilde{T})\right)(1-f_{\mathrm{sw}})\tilde{\gamma}_{\mathrm{evap}}\tilde{\rho}_{\mathrm{l}}s_{\mathrm{l}} = -\tilde{m}_{\mathrm{g}}^{\mathrm{H_2O}}\ , \tag{6}$$

where $f_{\mathrm{sw}} = \left[1 + \tanh\left(\tilde{p}^{\mathrm{H_2O}} - \tilde{p}_{\mathrm{sat}}(\tilde{T})\right)\right]/2$, a continuous switching function, is introduced to smoothly change between condensation and evaporation. Here, $\tilde{\gamma}_{\mathrm{cond}}$ and $\tilde{\gamma}_{\mathrm{evap}}$ are the corresponding rate coefficients and $\tilde{m}_{\mathrm{g}}^{\mathrm{H_2O}}$ represents the source term for the species mass balance equation (C.6) of gaseous $\mathrm{H_2O}$. A relation proposed as fitting curve by Springer et al. [34] is applied for $\tilde{p}_{\mathrm{sat}}$. The molar mass and the universal gas constant are denoted by $\tilde{\mathscr{M}}$ and $\tilde{\mathscr{R}}$.

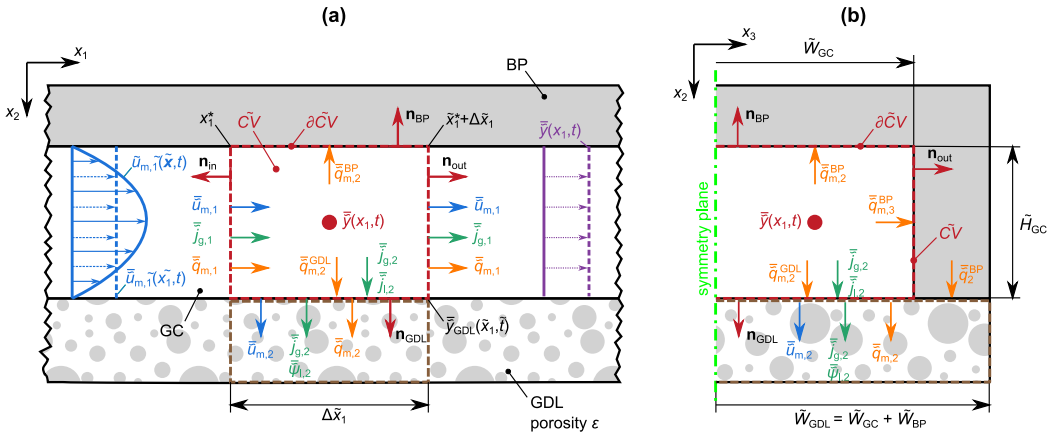

Fig. 2. Schematic of a cathode gas-channel element with adjacent BP and GDL and corresponding normal vectors **n**: (a) along-channel view, (b) cross-section. The mixture velocity profile $\tilde{u}_{\mathrm{m},1}$ and its cross-sectional average are shown in blue. The red dashed rectangle marks the control volume with convective (blue), diffusive (green), and heat (orange) fluxes. The brown rectangle indicates the corresponding GDL-side control volume, with $\bar{\tilde{y}}_{\mathrm{GDL}}$ as the interface value and $\bar{\tilde{q}}_2^{\mathrm{BP}}$ defined in Eq. (54). (For interpretation of the references to colour in this figure legend, the reader is referred to the web version of this article.)

In order to predict the temperature distribution in the PEMFC, the energy conservation of the multiphase mixture is considered. Herein, the heat flux $\tilde{q}_{\mathrm{m}}$ (orange vector in Fig. 2) due to thermal conduction is given by Fourier's law, [35],

$$\tilde{q}_{\mathrm{m},a} = -\tilde{k}_{\mathrm{m}} \frac{\partial \tilde{T}}{\partial \tilde{x}_a} , \tag{7}$$

where $\tilde{k}_{\mathrm{m}}$ represents the thermal conductivity of the mixture. In addition to convection, diffusive energy transport associated with the mass fluxes from Eq. (4) is accounted for by

$$\tilde{r}_{\mathrm{m},a} = \sum_{\gamma} \tilde{h}_{\mathrm{g}}^{\gamma} \tilde{j}_{\mathrm{g},a}^{\gamma} = \left(\tilde{h}_{\mathrm{g}}^{\alpha} - \tilde{h}_{\mathrm{g}}^{\mathrm{N_2}}\right) \tilde{j}_{\mathrm{g},a}^{\alpha} + \left(\tilde{h}_{\mathrm{g}}^{\mathrm{H_2O}} - \tilde{h}_{\mathrm{g}}^{\mathrm{N_2}}\right) \tilde{j}_{\mathrm{g},a}^{\mathrm{H_2O}} , \tag{8}$$

with the specific enthalpies $\tilde{h}_{\mathrm{g}}^{\gamma}$ of the gas species; for details see Appendix C.

2.2. Gas channel model

In the gas channels, homogeneous flow of the multiphase mixture is assumed, with liquid water dispersed as mist in the continuous gas phase, such that $\tilde{\mathbf{u}}_{\mathrm{l}} = \tilde{\mathbf{u}}_{\mathrm{g}} = \tilde{\mathbf{u}}_{\mathrm{m}}$ [26]. Furthermore, the flows in the gas channels turn out to be laminar in general [36] and are assumed to be fully developed locally,

$$\tilde{\mathbf{u}}_{\mathrm{m}}(\tilde{\mathbf{x}}, \tilde{t}) = \tilde{u}_{\mathrm{m},1}(\tilde{\mathbf{x}}, \tilde{t})\, \mathbf{e}_1 , \tag{9}$$

with the unit vector $\mathbf{e}_1 = (1,0,0)^T$, even though mass and energy are exchanged with the GDL, see Fig. 2. The paraboloid like velocity profile, as well as the no-slip condition are assumed to hold throughout, [37].

The derivation of the governing equations for the gas channels is based on the integral formulation of the conservation laws, shown here, e.g., for the conservation of the multiphase mixture mass at the cathode side

$$\int_{\tilde{C}\tilde{V}} \frac{\partial \tilde{\rho}_{\mathrm{m}}}{\partial \tilde{t}} \, \mathrm{d}\tilde{V} + \oint_{\partial \tilde{C}\tilde{V}} \tilde{\rho}_{\mathrm{m}} \tilde{\mathbf{u}}_{\mathrm{m}} \, \mathrm{d}\tilde{S} = 0 . \tag{10}$$

To this end, Eq. (10) is evaluated for the fixed control volume $\tilde{CV}$, depicted in Fig. 2 (red dashed rectangle), and its closed surface $\partial\tilde{CV}$. Using the concept behind Eq. (2), as well as Taylor series expansion about $\tilde{x}_1^*$ in the limit as $\Delta\tilde{x}_1 \to 0$ and by introducing characteristic variables, one finally obtains the continuity equation in dimensionless form:

$$\frac{\partial \rho_{\mathrm{m}}}{\partial t} + \frac{\partial (\rho_{\mathrm{m}} u_{\mathrm{m},1})}{\partial x_1} = -\frac{\tilde{W}_{\mathrm{GDL}} \tilde{L} \tilde{\mathscr{D}}_{\mathrm{O_2,H_2O}}}{\tilde{W}_{\mathrm{GC}} \tilde{H}_{\mathrm{GC}}^2 \tilde{u}_{1,\mathrm{r}}} \varepsilon \rho_{\mathrm{m}} u_{\mathrm{m},2} \Big|_{\mathrm{GDL}} . \tag{11}$$

The term on the right hand side represents the coupling between the gas channel and the GDL as a result of evaluating the integrals at the corresponding interface and ensuring the continuity of the total multiphase mixture mass flux. In an analogous manner, the related conservation laws for the gaseous species and liquid water mass, the multiphase mixture energy and momentum are derived in Appendix D considering the relevant cross-sectional averaged heat and mass fluxes indicated as coloured arrows in Fig. 2. Due to the quasi-2D treatment and the non-isothermal multiphase flow modelling, discontinuities naturally arise in temperature, gas species mass fractions, and liquid phase saturation at the interface between the gas channel and the GDL. To ensure a consistent coupling between the domains, the required jump conditions for the corresponding variables are formulated in accordance with the GDL boundary conditions given in Section 2.6.1.

The mass transport of gaseous species from the gas channel to the GDL is driven by concentration differences between the (cross-sectional averaged) species concentrations in the two adjacent domains, [30],

$$\begin{bmatrix} \bar{\tilde{j}}_{\mathrm{g},2}^{\mathrm{O_2}} \\ \bar{\tilde{j}}_{\mathrm{g},2}^{\mathrm{H_2O}} \end{bmatrix} = \begin{bmatrix} \tilde{\beta}_{\mathrm{O_2,O_2}} & \tilde{\beta}_{\mathrm{O_2,H_2O}} \\ \tilde{\beta}_{\mathrm{H_2O,O_2}} & \tilde{\beta}_{\mathrm{H_2O,H_2O}} \end{bmatrix} \begin{bmatrix} (1-\bar{s}_{\mathrm{l}}) \bar{\tilde{\rho}}_{\mathrm{g}} \bar{\tilde{\xi}}_{\mathrm{g}}^{\mathrm{O_2}} \big|_{\mathrm{GC}} - (1-\bar{s}_{\mathrm{l}}) \bar{\tilde{\rho}}_{\mathrm{g}} \bar{\tilde{\xi}}_{\mathrm{g}}^{\mathrm{O_2}} \big|_{\mathrm{GDL}} \\ (1-\bar{s}_{\mathrm{l}}) \bar{\tilde{\rho}}_{\mathrm{g}} \bar{\tilde{\xi}}_{\mathrm{g}}^{\mathrm{H_2O}} \big|_{\mathrm{GC}} - (1-\bar{s}_{\mathrm{l}}) \bar{\tilde{\rho}}_{\mathrm{g}} \bar{\tilde{\xi}}_{\mathrm{g}}^{\mathrm{H_2O}} \big|_{\mathrm{GDL}} \end{bmatrix} . \tag{12}$$

Table 1
Dimensionless governing equations for the anode and cathode gas channel domains of the PEMFC: total multiphase mixture mass balance (TMB), liquid phase mass balance (LMB), species mass balance in the gas phase of reactant $\alpha = H_2, O_2$ and H_2O (SMB), multiphase mixture energy balance (EB), multiphase mixture momentum balance (MOB), gas equation of state (EOS). The last two equations are the closure conditions for the gas species mass fractions and the multiphase mixture density, respectively. The definitions for the individual dimensionless groups K are given in Appendix B. Here, μ_g denotes the dynamic viscosity of the gas phase; for details see Appendix D.6.

Name	Equation	
TMB	$\partial_t \rho_m + \partial_{x_1}(\rho_m u_{m,1}) = -K_{T1}\,\varepsilon \rho_m u_{m,2}\Big\|_{GDL}$	(15)
LMB	$\partial_t s_l + \partial_{x_1}(s_l u_{m,1}) = K_\rho \dot{m}_l - \left[K_{L1}\,\varepsilon \rho_m u_{m,2} + K_{L2}\,\psi_l\right]\Big\|_{GDL}$	(16)
SMB α	$(1-s_l)\rho_g\left[\partial_t \xi_g^\alpha + u_{m,1}\partial_{x_1}\xi_g^\alpha\right] + K_{S1}\,\partial_{x_1} j_{g,l}^\alpha = \dot{m}_l \xi_g^\alpha - K_{S2}\, j_{g,2}^\alpha\Big\|_{GDL}$	(17)
SMB H_2O	$(1-s_l)\rho_g\left[\partial_t \xi_g^{H_2O} + u_{m,1}\partial_{x_1}\xi_g^{H_2O}\right] + K_{S1}\,\partial_{x_1} j_{g,l}^{H_2O} = \dot{m}_l(\xi_g^{H_2O} - 1) - K_{S2}\, j_{g,2}^{H_2O}\Big\|_{GDL}$	(18)
EB	$\rho_m c_m\left[\partial_t T + u_{m,1}\partial_{x_1} T\right] + K_{E1}\,(1-s_l)\rho_g \xi_g^{H_2O}\left[\partial_t T_{sat} + u_{m,1}\partial_{x_1} T_{sat}\right] + K_{E2}\, j_{g,l}^\alpha \partial_{x_1} T + j_{g,l}^{H_2O}\left[K_{E3}\,\partial_{x_2} T + K_{E4}\,\partial_{x_1} T_{sat}\right] = -(K_{E5} + K_{E6})(T - T_{BP}) - K_{E7}(T - T_{GDL})$	(19)
MOB	$\partial_t(\rho_m u_{m,1}) + F_u \partial_{x_1}(\rho_m u_{m,1}^2) + K_{M1}\,\partial_{x_1} p = K_{M2}\,\partial_{x_1}\left(\mu_g \partial_{x_1} u_{m,1}\right)$	(20)
EOS	$K_{EOS}\,\rho_g \sum_\gamma \frac{\xi_g^\gamma}{\mathscr{M}^\gamma} = p$	(21)
Closure 1	$\xi_g^\alpha + \xi_g^{N_2} + \xi_g^{H_2O} = 1$	(22)
Closure 2	$K_\rho\left[\rho_m - (1-s_l)\rho_g\right] = s_l$	(23)

Here, the mass transfer coefficient is assumed to be of the form $\tilde{\beta}_{v,\omega} = f_\beta\, \tilde{\mathscr{D}}_{v,\omega}/\tilde{H}_{GDL}$ with a fitting parameter f_β to adjust the mass transfer rate across the interface. The flux for N_2 follows from the closure condition (5). The liquid water flux from the gas channel to the GDL,

$$\bar{\bar{j}}_{l,2} = \tilde{\beta}_l \tilde{\rho}_l (\bar{s}\,|_{GC} - \bar{s}\,|_{GDL}), \tag{13}$$

is modelled with a constant mass transfer parameter $\tilde{\beta}_l$ as an additional fitting parameter.

To account for heat transfer between the fluid, the surrounding bipolar plates, and the GDLs, the following relationship is used [35],

$$\tilde{\bar{q}}_{m,i}^{\,j}(\tilde{x}_1, \tilde{t}) = \tilde{\alpha}\left(\tilde{\bar{T}}(\tilde{x}_1, \tilde{t}) - \tilde{T}^j(\tilde{x}_1, \tilde{t})\right) n_i^j\,. \tag{14}$$

Here, $\tilde{\alpha}$ denotes the heat transfer coefficient, n_i^j the outward-pointing normal vector of $\partial \tilde{CV}$ towards the adjacent domain j = BP, GDL in the direction $i = 2, 3$ with the corresponding temperature $\tilde{T}^j$. Due to the high thermal conductivity, the temperature in the bipolar plates is assumed constant in the $\tilde{x}_2$- and $\tilde{x}_3$-direction, providing a boundary condition for Eq. (14). The BP-GC heat fluxes as well as the GC-GDL coupling heat and mass fluxes are depicted in Fig. 2 (coloured vectors) and appear as source terms on the right hand side of the channels' transport equations in Table 1. The relevant dimensionless groups K and the shape factor F_u are defined in Appendices B and D.

2.3. GDL model

Following the gas-channel formulation, the GDLs are treated separately because the presence of the solid porous matrix and the resulting capillary effects introduce additional heat and mass fluxes. The capillary pressure $\tilde{p}_{cap}$ represents the pressure difference between the gas and liquid phases and, in porous materials, depends on the surface tension $\tilde{\zeta}_l$ of liquid water, the contact angle $\tilde{\theta}_c$ of the GDL matrix, the porosity ε, the permeability $\tilde{\kappa}$, and an empirical function $\mathscr{J}(s_l)$ of the liquid saturation s_l [38],

$$\tilde{p}_{cap} = \tilde{p}_l - \tilde{p}_g = \tilde{\zeta}_l \cos(\tilde{\theta}_c)\sqrt{\frac{\varepsilon}{\tilde{\kappa}}}\,\mathscr{J}(s_l)\,. \tag{24}$$

The Leverett $\mathscr{J}$-function has different forms for porous materials that are either hydrophilic ($\tilde{\theta}_c < 90°$), or hydrophobic ($\tilde{\theta}_c > 90°$) [39],

$$\mathscr{J}(s_l) = \begin{cases} 1.417(1-s_l) - 2.120(1-s_l)^2 + 1.263(1-s_l)^3, \\ 1.417 s_l - 2.120 s_l^2 + 1.263 s_l^3, \end{cases} \tag{25}$$

respectively. Driven by a capillary pressure gradient, the capillary diffusion flux $\tilde{\psi}_l$ appears as an additional transport mechanism to convection and multicomponent diffusion. In the multiphase mixture framework the following relationship between the multiphase mixture and individual phase velocities holds [38],

$$\varepsilon s_l \tilde{\rho}_l \tilde{u}_l = \varepsilon \zeta_l \tilde{\rho}_m \tilde{u}_m + \tilde{\psi}_l\,, \tag{26}$$

$$\varepsilon(1-s_l)\tilde{\rho}_g \tilde{u}_g = \varepsilon(1-\zeta_l)\tilde{\rho}_m \tilde{u}_m - \tilde{\psi}_l\,, \tag{27}$$

where ζ_l denotes the mobility of the liquid phase. The capillary flux $\tilde{\psi}_l$ of the liquid phase can then be obtained from a diffusion type equation [38],

$$\tilde{\psi}_{l,2} = -\tilde{\rho}_l \tilde{D}_{cap} \frac{\partial s_l}{\partial \tilde{x}_2} \tag{28}$$

with the capillary diffusion coefficient

$$\tilde{D}_{cap} = -\frac{\tilde{\kappa}}{\tilde{\rho}_l \tilde{\nu}_m} \zeta_l (1-\zeta_l) \frac{\partial \tilde{p}_{cap}}{\partial s_l}\,. \tag{29}$$

Table 2
Dimensionless governing equations for multiphase transport in the GDL domains. Equation names follow Table 1; definitions of K are provided in Appendix B.

Name	Equation	
TMB	$\partial_t \rho_\mathrm{m} + \partial_{x_2}\left(\rho_\mathrm{m} u_{\mathrm{m},2}\right) = 0$	(35)
LMB	$\varepsilon \partial_t s_\mathrm{l} + \varepsilon \partial_{x_2}\left(\zeta_\mathrm{l} \rho_\mathrm{m} u_{\mathrm{m},2}\right) + K_{\mathrm{L1}}\, \partial_{x_2} \psi_{\mathrm{l},2} = \varepsilon \dot{m}_\mathrm{l}$	(36)
SMB α	$\varepsilon \partial_t\left((1-s_\mathrm{l})\rho_\mathrm{g} \xi_\mathrm{g}^{\alpha}\right) + \varepsilon \partial_{x_2}\left((1-\zeta_\mathrm{l})\rho_\mathrm{m} u_{\mathrm{m},2} \xi_\mathrm{g}^{\alpha}\right) + \partial_{x_2} j_{\mathrm{g},2}^{\alpha} - K_{\mathrm{S1}}\, \partial_{x_2}\left(\psi_{\mathrm{l},2}\, \xi_\mathrm{g}^{\alpha}\right) = 0$	(37)
SMB H_2O	$\varepsilon \partial_t\left((1-s_\mathrm{l})\rho_\mathrm{g} \xi_\mathrm{g}^{\mathrm{H_2O}}\right) + \varepsilon \partial_{x_2}\left((1-\zeta_\mathrm{l})\rho_\mathrm{m} u_{\mathrm{m},2} \xi_\mathrm{g}^{\mathrm{H_2O}}\right) + \partial_{x_2} j_{\mathrm{g},2}^{\mathrm{H_2O}} - K_{\mathrm{S1}}\, \partial_{x_2}\left(\psi_{\mathrm{l},2} \xi_\mathrm{g}^{\mathrm{H_2O}}\right) = -\varepsilon \dot{m}_\mathrm{l}$	(38)
EB	$(1-\varepsilon) K_{\mathrm{E1}}\, \partial_t T + \varepsilon \rho_\mathrm{m} c_\mathrm{m}\left[\partial_t T + \gamma_\mathrm{c} u_{\mathrm{m},2} \partial_{x_2} T\right] + K_{\mathrm{E2}}\, \varepsilon \xi_\mathrm{g}^{\mathrm{H_2O}}\left[(1-s_\mathrm{l})\rho_\mathrm{g} \partial_t T_\mathrm{sat} + (1-\zeta_\mathrm{l})\rho_\mathrm{m} u_{\mathrm{m},2} \partial_{x_2} T_\mathrm{sat}\right] = -K_{\mathrm{E3}}\, j_{\mathrm{g},2}^{\alpha} \partial_{x_2} T - j_{\mathrm{g},2}^{\mathrm{H_2O}}\left[K_{\mathrm{E4}}\, \partial_{x_2} T + K_{\mathrm{E2}}\, \partial_{x_2} T_\mathrm{sat}\right] + \psi_{\mathrm{l},2}\left[\left(K_{\mathrm{E5}}\, c_\mathrm{g} - K_{\mathrm{E6}}\right)\partial_{x_2} T + K_{\mathrm{E7}}\, \xi_\mathrm{g}^{\mathrm{H_2O}} \partial_{x_2} T_\mathrm{sat}\right] + K_{\mathrm{E8}}\, \partial_{x_2}(k_\mathrm{m}\, \partial_{x_2} T)$	(39)
MOB	$\partial_t(\rho_\mathrm{m} u_{\mathrm{m},2}) + \partial_{x_2}(\rho_\mathrm{m} u_{\mathrm{m},2}^2) + K_{\mathrm{M1}} \partial_{x_2} p = K_{\mathrm{M2}} \mu_\mathrm{m} u_{\mathrm{m},2} + K_{\mathrm{M3}} \partial_{x_2}\left(\mu_\mathrm{m} \partial_{x_2} u_{\mathrm{m},2}\right)$	(40)
EOS	$K_{\mathrm{EOS}}\, \rho_\mathrm{g} \sum_\gamma \frac{\xi_\mathrm{g}^{\gamma}}{\mathscr{M}^{\gamma}} = p$	(41)
Closure 1	$\xi_\mathrm{g}^{\alpha} + \xi_\mathrm{g}^{\mathrm{N_2}} + \xi_\mathrm{g}^{\mathrm{H_2O}} = 1$	(42)
Closure 2	$K_\rho\left[\rho_\mathrm{m} - (1-s_\mathrm{l})\rho_\mathrm{g}\right] = s_\mathrm{l}$	(43)

Using the definition for the capillary pressure, Eq. (24), the capillary diffusion flux in the porous GDLs finally reads

$$\tilde{\psi}_{\mathrm{l},2} = \frac{\sqrt{\varepsilon \tilde{\kappa}}\, \cos\left(\theta_\mathrm{c}\right)\, \tilde{\zeta}_\mathrm{l}}{\tilde{\nu}_\mathrm{m}} \zeta_\mathrm{l}\left(1-\zeta_\mathrm{l}\right)\, \mathscr{J}'(s_\mathrm{l})\, \frac{\partial s_\mathrm{l}}{\partial \tilde{x}_2}\,, \tag{30}$$

where $\mathscr{J}'(s_\mathrm{l})$ denotes the derivative of the Leverett $\mathscr{J}$-function with respect to s_l.

The kinematic viscosity $\tilde{\nu}_\mathrm{m}$ of the multiphase mixture is a function of the relative permeabilities κ_rl, κ_rg and the kinematic viscosities $\tilde{\nu}_\mathrm{l}$, $\tilde{\nu}_\mathrm{g}$ of the liquid and gas phases, respectively,

$$\tilde{\nu}_\mathrm{m} = \left(\frac{\kappa_\mathrm{rl}}{\tilde{\nu}_\mathrm{l}} + \frac{\kappa_\mathrm{rg}}{\tilde{\nu}_\mathrm{g}}\right)^{-1}. \tag{31}$$

Usually, the relative phase permeability is a function of the liquid water saturation s_l. Here, the following relationship is used [2],

$$\kappa_\mathrm{rl} = s_\mathrm{l}^3 \quad \text{and} \quad \kappa_\mathrm{rg} = (1-s_\mathrm{l})^3\,, \tag{32}$$

from which the mobility of the liquid phase is further obtained,

$$\zeta_\mathrm{l} = \frac{\tilde{\nu}_\mathrm{m}}{\tilde{\nu}_\mathrm{l}} s_\mathrm{l}^3\,. \tag{33}$$

In the energy balance, the solid material of the porous GDL is accounted for in terms of enthalpy accumulation and heat fluxes due to thermal conduction. It is assumed that the GDL's solid material is in thermal equilibrium with the multiphase mixture, i.e. $\tilde{T}_\mathrm{GDL} = \tilde{T}$, such that no heat fluxes appear between the different phases and thermal conduction is solely described by Eq. (7) with a phase-averaged thermal conductivity

$$\tilde{k}_\mathrm{m} = (1-\varepsilon)\tilde{k}_\mathrm{GDL} + \varepsilon\left(s_\mathrm{l}\tilde{k}_\mathrm{l} + (1-s_\mathrm{l})\tilde{k}_\mathrm{g}\right)\,. \tag{34}$$

Analogously to the derivation of the differential form of the governing equations for the gas channel, dimensionless PDEs of the GDL domain can be formulated. These equations are summarised in Table 2.

2.4. Membrane model

The model for the transport of dissolved water within the membrane is adopted from the isothermal model [23] and takes into account electro-osmotic drag, which is proportional to the current density $\tilde{i}$, and diffusion due to gradients in the normalised water content λ, defined as the number of water molecules per sulfonic acid groups present in the polymer, $\lambda = n_{\mathrm{H_2O}}/n_{\mathrm{SO_3H}}$. The total flux of dissolved water therefore is given by

$$\tilde{j}_\mathrm{w} = -\mathscr{M}^{\mathrm{H_2O}}\left(C_\mathrm{drag}(\lambda)\frac{\tilde{i}}{\tilde{\mathscr{F}}} + \frac{\tilde{\rho}_\mathrm{PEM}}{\mathrm{E\tilde{W}}}\tilde{D}_\mathrm{w}(\lambda)\frac{\partial \lambda}{\partial \tilde{x}_2}\right) \tag{44}$$

with the hydration dependent transport coefficients for electro-osmotic drag C_drag and diffusion $\tilde{D}_\mathrm{w}$ as well as the membrane's density $\tilde{\rho}_\mathrm{PEM}$ and equivalent weight $\mathrm{E\tilde{W}}$. Nitrogen permeation is further accounted for by assuming a linear distribution of N_2 across the membrane and the crossover flux $\tilde{j}_\mathrm{cross}^{\mathrm{N_2}}$ appears as a coupling condition at the GDL–PEM interface only; for details see [23].

To incorporate non-isothermal effects in the membrane, an energy balance accounts for the accumulation of energy in the polymer backbone and the dissolved water, as well as energy transport due to the dissolved water fluxes and thermal conduction, Eq. (7). It is assumed that the enthalpy of dissolved water is identical to that of liquid water [40], and that the thermal conductivity of the membrane is a function of the normalised water content, [41],

$$\tilde{k}_\mathrm{PEM}(\lambda) = \left(0.177 + 3.7\times 10^{-3}\lambda\right)\left[\mathrm{W\,m^{-1}\,K^{-1}}\right]\,. \tag{45}$$

Table 3
Dimensionless governing equations of the membrane domain: dissolved water mass balance (DMB) and membrane energy balance (MEB). The definitions for the individual dimensionless groups K are given in Appendix B.

Name	Equation	
DMB	$\partial_t \lambda = K_{D1}\, i\, \partial_{x_2} \lambda + \left(\partial_{x_2} \lambda\right)^2 + \lambda\, \partial_{x_2} \lambda$	(47)
MEB	$\left(1 + K_{E1}\right) \partial_t T - K_{E2}\, i \lambda\, \partial_{x_2} T - \lambda\, \partial_{x_2} \lambda\, \partial_{x_2} T = K_{E3}\, \partial_{x_2} \left(k_{PEM}(\lambda)\, \partial_{x_2} T\right) + K_{E4}\, i^2/\sigma(\lambda)$	(48)

Table 4
Geometrical dimensions and material properties of the PEMFC used in the simulations.

Parameter [unit], source	Symbol	Value
PEMFC length [m]	$\tilde{L}$	0.05
Anode & cathode GC		
Height [m]	$\tilde{H}_{GC}$	4×10^{-4}
Width [m]	$\tilde{W}_{GC}$	8×10^{-4}
Heat transfer coefficient [$\mathrm{W\,m^{-2}\,K^{-1}}$]	$\tilde{\alpha}, \tilde{\alpha}_{GDL}$	500
Anode & cathode GDL		
Height [m]	$\tilde{H}_{GDL}$	2×10^{-4}
Width [m]	$\tilde{W}_{GDL}$	1.6×10^{-4}
Porosity [−]	ε	0.8
Density [$\mathrm{kg\,m^{-3}}$]	$\tilde{\rho}_s$	2000
Bruggeman exponent [−], [23]	q	1.5
Hydraulic permeability [$\mathrm{m^2}$]	$\tilde{\kappa}$	6×10^{-12}
Thermal conductivity [$\mathrm{W\,m^{-1}\,K^{-1}}$]	$\tilde{k}_{GDL}$	0.7
Specific heat capacity [$\mathrm{J\,kg^{-1}\,K^{-1}}$]	$\tilde{c}_{GDL}$	1000
Thermal contact resistance with BP [$\mathrm{m^2\,K\,W^{-1}}$]	$\tilde{R}_{th}$	1×10^{-4}
Contact angle [−]	θ_c	130°
Anode & cathode CL		
Thickness (AVL Fire™) [m]	$\tilde{H}_{CL}$	1×10^{-5}
Activation energy for O_2 reduction on Pt [$\mathrm{J\,mol^{-1}}$], [42]	$\tilde{E}_{act}$	66×10^3
Open circuit potential [V], [42]	$\tilde{E}_{OC}$	1.192
Reference O_2 partial pressure [Pa], [42]	$\tilde{p}_{O_2,r}$	101 250
Reference temperature for $\tilde{i}_0^*$ [K], [42]	$\tilde{T}_{0,r}$	298.15
Membrane		
Thickness [m]	$\tilde{H}_{PEM}$	2×10^{-5}
Density [$\mathrm{kg\,m^{-3}}$]	$\tilde{\rho}_{PEM}$	2000
Equivalent weight [$\mathrm{kg\,mol^{-1}}$]	$\tilde{EW}$	1.1
Water diffusion coefficient at $\tilde{T} = 343.15\,\mathrm{K}$ [$\mathrm{m^2\,s^{-1}}$]	$\tilde{D}_w$	$2.16 \times 10^{-11}\,\lambda$
Electro-osmotic drag coefficient at $\tilde{T} = 343.15\,\mathrm{K}$ [−]	C_{drag}	0.1136λ
Specific heat capacity [$\mathrm{J\,kg^{-1}\,K^{-1}}$]	$\tilde{c}_{PEM}$	1090
Phase change rate coefficients		
Condensation [$\mathrm{s^{-1}}$]	$\tilde{\gamma}_{cond}$	1000
Evaporation [$\mathrm{Pa^{-1}\,s^{-1}}$]	$\tilde{\gamma}_{evap}$	10^{-5}
LIT model fitting parameters		
Reference exchange current density [$\mathrm{A\,m^{-2}}$]	$\tilde{i}_0^*$	0.05
Transfer coefficient [−]	α_{red}	0.525
Pressure dependency coefficient [−]	γ_C	0.7
Ionic conductivity fitting parameter [−]	$f_{PEM1}; f_{PEM2}$	−0.1; 0.125
GC-GDL mass transfer fitting parameter [−]	$f_\beta^C; f_\beta^A$	0.5; 1.0

The generation of Joule heat is accounted for by the source term $\tilde{S}_{PEM} = \tilde{i}^2/\tilde{\sigma}(\lambda)$, in which the proton conductivity $\tilde{\sigma}$ depends linearly on the membrane hydration,

$$\tilde{\sigma} = (f_{PEM1} + f_{PEM2}\lambda) \exp\left(\frac{1286}{303} - \frac{1286\,\mathrm{K}}{\tilde{T}}\right) \left[\mathrm{S\,m^{-1}}\right]. \tag{46}$$

The fitting parameters f_{PEM1} and f_{PEM2} enable the adjustment of the model to a specific FC, by matching the Ohmic potential drop in the electrochemical model, see Section 4 and Table 4.

By means of characteristic reference quantities the dimensionless governing equations for the membrane domain are derived analogue to that of the GDL and summarised in Table 3.

2.5. Electrochemical model

The cell potential $\tilde{E}_{cell}$ is calculated by subtracting the losses from the open cell potential $\tilde{E}_{OC}$,

$$\tilde{E}_{cell} = \tilde{E}_{OC} - \tilde{\eta} - \tilde{i} \int_0^{\tilde{H}_{PEM}} \frac{\mathrm{d}\tilde{x}_2}{\tilde{\sigma}(\lambda)}, \tag{49}$$

where $\tilde{\eta}$ is the overpotential due to activation polarisation in the cathode catalyst layer obtained from the Butler–Volmer equation in the limit of high current densities [42],

$$\tilde{i} = \tilde{i}_0 \exp\left(\frac{\alpha_{red} \tilde{\mathscr{F}} \tilde{\eta}}{\tilde{\mathscr{R}} \tilde{T}}\right), \tag{50}$$

and the rightmost term accounts for the protons' Ohmic resistance in the PEM. The exchange current density $\tilde{i}_0$ is further defined as [42]

$$\tilde{i}_0 = \tilde{i}^*_{0,\mathrm{r}} \left(\frac{\tilde{p}^{\mathrm{O_2}}}{\tilde{p}^{\mathrm{O_2}}_{\mathrm{r}}} \right)^{\gamma_{\mathrm{C}}} \exp\left[-\frac{\tilde{E}_{\mathrm{act}}}{\tilde{\mathscr{R}}\tilde{T}} \left(1 - \frac{\tilde{T}}{\tilde{T}_{0,\mathrm{r}}} \right) \right] . \tag{51}$$

Here, the reference exchange current density $\tilde{i}^*_{0,r}$ (scaled by the electrode roughness), the transfer coefficient α_{red}, and the pressure dependency factor γ_{C} are additional fitting parameters to adjust the polarisation curve of the PEMFC, see also Section 4. The reference values for the O_2 partial pressure and temperature are denoted by $\tilde{p}^{\mathrm{O_2}}_{\mathrm{r}}$ and $\tilde{T}_{0,r}$, respectively, and $\tilde{p}^{\mathrm{O_2}}$ and T denote the corresponding variables of the cathode catalyst layer.

2.6. Coupling & boundary conditions

On the anode and the cathode side, the associated models for the gas channel and GDL represent a system of nine coupled equations, six PDEs and three algebraic equations. Two additional PDEs describe the water transport and the conservation of energy in the membrane. The electrochemical model consists of one transcendental and one algebraic equation. These model equations are valid in different domains and must be merged by appropriate coupling conditions at the corresponding interfaces.

2.6.1. Interface BP-GC-GDL

The quasi-1D GC model inherently accounts for the coupling of mass and heat fluxes at the GC-GDL interface due to the integral formulation of the conservation equations for multiphase mixture mass, liquid phase mass, species and energy. The corresponding mass and heat fluxes appear as source terms in the governing equations of the gas channel in Table 1. For the governing equations of the GDL, one further needs to define boundary conditions that ensure the continuity of the mass and heat fluxes across the interfaces between the bipolar plates, gas channels and GDL that is depicted in Fig. 2. The boundary condition for the liquid phase mass balance is given by

$$\frac{\tilde{W}_{\mathrm{GC}}}{\tilde{W}_{\mathrm{GDL}}} \tilde{j}_{\mathrm{l},2}|_{\mathrm{GC}} = \varepsilon \tilde{\rho}_{\mathrm{m}} \tilde{u}_{\mathrm{m},2} (\zeta_{\mathrm{l}}|_{\mathrm{GDL}} - \zeta_{\mathrm{l}}|_{\mathrm{GC}}) + \tilde{\psi}_{\mathrm{l},2}|_{\mathrm{GDL}} , \tag{52}$$

where $\varepsilon\tilde{\rho}_{\mathrm{m}}\tilde{u}_{\mathrm{m},2}$ represents the convective multiphase mixture flux in the GDL. The subscripts 'GC' and 'GDL' further indicate the variable's corresponding domain, i.e. $\tilde{j}_{\mathrm{l},2}\,|_{\mathrm{GC}}$ is the liquid water flux from the gas channel to the interface, Eq. (13), and $\tilde{\psi}_{\mathrm{l},2}$ is the capillary diffusion flux in the GDL, Eq. (30). Similarly, by applying the continuity of gas species across the interface yields the boundary conditions for the transport of species $\beta = \mathrm{H_2}, \mathrm{O_2}$ and $\mathrm{H_2O}$,

$$\frac{\tilde{W}_{\mathrm{GC}}}{\tilde{W}_{\mathrm{GDL}}} \left[\tilde{j}^{\beta}_{\mathrm{g},2} - \tilde{j}_{\mathrm{l},2} \xi^{\beta}_{\mathrm{g}} \right] |_{\mathrm{GC}} - \left[\tilde{j}^{\beta}_{\mathrm{g},2} - \tilde{\psi}_{\mathrm{l},2} \xi^{\beta}_{\mathrm{g}} \right] |_{\mathrm{GDL}} = \varepsilon \tilde{\rho}_{\mathrm{m}} \tilde{u}_{\mathrm{m},2} \left[(1-\zeta_{\mathrm{l}}) \xi^{\beta}_{\mathrm{g}} |_{\mathrm{GDL}} - (1-\zeta_{\mathrm{l}}) \xi^{\beta}_{\mathrm{g}} |_{\mathrm{GC}} \right] , \tag{53}$$

where $\tilde{j}^{\beta}_{\mathrm{g},2}\,|_{\mathrm{GC}}$ is the diffusive flux defined by Eq. (12).

For the boundary conditions regarding the energy balance, the distribution of heat fluxes in the (x_2, x_3)-plane must be accounted for. One part of the energy flux emitted by the GDL is conducted directly into the BP,

$$\tilde{q}^{\mathrm{BP}}_2 = \frac{1}{\tilde{R}_{\mathrm{th}}} (\tilde{T}_{\mathrm{BP}} - \tilde{T}_{\mathrm{GDL}}) \tag{54}$$

via the thermal contact resistance $\tilde{R}_{\mathrm{th}}$, [43], while the remaining part, together with mass and enthalpy, is transferred to the gas channel. The corresponding boundary condition reads

$$\begin{aligned} &\varepsilon \tilde{\rho}_{\mathrm{m}} \tilde{u}_{\mathrm{m},2} \left(\left[(1-\zeta_{\mathrm{l}}) \tilde{h}_{\mathrm{g}} + \zeta \tilde{h}_{\mathrm{l}} \right] |_{\mathrm{GC}} - \left[(1-\zeta_{\mathrm{l}}) \tilde{h}_{\mathrm{g}} + \zeta \tilde{h}_{\mathrm{l}} \right] |_{\mathrm{GDL}} \right) \\ &+ \frac{\tilde{W}_{\mathrm{GC}}}{\tilde{W}_{\mathrm{GDL}}} \left[\tilde{r}_{\mathrm{m},2} + \tilde{j}_{\mathrm{l},2} (\tilde{h}_{\mathrm{l}} - \tilde{h}_{\mathrm{g}}) + \tilde{q}^{\mathrm{GDL}}_{\mathrm{m},2} \right] |_{\mathrm{GC}} + \frac{\tilde{W}_{\mathrm{BP}}}{\tilde{W}_{\mathrm{GDL}}} \tilde{q}^{\mathrm{BP}}_2 = \left[\tilde{r}_{\mathrm{m},2} + \tilde{\psi}_{\mathrm{l},2} (\tilde{h}_{\mathrm{l}} - \tilde{h}_{\mathrm{g}}) + q_{\mathrm{m},2} \right] |_{\mathrm{GDL}} . \end{aligned} \tag{55}$$

Although a quasi-2D description is used, different gas channel and GDL widths in the x_3-direction, see Figs. 1(a) and 2, can be taken into account.

2.6.2. Interface GDL - membrane

The GDL–PEM interface forms the principal junction where transport phenomena in the porous electrodes and membrane couple to the electrochemical reactions in the catalyst layer. Due to their relative thickness, the catalyst layers are treated as vanishingly thin, and the electrochemical source terms are therefore applied at the GDL–membrane interface. The coupling conditions are formulated using the conservation of total species and heat fluxes, assuming that there is no convective flow through the PEM. The specific coupling conditions read:

$$\begin{aligned} \text{cathode:}\quad & \tilde{j}^{\mathrm{O_2}}_{\mathrm{g,tot}} = \frac{\tilde{i} \tilde{\mathscr{M}}^{\mathrm{O_2}}}{4\tilde{\mathscr{F}}} , \quad \tilde{j}^{\mathrm{N_2}}_{\mathrm{g,tot}} = \tilde{j}^{\mathrm{N_2}}_{\mathrm{cross}} , \\ & \tilde{j}^{\mathrm{H_2O}}_{\mathrm{g,tot}} = (1-s_{\mathrm{l}}) \left(\tilde{j}_{\mathrm{w}} - \frac{i \tilde{\mathscr{M}}^{\mathrm{H_2O}}}{2\tilde{\mathscr{F}}} \right) , \\ & \tilde{j}_{\mathrm{l,tot}} = s_{\mathrm{l}} \left(\tilde{j}_{\mathrm{w}} - \frac{i \tilde{\mathscr{M}}^{\mathrm{H_2O}}}{2\tilde{\mathscr{F}}} \right) , \\ \text{anode:}\quad & \tilde{j}^{\mathrm{H_2}}_{\mathrm{g,tot}} = -\frac{i \tilde{\mathscr{M}}^{\mathrm{H_2}}}{2\tilde{\mathscr{F}}} , \quad \tilde{j}^{\mathrm{N_2}}_{\mathrm{g,tot}} = \tilde{j}^{\mathrm{N_2}}_{\mathrm{cross}} , \\ & \tilde{j}^{\mathrm{H_2O}}_{\mathrm{g,tot}} = (1-s_{\mathrm{l}}) \tilde{j}_{\mathrm{w}} , \quad \tilde{j}_{\mathrm{l}} = s_{\mathrm{l}} \tilde{j}_{\mathrm{w}} . \end{aligned} \tag{56}$$

Here, the total mass flux of gaseous species γ is given by $\tilde{j}^{\gamma}_{\mathrm{g,tot}} = \varepsilon(1-\zeta_{\mathrm{l}}) \tilde{\rho}_{\mathrm{m}} \tilde{u}_{\mathrm{m},2} \xi^{\gamma}_{\mathrm{g}} + \tilde{j}^{\gamma}_{\mathrm{g},2} - \tilde{\psi}_{\mathrm{l},2} \xi^{\gamma}_{\mathrm{g}}$ and the total mass flux of liquid water is $\tilde{j}^{\alpha}_{\mathrm{l,tot}} = \varepsilon \zeta_{\mathrm{l}} \tilde{\rho}_{\mathrm{m}} \tilde{u}_{\mathrm{m},2} + \tilde{\psi}_{\mathrm{l},2}$. The N_2 crossover flux $j^{\mathrm{N_2}}_{\mathrm{cross}}$ through the membrane is defined in [23]. For the coupling of the energy balance one finds for either side:

$$\varepsilon \tilde{\rho} \tilde{u}_{\mathrm{m},2} (\zeta \tilde{h}_{\mathrm{l}} + (1-\zeta) \tilde{h}_{\mathrm{g}}) + \tilde{\psi}_{\mathrm{l},2} (\tilde{h}_{\mathrm{l}} - \tilde{h}_{\mathrm{g}}) + \tilde{r}_{\mathrm{m},2} + \tilde{q}_{\mathrm{m},2} = \tilde{j}_{\mathrm{w}} \tilde{h}_{\mathrm{l}} + \tilde{q}_{\mathrm{PEM},2} - \tilde{S}^{\mathrm{C/A}}_{\mathrm{CL}} , \tag{57}$$

where $\tilde{q}_{\mathrm{PEM},2}$ is the Fourier heat flux in the membrane. The source terms at the interface are given by

$$\begin{aligned}\tilde{S}^{\mathrm{C}}_{\mathrm{CL}} &= \frac{\tilde{\mathscr{M}}^{\mathrm{H_2O}}\tilde{i}}{2\tilde{\mathscr{F}}}\,\tilde{h}_{\mathrm{l}} - \frac{\tilde{\mathscr{M}}^{\mathrm{O_2}}\tilde{i}}{4\tilde{\mathscr{F}}}\,\tilde{h}_{\mathrm{g}}^{\mathrm{O_2}} - \frac{\tilde{i}}{2\mathscr{F}}\,\tilde{T}\Delta\tilde{S}^{\mathrm{C}} + \tilde{i}\tilde{\eta}\,,\\ \tilde{S}^{\mathrm{A}}_{\mathrm{CL}} &= \frac{\tilde{\mathscr{M}}^{\mathrm{H_2}}\tilde{i}}{2\tilde{\mathscr{F}}}\,\tilde{h}_{\mathrm{g}}^{\mathrm{H_2}}\,.\end{aligned} \tag{58}$$

Both catalyst layer source terms account for the consumption and generation of species enthalpy by the electrochemical reaction. Additionally, on the cathode side, the release of heat due to the reaction entropy $\Delta\tilde{S}^{\mathrm{C}}$ and the overpotential $\tilde{\eta}$ from activation polarisation losses, Eq. (50), is considered.

For the formulation of the membrane boundary conditions a non-equilibrium model for H_2O at the GDL–PEM interface is chosen. The water flux $\tilde{j}_{\mathrm{sorp}}$ due to sorption or desorption processes of the membrane is assumed to be proportional to the difference between the actual membrane water content λ and the value at its equilibrium state λ_{eq} [44],

$$\tilde{j}_{\mathrm{sorp}} = \frac{\tilde{\mathscr{M}}^{\mathrm{H_2O}}\tilde{\rho}_{\mathrm{PEM}}}{\mathrm{E\tilde{W}}}\tilde{\gamma}_{\mathrm{sorp}}\left(\lambda_{\mathrm{eq}} - \lambda\right). \tag{59}$$

Here, $\tilde{\gamma}_{\mathrm{sorp}}$ represents the mass transfer coefficient for the sorption–desorption process. It depends on the membrane water content and the temperature at the interface; for details see [44]. The equilibrium water content λ_{eq} depends on the water activity $a_{\mathrm{w}} = \tilde{p}^{\mathrm{H_2O}}/\tilde{p}_{\mathrm{sat}} + 2s_{\mathrm{l}}$ and is obtained from the relation [2]

$$\lambda_{\mathrm{eq}} = \begin{cases} 0.043 + 17.81a_{\mathrm{w}} - 39.85a_{\mathrm{w}}^2 + 36.0a_{\mathrm{w}}^3\,, & a_{\mathrm{w}} < 1\,,\\ 12.6 + 1.4a_{\mathrm{w}}\,, & 1 \le a_{\mathrm{w}} < 3\,,\\ 16.8\,, & a_{\mathrm{w}} \ge 3\,,\end{cases} \tag{60}$$

and therefore is a function of the water partial pressure $\tilde{p}^{\mathrm{H_2O}}$ and liquid water saturation s_{l}.

For the evaluation of the energy balance, thermal equilibrium between the GDL and the PEM is assumed. Therefore, the temperature computed from Eq. (57) is prescribed as a Dirichlet condition to the PEM boundaries.

2.6.3. Boundary conditions

Various interchangeable PEMFC operating modes can be simulated with the present model by applying different sets of boundary conditions. In terms of mass transport, either pressure or mass-driven operation is possible, prescribing the inlet pressure $\tilde{p}_{\mathrm{in}}$ or the gas channel inlet velocity $\tilde{u}^{\mathrm{in}}_{\mathrm{m},1}$. The outlet pressure $\tilde{p}_{\mathrm{out}}$ is set as a boundary condition in both cases. Furthermore, a stoichiometry operation mode is implemented that applies an inlet reactant mass flux that is ν_i times the flux consumed in the respective half cell $i = \mathrm{C}, \mathrm{A}$. In the energy balance, a Dirichlet boundary condition for the inlet temperature is applied. Depending on the inlet temperature and pressure, the gas phase mass fractions $\tilde{\xi}^{\alpha}_{\mathrm{g}}$ are determined according to the desired gas relative humidity ($\mathrm{RH_{in}}$) with $s_{\mathrm{l}} = 0$. The bipolar plate temperature is further set constant in x_1-direction to mimic an ideal cooling system. All these settings are applicable to both co- and counter-flow operation modes of the PEMFC. In all cases, a Neumann condition sets the diffusive mass fluxes to zero at the respective channel outlet. Further, the dead-end operation of the anode can be simulated by replacing the pressure outlet boundary condition $\tilde{p}_{\mathrm{out}}$ with a fixed outlet velocity $\tilde{u}^{\mathrm{out}}_{\mathrm{l,m}} = 0$. Deliberate dynamic switching between these boundary conditions further allows to replicate N_2 purging scenarios. For the electrochemical model, both current and voltage driven operation is possible. For the latter, a uniform cell potential distribution $\tilde{E}_{\mathrm{cell}}$ is applied to the catalyst layers. For current driven mode one additional equation,

$$\tilde{i}_{\mathrm{avg}}(\tilde{t}) = \frac{1}{\tilde{L}}\int_0^{\tilde{L}} \tilde{i}(\tilde{x}_1, \tilde{t})\,\mathrm{d}\tilde{x}_1\,, \tag{61}$$

is introduced to provide a closure for the current density distribution in the inner slices of the GDL. Here, the boundary condition is the average cell current density $\tilde{i}_{\mathrm{avg}}$.

3. Numerical treatment

To solve the system of coupled nonlinear model equations, the same numerical treatment is used that was developed for the isothermal case, [23]. The solution method is based on a Chebyshev spectral collocation method that discretises the spatial domain with a Gauss–Lobatto grid, thereby providing high accuracy with a comparatively small number of computation nodes [45]. The time derivatives are approximated by an upwind finite difference scheme of second order accuracy, which is capable of adaptive time stepping [46]. To avoid numerically expensive Newton iterations, the governing equations to be solved at time step t_k are linearised with respect to the previous time step t_{k-1} [47], which finally yields a system of linear equations of the form

$$\mathbf{A}(\mathbf{x}_{k-1}, \mathbf{x}_{k-2}, \mathbf{x}_{k-3}, \mathbf{y}_k)\mathbf{x}_k = \mathbf{b}(\mathbf{x}_{k-1}, \mathbf{x}_{k-2}, \mathbf{x}_{k-3}, \mathbf{y}_k)\,, \tag{62}$$

for the entire PEMFC model. Here, the system matrix $\mathbf{A}$ and the right-hand side vector $\mathbf{b}$ depend on the solution vectors $\mathbf{x}_k = \mathbf{x}(t_k)$ of the three previous time steps t_{k-1}, t_{k-2} and t_{k-3}. For transient simulations, the system (62) is solved at each time step t_k implicitly. The components of the vector $\mathbf{x}$ represent the unknown variables at the collocation points mentioned in Section 2. In the GCs and the GDL, these variables are the multiphase mixture velocity $u_{\mathrm{m},a}$, the gas mass fractions $\xi_{\mathrm{g}}^{\mathrm{O_2}}$, $\xi_{\mathrm{g}}^{\mathrm{H_2}}$, $\xi_{\mathrm{g}}^{\mathrm{N_2}}$, $\xi_{\mathrm{g}}^{\mathrm{H_2O}}$, the pressure p, the gas density ρ_{g}, the temperature T, and the density of the multiphase mixture ρ_{m}. In the PEM the unknowns are the dissolved water content λ and the temperature T, as well as the equilibrium water contents λ_{eq} at the GDL–PEM interfaces. The input vector $\mathbf{y}_k = \mathbf{y}(t_k)$ contains the imposed boundary conditions mentioned in Section 2.6.3.

To reduce the linearisation effort, at each time step the liquid phase mass balance equations (16) and (D.12) are solved separately in $\mathbf{A}_{\mathrm{l}}\mathbf{x}_{\mathrm{l}} = \mathbf{b}_{\mathrm{l}}$, prior to solving the remaining governing equations. The vector $\mathbf{x}_{\mathrm{l}}$ contains s_{l} as the only variable at each grid point. The rather sluggish water dynamics justify s_{l} to be treated as a known parameter in the subsequent solution of Eq. (62). The dimension $N_A \times N_A$ of the square matrix $\mathbf{A}$ is given by

$$N_A = 8\left(N^{\mathrm{C}}_{\mathrm{GC}} + N^{\mathrm{A}}_{\mathrm{GC}}\right) + N_{\mathrm{SL}}\left[8\left(N^{\mathrm{C}}_{\mathrm{GDL}} + N^{\mathrm{A}}_{\mathrm{GDL}}\right) + 2\,N_{\mathrm{PEM}} + 4\right] + \delta_{\mathrm{i/u}}\,, \tag{63}$$

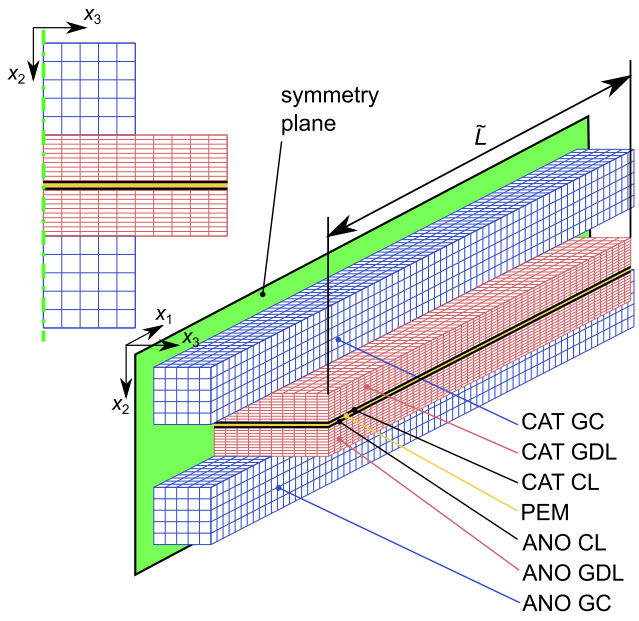

Fig. 3. Computational domain used for 3D PEMFC simulations in AVL Fire™ M with a total number of 28 500 cells. (For interpretation of the references to colour in this figure legend, the reader is referred to the web version of this article.)

where N_{GC}, N_{GDL}, N_{PEM} denote the number of computational nodes in the corresponding domains, N_{SL} is the number of inner slices, and $\delta_{i/u} = 0$ for voltage driven mode and $\delta_{i/u} = 1$ for current driven mode. The latter is due to the one additional Eq. (61) for the cell current boundary condition. The factors 8 and 2 correspond to the number of variables in the gas channels, GDLs and PEM, respectively. Additionally, the equilibrium water content λ_{eq} of the cathode and anode GDL–PEM interface, as well as the activation overpotential η and the current density i, calculated from the electrochemical model, appear as slice variables. The dimension of the system of equations for the liquid water transport model is $N_{A_l} = N_{GC}^{C} + N_{GC}^{A} + N_{SL}\left(N_{GDL}^{C} + N_{GDL}^{A}\right)$. For the exemplary discretisation with $N_{GC} = 12$, $N_{GDL} = 5$, $N_{PEM} = 3$ and $N_{SL} = 5$, shown in Fig. 1 that is further used to validate the current LIT model, the matrix $\mathbf{A}$ is of dimension $N_A \times N_A = 642^2$ ($N_{A_l} \times N_{A_l} = 74^2$) with a sparsity of 0.967 (0.793).

To avoid nonlinearities appearing in the computation of material parameters, such as diffusion coefficients, phase mobility, or heat capacity, these are calculated from the previous time step variables. This substantial simplification is justified with the relatively small material property alterations that occur in the typical temporal operating behaviour of a PEMFC. In contrast to the model for isothermal conditions, the equilibrium water content is solved in an implicit fashion in order to improve numerical stability during highly dynamic simulations.

4. Validation and discussion

The LIT model presented here is implemented in MATLAB® [48] and validated against high resolution 3D CFD simulations using the fuel cell package of the commercially available software AVL Fire™ M R2023.1 [49]. A detailed description of the 3D CFD model, including the governing equations, source terms, and boundary conditions, can be found in the work of Fink et al. [50]. This well-established model was validated and tested against measurement data in numerous works, including [51,52], proving its predictive power over a wide range of operating conditions. Overall predictive capabilities of the current LIT model are presented in terms of polarisation curves. The accuracy of spatial distributions of gas species, liquid water, membrane water content and cell temperature is discussed for selected steady-state operating points. To investigate the transient behaviour of the LIT model, the responses of current density, liquid water saturation and temperature to changes in the cell potential are analysed.

The geometrical domain is described in a quasi-2D manner for the LIT model, displayed in Fig. 1(b). The number of computational nodes, Section 3, was chosen based on a grid convergence study that resulted in this discretisation as the best compromise between achieved accuracy (finer grid resolutions lead to insignificant accuracy enhancements) and computation time. The computational grid for the AVL Fire™ M simulations is shown in Fig. 3. A straight channel geometry similar to [53] is implemented. However, the gas channel inlets are straight, and the geometry of the anode and cathode gas channels is adapted to have equal dimensions. By using the green symmetry plane along the channel length, the number of cells is halved, and the computational effort is significantly reduced.

To validate the prediction capabilities of the LIT model and its underlying assumptions, the simulations performed with AVL Fire™ are also based on non-isothermal conditions and take into account liquid water formation, liquid water transport and membrane gas crossover for all species. Mass flows into the FC are described by stoichiometric flow, therefore the boundary condition for the gas channel inlet velocity is prescribed as

$$\tilde{u}_{m,1}^{in} = \nu \frac{\tilde{L}\,\tilde{W}_{GDL}}{\tilde{H}_{GC}\,\tilde{W}_{GC}} \frac{\mathscr{M}^{\alpha}\,\tilde{I}_{avg}}{n\,\mathscr{F}\,\tilde{\rho}_{g}^{in}\,\xi_{g}^{in}}, \tag{64}$$

where ν denotes the stoichiometry factor and $n = 2, 4$ on the anode and cathode side, respectively. The inlet gas composition is defined by a constant relative humidity RH_{in} of the air and H_2 gas. At the channel outlets a constant pressure boundary condition is prescribed and co-flow operation is used for all simulations. For the gas inlet and all surfaces in contact with the bipolar plate (gas channels and GDL), a constant temperature

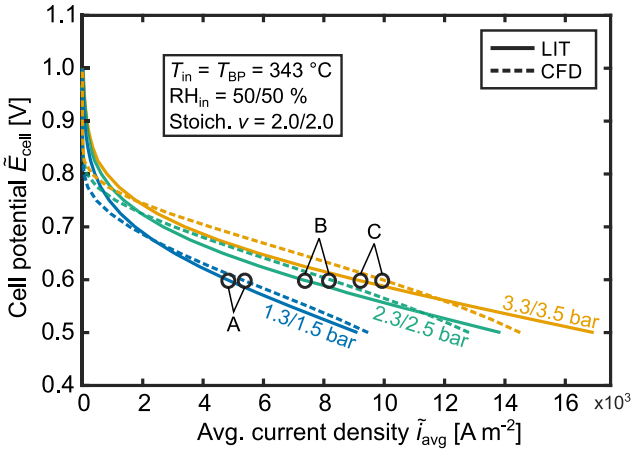

Fig. 4. Polarisation curves computed by the CFD and LIT models. The green lines represent the fitted benchmark case for $\tilde{p}_{out}$ = 2.3/2.5 bar at the cathode/anode side, the blue and orange lines show the LIT model's predictive capability for different operating pressures $\tilde{p}_{out}$ = 2.3/2.5 bar and $\tilde{p}_{out}$ = 3.3/3.5 bar, respectively. The black circles indicate the specific operating points studied in the validation of the LIT model in terms of gas species, Fig. 5, liquid water, Fig. 6(a), membrane water, Fig. 6(b), and temperature distributions, Fig. 7. (For interpretation of the references to colour in this figure legend, the reader is referred to the web version of this article.)

$\tilde{T}_{in} = \tilde{T}_{BP}$ = 70 °C is prescribed, assuming sufficient temperature control of the fuel cell. The considered effects of the non-isothermal, multi-phase AVL Fire™ M model include multi-component diffusion via Maxwell–Stefan diffusion through porous media, transport of liquid and gaseous species in the ionomer phase and three-phase enthalpy transport [50].

As far as applicable, geometrical dimensions, material properties and transport coefficients are equal in both software environments except for the electrochemical parameters explicitly referred to as fitting parameters (see Section 2.5) which are varied to adjust the LIT model results to that obtained by AVL Fire™. However, if different models are used to describe certain physical phenomena, also transport coefficients may differ. Furthermore, the parameters f_β and $\tilde{\rho}_l$ for the GC-GDL mass transfer, as well as the phase change rates $\tilde{\gamma}_{evap}$ and $\tilde{\gamma}_{cond}$, appear only in the LIT model, due to the simplified description of the GC-GDL interface and liquid–gas interphase mass transfer. The geometric dimensions and material properties used in the simulations are summarised in Table 4.

A benchmark polarisation curve is established with AVL Fire™ simulations, by altering the cell potential from 1.0 V to 0.5 V in steps of 0.025 V. At the cathode/anode side of the PEMFC the values for the inlet relative humidity and outlet pressure were held constant at RH_{in} = 50/50 % and $\tilde{p}_{out}$ = 2.3/2.5 bar, respectively. Stoichiometry operation was used with stoichiometric factor ν = 2.0 for both sides.

To obtain an appropriate reference polarisation curve from the LIT model, the fitting parameters of the electrochemical model presented in Section 2.5 were adjusted using MATLAB®'s particle swarm optimisation algorithm [54]. The objective function was the root mean square error between the 3D CFD benchmark polarisation curve and the polarisation curve generated by the LIT model. To enhance the computational efficiency of the fitting procedure, MATLAB®'s Parallel Computing Toolbox [48] was utilised, enabling multiple LIT simulations to be performed simultaneously. For the generation of a polarisation curve with the LIT model, the cell potential was varied in steps of 0.1 V from 1.0 V to 0.5 V. The current density values used for the polarisation curve were recorded ensuring that a steady state was reached. Here, good agreement is found generally and minor deviations appear as both simulations are partly based on different models, e.g. different dependencies for membrane ionic conductivity on membrane water content and the treatment of reactant crossover in the 3D CFD simulations. The obtained fitting parameters are summarised in Table 4.

4.1. Steady-state validation

To evaluate the predictive capabilities of the LIT model, polarisation curves with outlet pressures $\tilde{p}_{out}$ = 1.3/1.5 bar and 3.3/3.5 bar are compared to AVL Fire™ M calculations, keeping the values of all fitting parameters unchanged. As shown in Fig. 4, the polarization curves of the LIT model align both quali- and quantitatively with the 3D simulations for varying cathode/anode pressures of 1.3/1.5, 2.3/2.5, and 3.3/3.5 bar under the relevant operating conditions of the PEMFC above 2000 A m^{-2}. A detailed error analysis between LIT and CFD calculations is shown in Appendix A.1. Here, the observed deviations are within the expected prediction accuracy. For most of the operating points the deviation remains within ±25 %, which we estimate to be roughly of the order of the error introduced by cross-sectional averaging and the simplified physical–mathematical description of the LIT model. At low current densities, the absence of reactant crossover in the LIT model leads to larger deviations from the CFD results, where crossover effects are explicitly accounted for. At high current densities — particularly at elevated operating pressures — the observed deviations arise from neglected reactant concentration losses in the catalyst layer. Nevertheless, despite these limitations, the LIT model remains capable of capturing the overall cell behaviour in the practically relevant operating regime.

To analyse the gas species mole fraction distribution in the gas channels along the x_1-direction, results for selected steady-state operating points, denoted as A, B and C in Fig. 4, are presented in Fig. 5. Each column represents one of the selected operating points. These three operating points are evaluated for equal cell potential $\tilde{E}_{cell}$ = 0.6 V. For a better comparison of the quasi-2D and 3D results obtained by the LIT model and AVL Fire™, respectively, cross-sectional averaged values are computed for the latter. Specifically, the results for the gas channels are averaged with respect to the x_2- and x_3-directions, similar to Eq. (2). The offsets between the species distributions again arise from the various submodels used in the two approaches. However, the overall characteristics show good agreement for all outlet pressure operating conditions. Further, the spatial distributions of the liquid water saturation s_l in the cathode GDL is compared in Fig. 6(a). For case A, representing the operating point with the smallest current density $\tilde{i}_{cell}$ = 4797 A m^{-2}, the LIT model accurately predicts the locations of liquid water formation; however, it fails to quantify

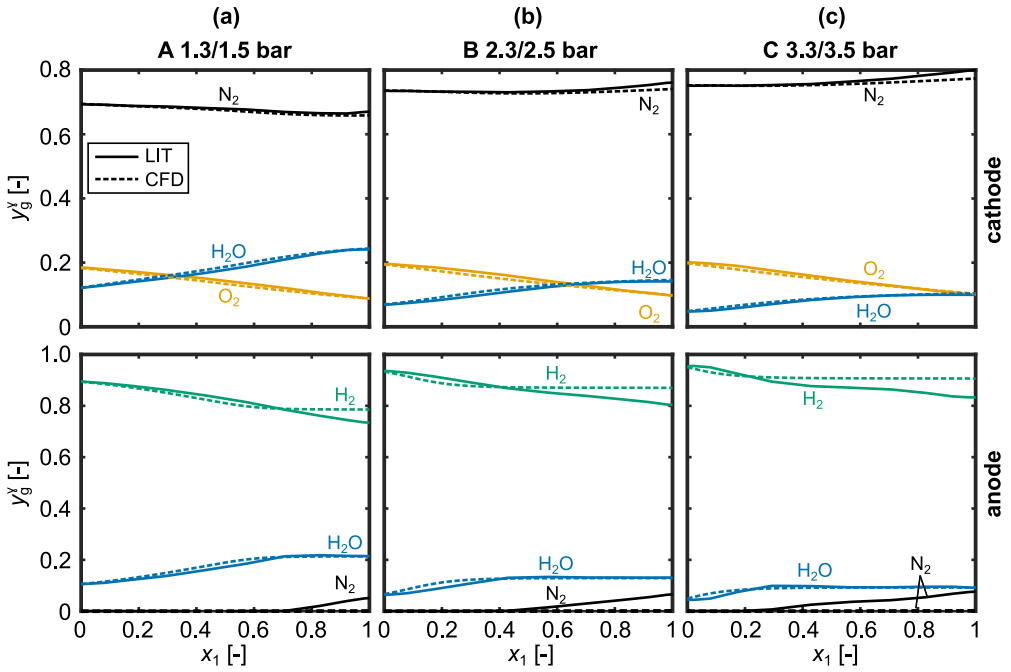

Fig. 5. Cathode and anode channel distributions of the gas mole fractions y_g^γ for the 3D CFD and the LIT model for a cell potential of $\tilde{E}_{cell}$ = 0.6 V and cathode/anode side outlet pressures $\tilde{p}_{out}$ (a) 1.3/1.5 bar, (b) 2.3/2.5 bar and (c) 3.3/3.5 bar. CFD results are cross-sectional averaged values, coloured lines represent different gas species: orange-O_2, blue-H_2O, black-N_2 and green-H_2. (For interpretation of the references to colour in this figure legend, the reader is referred to the web version of this article.)

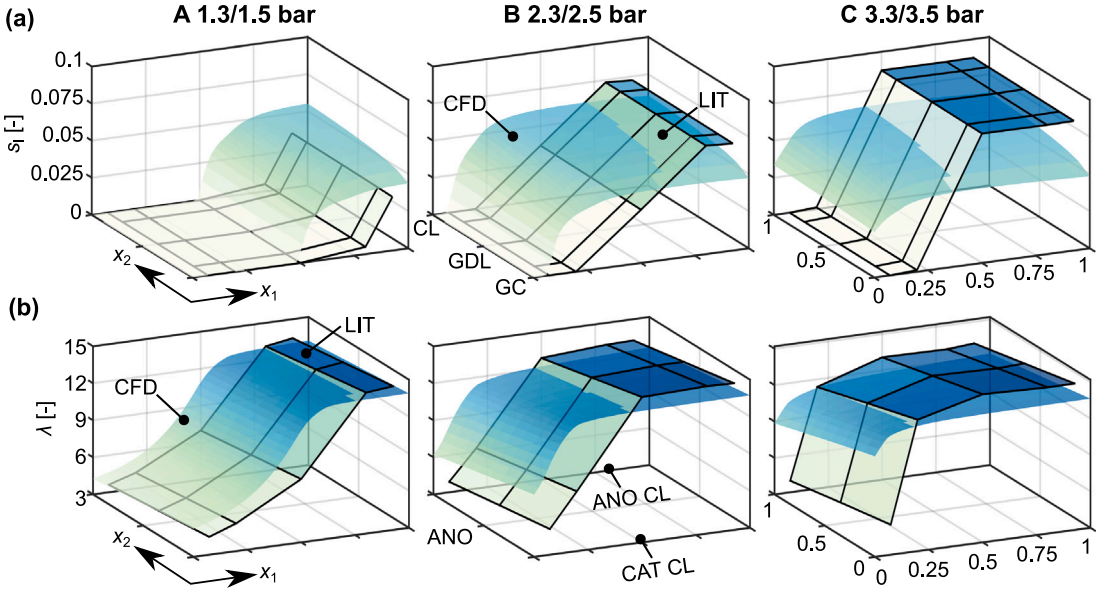

Fig. 6. Steady-state distributions of (a) liquid water saturation s_l in the cathode GDL and (b) normalised membrane water content λ obtained from the LIT model and CFD simulations for different cathode/anode side outlet pressures $\tilde{p}_{out}$ = 1.3/1.5 bar, 2.3/2.5 bar, 3.3/3.5 bar, and cell potential $\tilde{E}_{cell}$ = 0.6 V. CFD results are averaged along the x_3-direction.

liquid water accumulation in the porous GDL. For cases B and C, the LIT model provides a better prediction of the average liquid water formation. However, the trend along the x_1-direction appears almost linear, with a liquid-free region at the beginning and a plateau at the end. In contrast, the CFD simulations show a more uniform distribution along the channel, albeit with a similar depletion of liquid water at the inlet. In both the LIT model and the AVL Fire™ M simulations liquid water saturation s_l is of the order 10^{-3} in the anode GDL and below 10^{-4} in both channels. It should be stressed that, for most fuel cell control applications, the exact amount of water accumulation is not critical; an estimate of its magnitude and spatial distribution is typically sufficient to prevent flooding conditions. Therefore, the LIT model, with its reduced complexity and enhanced computational efficiency, serves as an ideal tool for practical control-oriented applications while still capturing the key physical trends.

A similar picture is found when the results of AVL Fire™ M and the LIT model are compared in terms of the normalised PEM water content λ, Fig. 6(b). The LIT model both qualitatively and quantitatively captures the trends of increased membrane hydration and spreading along the

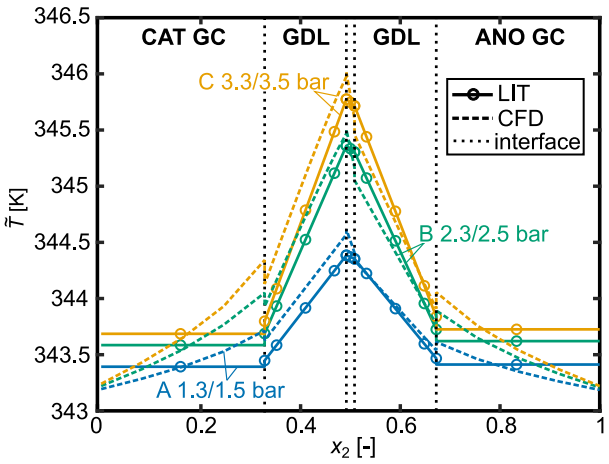

Fig. 7. Comparison of steady-state temperature profiles in the through plane direction x_2 at $x_1 = 0.5$ obtained from the LIT model and CFD simulations for different cathode/anode outlet pressures $\tilde{p}_{\text{out}} = 1.3/1.5\,\text{bar}$, $2.3/2.5\,\text{bar}$, $3.3/3.5\,\text{bar}$, and cell potential $\tilde{E}_{\text{cell}} = 0.6\,\text{V}$. Circles indicate the Gauss–Lobatto grid of the LIT model, the dotted lines show the GC/GDL and GDL/PEM interfaces. The constant temperature values in the gas channels are due to the underlying assumptions of the LIT model.

channel direction with increasing pressure (i.e. current density) due to the increased formation of reactant water in the cathode catalyst layer. Here, the small deviations likely stem from differences in the modelling of the membrane's sorption isotherm. Additionally, it is important to highlight the strong influence of the liquid water saturation s_l on λ, which significantly affects the results of the 3D CFD and LIT model simulations. The CFD variables s_l and λ are averaged here along the x_3-direction (membrane width) for better comparison. As the mass and heat transfer coefficients appearing in the coupling conditions between gas channel and GDL, Eqs. (12)–(14), are fitting parameters, we conducted a sensitivity analysis to assess their impact on flooding and cell performance predictions. Details and results of this analysis are presented in Appendix A.2.

Fig. 7 finally depicts the through-plane temperature distributions at the centre of the PEMFC ($x_1 = 0.5$), averaged along the x_2- and x_3-directions, for the operating points A, B, and C. These results, obtained from both CFD and LIT model simulations, reveal the influence of the operating pressure on the temperature profiles. At higher operating pressures the temperature level rises due to the increased generation of heat in the membrane and catalyst layers. The through-plane temperature profiles in the membrane electrode assembly predicted by the LIT model show both qualitative and quantitative agreement with the 3D CFD simulations across the different applied anode/cathode channels outlet pressures $\tilde{p}_{\text{out}}$ of $1.3/1.5\,\text{bar}$, $2.3/2.5\,\text{bar}$, and $3.3/3.5\,\text{bar}$. The maximum temperature deviations between the two model results remain within $\lesssim 0.2\,\text{K}$, a level of agreement that is particularly relevant for degradation predictions. Because of its quasi-2D formulation, the LIT model cannot capture the temperature gradients in the x_2- and x_3-directions present in the gas channels but instead provides a constant temperature. Nevertheless, the predicted values closely match the average temperature levels observed in the CFD simulations and thus the impact on phase change predictions in the channel is negligible; for details see Appendix A.3. The observed temperature discontinuity at the GC-GDL interface arises from the cross-sectional averaging applied to the CFD results.

4.2. Dynamic simulations

A comprehensive validation of transient processes is difficult, as experimental data is hardly available. Therefore, the LIT model results are analysed with respect to dynamic FC model results presented by other authors. In this regard, the FC's dynamic response to typical state changes as introduced by Goshtasbi and co-workers [19] are considered in the following. Fig. 8 shows the time evolution of the average current density $\tilde{i}_{\text{avg}}$, as well as the temperature $\tilde{T}$ and liquid water saturation s_l in the cathode catalyst layer at the gas channel outlet. The simulations start from a steady state at $\tilde{E}_{\text{cell}} = 0.8\,\text{V}$ under two different inlet relative humidities at both sides: (a) $\text{RH}_{\text{in}} = 20\,\%$ and (b) $\text{RH}_{\text{in}} = 80\,\%$. The cell potential $\tilde{E}_{\text{cell}}$ is then changed steplike at $\tilde{t} = 20\,\text{s}$, $120\,\text{s}$, $220\,\text{s}$, and $320\,\text{s}$ to $0.6\,\text{V}$, $0.5\,\text{V}$, $0.6\,\text{V}$, and $0.8\,\text{V}$, respectively. The response of $\tilde{i}_{\text{avg}}$ immediately after the first two step changes is shown in more detail in Fig. 8(c).

After the first step, the current density increases abruptly in response to the applied potential drop, followed by a slower transient towards a new steady state. The characteristic time scale of this transition depends on the cell's humidity: for $\text{RH}_{\text{in}} = 80\,\%$, the dynamic response is slightly slower than for $\text{RH}_{\text{in}} = 20\,\%$. Slower FC relaxation dynamics with increasing cell humidity were also found by [19].

After the second step, the transient behaviour changes significantly. In high humidity, the current density exhibits both an over- and undershoot, indicating complex hydration dynamics due to increased membrane water content from the preceding chemical reaction. The characteristic time constants observed in both steps are considerably larger than those predicted by the model for the isothermal single-phase case [23], in which the transient aligns with estimates based on

$$\tilde{\tau}_{\text{m}} \sim \frac{2\tilde{\mathscr{F}}}{\tilde{i}_{\text{avg}}} \frac{\tilde{\rho}_{\text{PEM}} \tilde{H}_{\text{PEM}} \Delta\lambda}{\text{E}\tilde{\text{W}}} \,, \tag{65}$$

as proposed by Wang and Wang [55]. This estimate relates the membrane hydration change $\Delta\lambda$ to the average current density $\tilde{i}_{\text{avg}}$. The observed discrepancy becomes even more apparent in the second step, where the estimation predicts faster dynamics due to nearly unchanged membrane hydration. The computed values of $\tilde{\tau}_{\text{m}}$, $\tilde{i}_{\text{avg}}$, and $\Delta\lambda$ for the first two step changes for both humidities are summarised in Table 5. Notably, for $\text{RH}_{\text{in}} = 80\,\%$, no steady state in current density is reached even $100\,\text{s}$ after the second step, indicating particularly sluggish dynamics that are comparable to the behaviour of liquid water. A similar response is observed after the third step change, where the slow removal of liquid water from the gas diffusion layer (GDL) significantly delays the system's relaxation for both inlet relative humidities. Since membrane hydration and

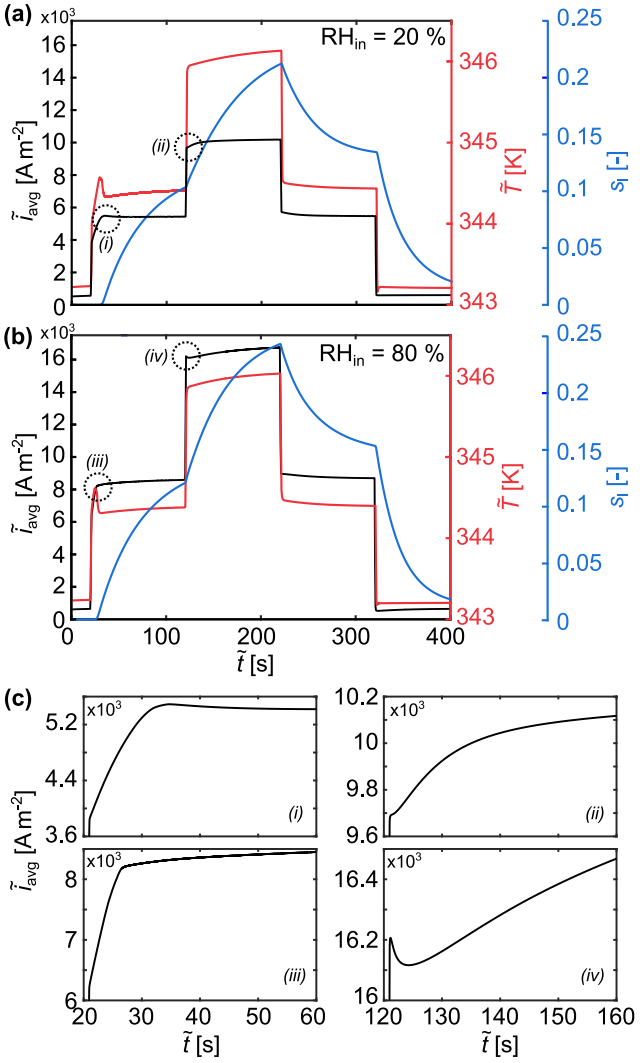

Fig. 8. Dynamic response of the average current density $\tilde{i}_{avg}$, temperature $\tilde{T}$, and liquid-water saturation sl in the cathode catalyst layer at the gas-channel outlet to a sequence of applied cell-potential steps. Results are shown for inlet relative humidities of (a) 20 % and (b) 80 %, with all other operating conditions identical to the reference steady state. Subfigure (c) provides zoomed-in views of the current-density response following the first two potential changes.. (For interpretation of the references to colour in this figure legend, the reader is referred to the web version of this article.)

Table 5
Parameters for the calculation of the characteristic timescales of membrane hydration. The change in membrane hydration $\Delta\lambda$ is calculated from the average water content in the beginning and end of the step change, denoted by $\bar{\lambda}_a$ and $\bar{\lambda}_b$, respectively. $\tilde{\tau}_m$ represents the characteristic timescale of membrane hydration calculated from Eq. (65).

	i	*ii*	*iii*	*iv*
$\tilde{i}_{avg}$ [A m^{-2}]	5300	8200	10 171	16 685
$\bar{\lambda}_a$ [−]	2.950	5.390	7.685	13.757
$\bar{\lambda}_b$ [−]	7.685	13.757	7.937	13.899
$\tilde{\tau}_m$ [s]	6.267	0.173	7.149	0.060

therefore the Ohmic losses depend on the liquid water content in the catalyst layer, Eq. (60), the time evolution of the current density is significantly influenced by liquid water generation. Consequently, the time constants are orders of magnitude larger compared to the estimates from Eq. (65).

The dynamic response of the current density can further be understood by analysing the characteristic timescale of liquid water transport $\tilde{\tau}_l$. The timescale is estimated using a simplified conservation model for a single slice of the cathode GDL, which balances liquid water accumulation with fluxes from the adjacent gas channel and the membrane, while neglecting spatial variations in the x_2-direction. Through dimensional analysis, the membrane sorption flux, Eq. (59), is identified as the dominant transport mechanism with characteristic time

$$\tilde{\tau}_l \sim \frac{\tilde{H}_{GDL}\,\mathrm{E\tilde{W}}\,\tilde{\rho}_l}{\tilde{\mathscr{M}}^{H_2O}\,\tilde{\rho}_{PEM}\,\tilde{\gamma}_{sorp}} \approx 122\,\mathrm{s}\,, \tag{66}$$

in good agreement with the observed evolution of s_l in the GDL and, correspondingly, $\tilde{i}_{avg}$, Fig. 8.

During the first step change the temperature in the catalyst layers shows an undershoot. This behaviour, also reported in [56], is primarily caused by latent heat release due to membrane water absorption. As the current density rises rapidly, excess water is generated and absorbed by the membrane, releasing heat [56,57]. At the same time, Ohmic losses increase, as electro-osmotic drag leads to membrane dehydration, raising resistance and contributing to additional Joule heating. The overshoot disappears in the second step, where the membrane is already well hydrated. Finally, in the last step even a temperature undershoot occurs due to the desorption of membrane water into the gas phase. Beyond this, the temperature evolution generally follows the behaviour of the current density closely, indicating a shorter characteristic time scale for heat transport, $\tilde{\tau}_\mathrm{h}$. Analogue to Eq. (66), one can estimate the characteristic timescale of heat transfer by applying the conservation of energy for a single GDL slice. Here, the convective heat transfer between the gas channel and the GDL, Eq. (14), is the relevant transport mechanism with the time constant

$$\tilde{\tau}_\mathrm{h} \sim \frac{\tilde{H}_\mathrm{GDL}\,\tilde{\rho}_\mathrm{GDL}\,\tilde{c}_\mathrm{GDL}}{\tilde{\alpha}_\mathrm{GDL}} \approx 0.8\,\mathrm{s}\,, \tag{67}$$

in line with the dynamic temperature response of the cell.

Despite the large current density differences between the two operating conditions, the resulting temperatures remain relatively similar at a given cell potential. After the second step e.g., the catalyst layers temperature is 346 K in both cases, despite the 6000 A m^{-2} larger current density for $\mathrm{RH_{in}} = 80\,\%$. This is due to a balance between current density and membrane conductivity: although Joule heating, $\tilde{S}_\mathrm{PEM} = \tilde{i}^2/\tilde{\sigma}$, increases with current density, it is mitigated by higher proton conductivity $\tilde{\sigma}$ from improved membrane hydration. As a result, the increased resistive heating is offset by enhanced charge transport, leading to similar temperature levels across different operating conditions.

The calculations of all the presented LIT model results were performed on an AMD Ryzen™ Threadripper PRO 3955WX 4.3 GHz CPU with 128 GB RAM. Although the solution procedure is not yet parallelised, the applied linearisation scheme of the governing equations, combined with the quasi-2D discretisation and spectral methods, enables the computation of a single time step in less than 100 ms. For comparison, on a conventional notebook system (AMD Ryzen™ 5 PRO 4650U 2.1 GHz, 16 GB RAM) computation of a single time step is still only 125 ms. The reported wall-clock computation time per simulation step corresponds to a sampling rate of approximately 10 Hz, which would in principle be sufficient for supervisory-level control tasks such as thermal and water management. However, the simulation of step-like load changes requires time step sizes between 1 ms to 5 ms for numerical stability, which increases the effective simulation time. To mitigate this, the implementation of variable time stepping significantly reduces the overall computational effort and enables the simulation of long-term transient behaviour. Specifically, the time step is reduced to accurately resolve rapid state variations during periods of large temporal gradients and increased to accelerate the simulation as the system approaches steady state. Table 6 provides an overview of how the discretisation of the LIT model affects the required computation time $\tilde{t}_\mathrm{c}$ for simulating the applied voltage profile shown in Fig. 8. In each row of Table 6, only one domain is discretised differently compared to the resolution used for validation (second row). By employing variable time stepping with step sizes in the range of 1 ms to 100 ms, the simulation time for the validation case is 1214 s, corresponding to an approximately 33-fold speed-up compared to a simulation with a fixed time step of 1 ms. As evident from Eq. (63), N_SL and N_GDL have the strongest influence on the dimension of the system of equations. Interestingly, however, the computation time is primarily affected by N_SL, despite similar system dimensions in rows three and five. This may be attributed to the stronger nonlinearity or stiffer dynamics associated with the membrane water phase, which may require more iterations during implicit time integration. Despite the drastically different system sizes between the lowest and highest resolutions, $\tilde{t}_\mathrm{c}$ does not even double, since the high sparsity (>0.96) is maintained for all discretisations. The first row in Table 6 corresponds to the smallest discretisation that ensures stable simulation, even during periods of strong temporal gradients. A grid convergence study shows a small but noticeable effect on both flooding and current density predictions when increasing the number of inner slices from 4 to 5. Further refinement of the discretisation leads only to marginal changes in these quantities.

The objective of the present model is to provide a computational environment suitable for control-oriented fuel-cell design studies and the development of degradation–mitigation strategies. Such applications rely on accurate representations of temperature dynamics, flooding behaviour, long transient trajectories, and sufficient spatial resolution to capture relevant gradients across the membrane, gas diffusion layers, and flow channels. In this context, the achieved execution speed of approximately one third of real time is sufficient, as these studies are typically conducted offline and focus on system-level dynamics evolving on long time scales. Building on the formulations in [23,25], the present model extends the physical scope through three key additions: (i) a non-isothermal treatment, capturing local temperature evolution and its feedback on reaction and transport kinetics; (ii) liquid-water formation and two-phase transport, enabling the prediction of flooding; and (iii) a non-equilibrium PEM–GDL mass-transfer description for more realistic transient behaviour. Despite this increased physical fidelity, the formulation remains well suited for substantial computational acceleration. The natural decomposition into spatial subdomains (anode, cathode, GDL, and channels) enables parallelisation across computing cores, while the governing equations exhibit pronounced sparsity that can be efficiently exploited by specialised solvers. Together, these properties provide a clear pathway for further optimisation beyond the performance of the current prototype.

At the same time, the present approach entails several inherent trade-offs. The quasi-2D representation simplifies GDL and channel interactions and does not resolve catalyst-layer microstructure or localised porous-electrode heterogeneities. Gas crossover beyond N_2 is neglected, and liquid-water predictions are limited by the absence of explicit droplet detachment, coalescence, and channel-clogging dynamics. These limitations reflect a deliberate trade-off between physical fidelity and computational efficiency, chosen to support design studies and long transient simulations relevant to operational and control-oriented analyses.

5. Conclusion and outlook

In this work, a computationally highly efficient PEMFC model for non-isothermal and multiphase flow dynamic simulations with quasi-2D spatial resolution is proposed as an extension of the model for isothermal single-phase conditions developed by Murschenhofer et al. [23]. The current model captures key physical phenomena, including liquid water formation, two-phase transport by convection, multicomponent diffusion and capillary fluxes in the gas channels and GDLs. Unlike the previous approach, the present model dismisses the equilibrium condition for the membrane water content at the GDL–PEM interface and instead accounts for finite-rate mass transfer during membrane sorption and desorption processes. Additionally, the model incorporates heat generation from electrochemical reactions, finite proton conductivity, and phase changes. The models for the electrochemistry, the membrane water transport by electro-osmotic drag and diffusion, as well as N_2 crossover, remain unchanged. The adopted quasi-2D multiphase mixture approach [38] reduces the required number of governing equations while still capturing the essential mass and heat transport phenomena. A numerical scheme based on Chebyshev collocation for spatial discretisation, combined with the linearisation

Table 6
Required computation time $\tilde{t}_c$ for various spatial discretisations in the dynamic simulations of consecutive cell potential steps shown in Fig. 8 with a simulation time of 400 s (AMD Ryzen™ Threadripper PRO 3955WX 4.3 GHz CPU with 128 GB RAM). N_{GC}, N_{GDL}, N_{PEM} and N_{SL} denote the number of nodes for the gas channel, the GDL, the membrane and the number of 'inner slices', respectively. The size and sparsity of the square system matrices $\mathbf{A}$, Eq. (62), and $\mathbf{A}_l$ are indicated as N_A/N_{A_l} and S_A/S_{A_l}, respectively.

N_{GC}	N_{GDL}	N_{PEM}	N_{SL}	N_A/N_{A_l}	S_A/S_{A_l}	$\tilde{t}_c$ [s]
12	5	3	4	552/64	0.961/0.765	983
12	5	3	5	642/74	0.967/0.793	1214
12	5	3	7	822/94	0.974/0.832	1618
12	5	5	5	662/74	0.968/0.793	1769
12	7	3	5	802/94	0.971/0.822	1246
14	5	3	5	674/78	0.964/0.777	1281

of the governing equations in time (LIT), ensures comparatively low computational effort. Utilisation of a particle swarm optimisation algorithm further allows for the efficient fitting of the model's polarisation curve prediction to desired reference data, e.g. obtained from experimental setups or high-resolution 3D simulations.

A detailed validation of the model is conducted against steady-state CFD simulations of a 3D fuel cell geometry performed with the commercially available AVL Fire™ software package [49]. The results of the LIT model, in terms of predicted polarisation curves and the distributions of gaseous species, temperature, liquid water, and PEM water content, show fairly good agreement with the CFD simulations under various operating conditions. Furthermore, the transient behaviour of the temperature and the liquid water accumulation in the porous electrodes aligns with data from the existing literature. The model's capabilities offer a valuable tool for fuel cell control engineering, facilitating efficient control unit optimisation and state-observer predictions. In particular, the current model enables model-based control strategies that can dynamically account for heat and water management during varying load conditions. Its computational efficiency makes the present model particularly suitable for widespread parameter studies and performance analyses.

Future work will focus on increasing both fidelity and computational performance. Physically, improved catalyst-layer descriptions and explicit representation of droplet dynamics in the gas channels could further refine predictive accuracy. Computationally, leveraging spatial-domain parallelisation and sparse-solver strategies offers significant potential for acceleration, ultimately paving the way towards real-time model-based control, optimisation, and degradation–mitigation strategies.

CRediT authorship contribution statement

Florian Altmann: Writing – original draft, Visualization, Validation, Software, Methodology, Conceptualization. **Dominik Kuzdas:** Writing – review & editing, Methodology, Conceptualization. **Dominik Murschenhofer:** Writing – review & editing, Methodology, Conceptualization. **Johanna Bartlechner:** Writing – original draft, Visualization, Investigation. **Christoph Hametner:** Supervision, Funding acquisition. **Stefan Jakubek:** Supervision, Funding acquisition. **Stefan Braun:** Writing – review & editing, Supervision, Conceptualization.

Declaration of Generative AI and AI-assisted technologies in the writing process

During the preparation of this work, the author(s) used ChatGPT to review grammar and spelling in the manuscript. After using this tool, the author(s) reviewed and edited the content as needed and take full responsibility for the content of the publication.

Declaration of competing interest

The authors declare that they have no known competing financial interests or personal relationships that could have appeared to influence the work reported in this paper.

Acknowledgements

The authors acknowledge TU Wien Bibliothek, Austria for financial support through its Open Access Funding program. This work was funded by the Austrian Research Promotion Agency (FFG), Austria in the scope of the project *AlpeDHues* (grant number 884322). The authors would like to thank AVL List GmbH for providing the software used within the framework of their University Partnership Program. The financial support by the Austrian Federal Ministry of Labour and Economy, the National Foundation for Research, Technology and Development and the Christian Doppler Research Association is gratefully acknowledged.

Appendix A. Supplementary data

A.1. Polarisation curve error analysis

Fig. A.9 illustrates the relative error of the LIT model's predicted current density with respect to the CFD reference along the polarisation curve for several operating pressures shown in Fig. 4. Across the ohmic region of the polarisation curve, the LIT model reproduces the CFD results with deviations below approximately 25 %, indicating good agreement in the regime where the fuel cell typically operates. At low current densities, larger discrepancies occur due to reactant crossover and associated parasitic effects, which are not explicitly resolved in the reduced quasi-2D formulation. This behaviour is consistent with the intended scope of the LIT model, which is designed to capture the dominant transport and electrochemical mechanisms in the practically relevant operating range rather than to resolve crossover-dominated regimes.

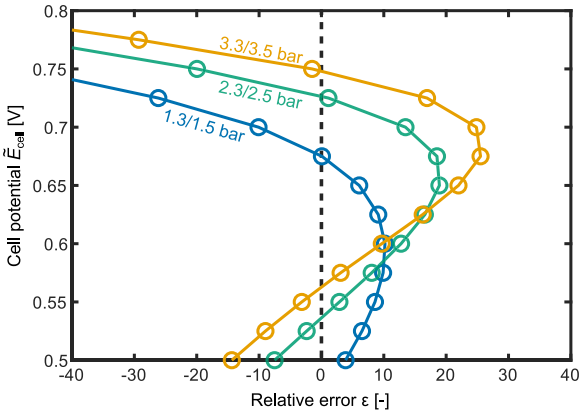

Fig. A.9. Evolution of the relative error $\epsilon = (\tilde{i}_{CFD} - \tilde{i}_{LIT})/\tilde{i}_{CFD}$ within the FC's operational range from the polarisation curves in Fig. 4.

A.2. Fitting parameter sensitivity analysis

This appendix presents a dedicated sensitivity analysis of the three fitted transfer coefficients in Eqs. (12), (13) and (14) to describe mass and heat transfer at the GC-GDL interface: (a) the liquid-phase mass-transfer coefficient $\tilde{\beta}_l$, (b) the fitting factor for the gas-phase transport coefficient f_β, and (c) the interfacial heat-transfer coefficient $\tilde{\alpha}_{GDL}$. Each parameter was varied over several orders of magnitude to assess its influence on the local liquid water saturation s_l at the GC-GDL interface and cell current density $\tilde{i}_{avg}$. The results for the parametric sweeps with operating conditions B of Fig. 4 are summarised in Fig. A.10.

Reducing β_l (Fig. A.10(a)) by one order of magnitude results in a substantial increase in the liquid water saturation within the GDL, approximately doubling the saturation compared to the baseline case. When the coefficient is decreased further, the saturation approaches a plateau, indicating a fully transport-limited regime in which additional reductions in the mass-transfer rate no longer alter the liquid distribution. In contrast, increasing the coefficient by two orders of magnitude leads to efficient removal of liquid water, causing the saturation to approach zero. This parameter also influences the electrochemical performance: lower coefficients enhance membrane humidification and therefore increase the current density, whereas higher coefficients reduce humidification and correspondingly decrease the current density. Importantly, the reference value used in the main study lies near the centre of the sensitivity range and yields intermediate behaviour between these extremes, indicating that it represents a physically reasonable and balanced choice for capturing FC behaviour under the investigated conditions. The gas-phase transport coefficient f_β (Fig. A.10(b)) primarily controls the supply of reactant gases to the GDL and the removal of water vapour. Reducing this coefficient significantly restricts gas transport, resulting in reactant starvation and a collapse of the current density. As the coefficient is increased, both the current density and the gas-phase saturation initially rise due to improved reactant access. At higher values, these quantities decrease slightly and then reach a plateau, reflecting a transition from a transport-limited to a reaction-limited regime. Moreover, stronger removal of water vapour at high coefficients further reduces the liquid-water saturation in the GDL. The reference value used in the main simulations lies within the intermediate region between starvation and the high-transport plateau, and therefore represents a physically meaningful and balanced choice that avoids unrealistic reactant limitation while not implying excessively strong vapour removal. Variations in the interfacial heat-transfer coefficient $\tilde{\alpha}_{GDL}$ (Fig. A.10(c)) have only a negligible impact on the model predictions. Across the tested range, neither the current density, nor the liquid-water distribution show any significant sensitivity to this parameter. This indicates that interfacial heat-transfer limitations do not play a relevant role under the operating conditions considered in this study.

A.3. Quantitative assessment of gas channel temperature effects

Table A.7 compares the LIT model's cross-sectional average gas channel temperature and liquid water saturation in the centre of the cell for the operating points shown in Fig. 7. The corresponding CFD data are reported as minimum, maximum, and average values across each cross-section, capturing the spatial variability visible in the CFD fields shown in Fig. 7. This comparison allows us to assess how the neglected gas-channel temperature gradients influence the liquid-water predictions of the LIT model.

In the CFD reference, the temperature drop along the channel ranges from about 0.5 to 1.1 K across the examined operating points. Despite the model simplifications, the LIT model matches the cross-sectional CFD averages closely: deviations remain below 0.05 K, corresponding to relative differences below 0.02 %. Since the saturation pressure at typical PEMFC conditions changes by roughly 3 to 5 % per Kelvin, such small temperature differences have a negligible impact on phase-change behaviour in the channel. While the LIT model predicts uniformly low saturations $< 1 \times 10^{-5}$, the CFD results show minor liquid formation only at the channel–GDL interface node and otherwise yield similar values. This discrepancy is expected, as the quasi-2D LIT model captures only cross-sectional averages, whereas the CFD resolves localised liquid pockets and micro-scale phase distributions. Crucially, both approaches indicate very low overall liquid-water content in the channel under the examined conditions. Thus, the saturation differences are primarily due to spatial-resolution effects rather than the minor temperature differences, and they have little influence on the interpretation of two-phase transport in this region.

Appendix B. Dimensionless groups

To obtain the governing equations in non-dimensional form, each variable is consequently replaced by a dimensionless variable multiplied by a characteristic reference value, e.g. for an arbitrary variable $\tilde{x}$

$$\tilde{x} = \tilde{x}_r x\,, \tag{B.1}$$

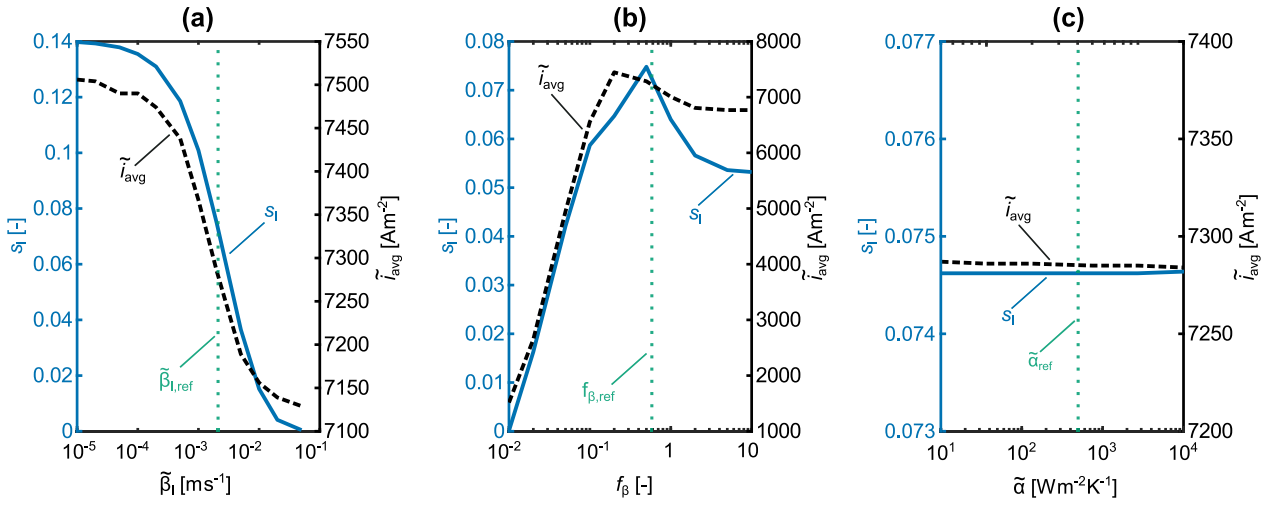

Fig. A.10. Sensitivity analysis of (cathode) GC-GDL mass and heat transfer coefficients. Response of the liquid water saturation s_l (blue full line) and current density $\tilde{i}_{avg}$ (black dashed line) to parameter variations of (a) the liquid-phase mass transfer coefficient $\tilde{\beta}_l$, (b) the gas-phase transport fitting factor f_β, and (c) the interfacial heat transfer coefficient $\tilde{\alpha}_{GDL}$. The vertical dotted line corresponds to the reference value used in the main studies. (For interpretation of the references to colour in this figure legend, the reader is referred to the web version of this article.)

Table A.7
Comparison of channel temperature and liquid-water saturation predicted by the LIT model and CFD cross-sectional averages at the operating condition shown in Fig. 7.

$\tilde{p}_{out}$ CAT/ANO [bar]	$\bar{T}_{LIT}$ [K]	$\bar{T}_{CFD}$ [K]	$s_{l,LIT}$ [−]	$s_{l,CFD}$ [−]
1.3/1.5	343.38	343.42	7.43×10^{-7}	1.00×10^{-6}
2.3/2.5	343.57	343.59	5.31×10^{-6}	1.55×10^{-4}
3.3/3.5	343.70	343.72	8.70×10^{-6}	3.79×10^{-4}

Table B.8
Characteristic reference values used to obtain the dimensionless formulation of the governing equations. Since all entries are dimensional values, tilde is omitted for simplicity.

$(\cdot)_r$	GC, $a = 1$		GDL, $a = 2$		PEM
	CAT	ANO	CAT	ANO	
E_{cell}	–	–	–	–	E_{OC}
i	–	–	–	–	i_r
p	p_{amb}	p_{amb}	p_{amb}	p_{amb}	–
T	T_r	T_r	T_r	T_r	T_r
t	$\frac{L}{u_{1,in}}$	$\frac{L}{u_{1,in}}$	$\frac{H_{GDL}^2}{\mathscr{D}_{O_2,H_2O}}$	$\frac{H_{GDL}^2}{\mathscr{D}_{H_2,H_2O}}$	$\frac{H_{PEM}^2}{D_w}$
u	$u_{1,in}$	$u_{1,in}$	$\frac{\mathscr{D}_{O_2,H_2O}}{H_{GDL}}$	$\frac{\mathscr{D}_{H_2,H_2O}}{H_{GDL}}$	–
x_a	L	L	H_{GDL}	H_{GDL}	H_{PEM}
$\dot{m}_l$	$\frac{\rho_{air} u_r}{L}$	$\frac{\rho_{H_2} u_r}{L}$	$\frac{\rho_{air} u_r}{H_{GDL}}$	$\frac{\rho_{H_2} u_r}{H_{GDL}}$	–
$\mathscr{D}$	$\mathscr{D}_{O_2,H_2O}$	$\mathscr{D}_{H_2,H_2O}$	$\mathscr{D}_{O_2,H_2O}$	$\mathscr{D}_{H_2,H_2O}$	D_w
$\mathscr{M}$	$\mathscr{M}^{O_2}$	$\mathscr{M}^{H_2}$	$\mathscr{M}^{O_2}$	$\mathscr{M}^{H_2}$	–
μ	μ_g^{air}	$\mu_g^{H_2}$	μ_g^{air}	$\mu_g^{H_2}$	–
ρ	ρ_{air}	$\rho_g^{H_2}$	ρ_{air}	$\rho_g^{H_2}$	ρ_{PEM}
c	c_g^{air}	$c_g^{H_2}$	c_g^{air}	$c_g^{H_2}$	c_{PEM}
k	k_g^{air}	$k_g^{H_2}$	k_{GDL}	k_{GDL}	k_r
σ	–	–	–	–	σ_r

where $\tilde{x}$, $\tilde{x}_r$ and x denote the dimensional, characteristic reference and dimensionless variables, respectively. The characteristic reference variables for each domain are listed in Table B.8.

Commonly used dimensionless groups such as the Reynolds number Re, Schmidt number Sc and Péclet number Pe, as well as the density ratio between the gas and liquid phases are defined in Table B.9. The dimensionless groups that appear in the governing equations for the PEM, Section 2.4, the gas channels, Section 2.2, and GDL domains, Section 2.3, are listed in Tables B.10–B.12, respectively. Due to the orientation of the coordinate system, the dimensionless groups for the gas channel–GDL coupling fluxes in the gas channel conservation equations have a negative sign on the anode side. The numerical values of the dimensional groups are computed with the reference values from the validation, see Tables 4 and B.13. Note that the terms in the gas channel's governing equations accounting for the coupling of diffusive mass and enthalpy fluxes with the

Table B.9
Reynolds number (Re), Schmidt number (Sc), and the two Péclet numbers (Pe_{GC} and Pe_{GDL}) characterising mass transport in the gas channel. Pe_{GC} relates convective to diffusive transport within the gas channel, while Pe_{GDL} compares convective transport in the channel to mass transport through the gas diffusion layer (GDL). The dimensionless groups for the density ratio K_ρ and equation of state K_{EOS} are used in both the gas channel and GDL domains.

Dimensionless group	Value CAT	Value ANO
$\mathrm{Re} = \frac{\tilde{u}_\mathrm{r}\,\tilde{D}_\mathrm{H}\,\tilde{\rho}_\mathrm{r}}{\tilde{\mu}_\mathrm{r}}$	103	23.2
$\mathrm{Sc} = \frac{\tilde{\mu}_\mathrm{r}}{\tilde{\mathscr{D}}_\mathrm{r}\,\tilde{\rho}_\mathrm{r}}$	0.616	0.818
$\mathrm{Pe}_\mathrm{GC} = \frac{\tilde{u}_{1,\mathrm{r}}\,\tilde{L}}{\tilde{\mathscr{D}}_\mathrm{r}}$	47.4	14.2
$\mathrm{Pe}_\mathrm{GDL} = \frac{\tilde{u}_{1,\mathrm{r}}\,\tilde{H}_\mathrm{GDL}}{\tilde{\mathscr{D}}_\mathrm{r}}$	23.7	7.12
$K_\rho = \frac{\tilde{\rho}_\mathrm{r}}{\tilde{\rho}_\mathrm{l}}$	1.01×10^{-3}	1.09×10^{-4}
$K_\mathrm{EOS} = \frac{\tilde{\mathscr{R}}\,\tilde{T}_\mathrm{r}\,\tilde{\rho}_\mathrm{r}}{\tilde{p}_\mathrm{r}\,\tilde{\mathscr{M}}_\mathrm{r}}$	0.845	1.45

Table B.10
Dimensionless groups for the membrane domain.

Dimensionless group	Value
$K_{D1} = \frac{\mathrm{E\tilde{W}}\,\tilde{\imath}_\mathrm{r}\,C_\mathrm{drag}\,\tilde{\imath}_\mathrm{r}}{\tilde{\rho}_\mathrm{PEM}\,\tilde{\mathscr{F}}\,\tilde{H}_\mathrm{PEM}}$	2.91
$K_{E1} = \frac{\mathrm{E\tilde{W}}\,\tilde{c}_\mathrm{PEM}}{\tilde{\mathscr{M}}^{\mathrm{H_2O}}\,\tilde{c}_\mathrm{l}}$	15.9
$K_{E2} = K_{D1}$	2.91
$K_{E3} = \frac{\mathrm{E\tilde{W}}\,\tilde{\imath}_\mathrm{r}\,\tilde{k}_\mathrm{r}}{\tilde{\mathscr{M}}^{\mathrm{H_2O}}\,\tilde{\rho}_\mathrm{PEM}\,\tilde{c}_\mathrm{l}\,\tilde{H}^2_\mathrm{PEM}}$	1.17×10^5
$K_{E4} = \frac{\mathrm{E\tilde{W}}\,\tilde{\imath}_\mathrm{r}\,i^2_\mathrm{r}}{\tilde{\mathscr{M}}^{\mathrm{H_2O}}\,\tilde{\rho}_\mathrm{PEM}\,\tilde{c}_\mathrm{l}\,\tilde{T}_\mathrm{r}\,\tilde{\sigma}_\mathrm{r}}$	147

GDL — associated with the dimensionless groups K_{L1}, K_{S1} and K_{E2-E4} in Table B.11 - are retained in the model to ensure validity even in the limit $\tilde{u}_{m,1} \to 0$, as encountered e.g. in dead-end operation. To calculate the Reynolds number Re, Table B.9, the hydraulic diameter $\tilde{D}_\mathrm{H}$ for a rectangular duct is defined as, [58],

$$\tilde{D}_\mathrm{H} = \frac{2\tilde{H}_\mathrm{GC}\tilde{W}_\mathrm{GC}}{\tilde{H}_\mathrm{GC} + \tilde{W}_\mathrm{GC}}\,. \tag{B.2}$$

Appendix C. Multiphase mixture framework

The derivation of the governing equations for the present PEMFC model is based on a multiphase mixture approach that treats the gas and liquid phases as constituents of a multiphase mixture, neglecting detailed phase interactions [26]. Thereby the necessity to solve individual conservation laws for the momentum and energy of each phase is omitted, drastically reducing the computational effort. The principal equations for the derivation of the governing equation of the LIT PEMFC model are summarised below. In general, an individual phase k consists of multiple species γ. For each species γ the continuity equation

$$\int_{\tilde{V}} \frac{\partial(s_k\tilde{\rho}_k\xi_k^\gamma)}{\partial\tilde{t}}\,\mathrm{d}\tilde{V} + \oint_{\partial\tilde{V}} s_k\tilde{\rho}_k\tilde{\mathbf{u}}_k\xi_k^\gamma\,\mathrm{d}\tilde{S} + \oint_{\partial\tilde{V}} \tilde{\mathbf{j}}_k^\gamma\,\mathrm{d}\tilde{S} = \int_{\tilde{V}} \tilde{m}_k^\gamma\,\mathrm{d}\tilde{V} \tag{C.1}$$

applies, here $\tilde{\rho}_k$ is the mass density of phase k with volume fraction s_k, and ξ_k^γ is the mass fraction of species γ in phase k. The phase velocity is further denoted by $\tilde{\mathbf{u}}_k$ and $\tilde{\mathbf{j}}_k^\gamma$ denotes a diffusive mass flux within the phase. The right hand side term represents a volumetric source term for species γ in phase k.

In the two-phase fluid of the PEMFC gas channels and the GDLs, the gaseous phase consists of three species $\gamma = \alpha$, N_2 and H_2O. Here, α represents the reactant species of the electrochemical reaction at the anode, $\alpha = H_2$, and cathode side, $\alpha = O_2$, respectively. Summation of Eq. (C.1) over all species and applying the closure conditions for the phase volume fractions, the mass fractions and the diffusive fluxes,

$$s_\mathrm{l} + s_\mathrm{g} = 1\,, \quad \sum_\gamma \xi_\mathrm{g}^\gamma = 1\,, \quad \sum_\gamma \mathbf{j}_\mathrm{g}^\gamma = \mathbf{0}\,, \tag{C.2}$$

as well as considering that H_2O undergoes phase change only and that no other sources appear in the gas channels and GDLs,

$$\tilde{m}_\mathrm{l}^{\mathrm{H_2O}} = -\,\tilde{m}_\mathrm{g}^{\mathrm{H_2O}} \equiv \tilde{m}_\mathrm{l}\,, \tag{C.3}$$

yields the mass balance of the gas phase (GMB),

$$\int_{\tilde{V}} \frac{\partial((1-s_\mathrm{l})\tilde{\rho}_\mathrm{g})}{\partial\tilde{t}}\,\mathrm{d}\tilde{V} + \oint_{\partial\tilde{V}} (1-s_\mathrm{l})\tilde{\rho}_\mathrm{g}\tilde{\mathbf{u}}_\mathrm{g}\,\mathrm{d}\tilde{S} = -\int_{\tilde{V}} \tilde{m}_\mathrm{l}\,\mathrm{d}\tilde{V}\,. \tag{C.4}$$

Table B.11
Dimensionless groups for the gas channel domains.

Dimensionless group	Value CAT	Value ANO
$K_{\mathrm{T1}}^{\mathrm{C}} = \frac{\tilde{W}_{\mathrm{GDL}}}{\tilde{W}_{\mathrm{GC}}} \frac{\tilde{L}}{\tilde{H}_{\mathrm{GC}}} \frac{1}{\mathrm{Pe}_{\mathrm{GDL}}} = -K_{\mathrm{T1}}^{\mathrm{A}}$	10.6	−35.1
$K_{\mathrm{L1}}^{\mathrm{C}} = \frac{\tilde{W}_{\mathrm{GDL}}}{\tilde{W}_{\mathrm{GC}}} \frac{\tilde{L}}{\tilde{H}_{\mathrm{GC}}} \frac{K_{\rho}}{\mathrm{Pe}_{\mathrm{GDL}}} = -K_{\mathrm{L1}}^{\mathrm{A}}$	0.0107	-3.84×10^{-3}
$K_{\mathrm{L2}}^{\mathrm{C}} = \frac{\tilde{W}_{\mathrm{GDL}}}{\tilde{W}_{\mathrm{GC}}} \frac{\tilde{L}}{\tilde{H}_{\mathrm{GDL}}} \frac{\sqrt{\varepsilon\tilde{\kappa}} \cos(\theta_{\mathrm{c}}) \tilde{\zeta}_{\mathrm{l}}}{\tilde{\rho}_{\mathrm{l}} \tilde{u}_{1,\mathrm{r}} \tilde{\nu}_{\mathrm{r}}} = -K_{\mathrm{L2}}^{\mathrm{A}}$	−1.56	0.353
$K_{\mathrm{S1}}^{\mathrm{C,A}} = \frac{1}{\mathrm{Pe}_{\mathrm{GC}}}$	1.69×10^{-4}	5.62×10^{-4}
$K_{\mathrm{S2}}^{i} = K_{\mathrm{T1}}^{i}$	10.6	35.1
$K_{\mathrm{E1}}^{\mathrm{C,A}} = \frac{(\tilde{c}_{\mathrm{l}} - \tilde{c}_{\mathrm{g}}^{\mathrm{H_2O}})}{\tilde{c}_{\mathrm{r}}}$	2.16	0.151
$K_{\mathrm{E2}}^{\mathrm{C,A}} = \frac{(\tilde{c}_{\mathrm{g}}^{\beta} - \tilde{c}_{\mathrm{g}}^{\mathrm{N_2}})}{\tilde{c}_{\mathrm{r}}} \frac{1}{\mathrm{Pe}_{\mathrm{GC}}}$	-1.92×10^{-5}	5.21×10^{-4}
$K_{\mathrm{E3}}^{\mathrm{C,A}} = \frac{(\tilde{c}_{\mathrm{g}}^{\mathrm{H_2O}} - \tilde{c}_{\mathrm{g}}^{\mathrm{N_2}})}{\tilde{c}_{\mathrm{r}}} \frac{1}{\mathrm{Pe}_{\mathrm{GC}}}$	1.60×10^{-4}	3.72×10^{-5}
$K_{\mathrm{E4}}^{\mathrm{C,A}} = \frac{(\tilde{c}_{\mathrm{l}} - \tilde{c}_{\mathrm{g}}^{\mathrm{H_2O}})}{\tilde{c}_{\mathrm{r}}} \frac{1}{\mathrm{Pe}_{\mathrm{GC}}}$	3.66×10^{-4}	8.51×10^{-5}
$K_{\mathrm{E5}}^{\mathrm{C,A}} = \frac{2\tilde{L}}{\tilde{W}_{\mathrm{GC}}} \frac{\tilde{\alpha}}{\tilde{\rho}_{\mathrm{r}} \tilde{c}_{\mathrm{r}} \tilde{u}_{1,\mathrm{r}}}$	15.7	10.1
$K_{\mathrm{E6}}^{\mathrm{C,A}} = \frac{\tilde{L}}{\tilde{H}_{\mathrm{GC}}} \frac{\tilde{\alpha}}{\tilde{\rho}_{\mathrm{r}} \tilde{c}_{\mathrm{r}} \tilde{u}_{1,\mathrm{r}}}$	15.7	10.1
$K_{\mathrm{E7}}^{\mathrm{C,A}} = \frac{\tilde{L}}{\tilde{H}_{\mathrm{GC}}} \frac{\tilde{\alpha}_{\mathrm{GDL}}}{\tilde{\rho}_{\mathrm{r}} \tilde{c}_{\mathrm{r}} \tilde{u}_{1,\mathrm{r}}}$	15.7	10.1
$K_{\mathrm{M1}} = \frac{\tilde{p}_{\mathrm{r}}}{\tilde{\rho}_{\mathrm{r}} \tilde{u}_{1,\mathrm{r}}^2}$	6410	5.93×10^{4}
$K_{\mathrm{M2}} = \tilde{F}_{\mathrm{c}} \frac{\tilde{L}}{\tilde{D}_{\mathrm{H}}} \frac{8}{\mathrm{Re}}$	19.5	86.1

Table B.12
Nondimensional groups for the gas diffusion layer domains.

Nondimensional group	Value CAT	Value ANO
$K_{\mathrm{L1}}^{\mathrm{C,A}} = \frac{\sqrt{\varepsilon\tilde{\kappa}} \cos(\theta_{\mathrm{c}}) \tilde{\zeta}_{\mathrm{l}}}{\tilde{\rho}_{\mathrm{l}} \tilde{\mathscr{D}}_{\mathrm{r}} \tilde{\nu}_{\mathrm{r}}}$	−0.148	−0.0100
$K_{\mathrm{S1}}^{\mathrm{C,A}} = \frac{\sqrt{\varepsilon\tilde{\kappa}} \cos(\theta_{\mathrm{c}}) \tilde{\zeta}_{\mathrm{l}}}{\tilde{\rho}_{\mathrm{r}} \tilde{\mathscr{D}}_{\mathrm{r}} \tilde{\nu}_{r}}$	−146	−92.0
$K_{\mathrm{E1}}^{\mathrm{C,A}} = \frac{\tilde{\rho}_{\mathrm{GDL}} \tilde{c}_{\mathrm{GDL}}}{\tilde{\rho}_{\mathrm{r}} \tilde{c}_{\mathrm{r}}}$	2000	1300
$K_{\mathrm{E2}}^{\mathrm{C,A}} = \frac{(\tilde{c}_{\mathrm{l}} - \tilde{c}_{\mathrm{g}}^{\mathrm{H_2O}})}{\tilde{c}_{\mathrm{r}}}$	2.16	0.151
$K_{\mathrm{E3}}^{\mathrm{C,A}} = \frac{(\tilde{c}_{\mathrm{g}}^{\beta} - \tilde{c}_{\mathrm{g}}^{\mathrm{N_2}})}{\tilde{c}_{\mathrm{r}}}$	−0.113	0.928
$K_{\mathrm{E4}}^{\mathrm{C,A}} = \frac{(\tilde{c}_{\mathrm{g}}^{\mathrm{H_2O}} - \tilde{c}_{\mathrm{g}}^{\mathrm{N_2}})}{\tilde{c}_{\mathrm{r}}}$	0.945	0.0662
$K_{\mathrm{E5}}^{\mathrm{C,A}} = K_{\mathrm{S1}}^{\mathrm{C,A}}$	−146	−92.0
$K_{\mathrm{E6}}^{\mathrm{C,A}} = \frac{\tilde{c}_{\mathrm{l}}}{\tilde{c}_{\mathrm{r}}} K_{\mathrm{S1}}^{\mathrm{C,A}}$	−605	−26.7
$K_{\mathrm{E7}}^{\mathrm{C,A}} = \frac{(\tilde{c}_{\mathrm{l}} - \tilde{c}_{\mathrm{g}}^{\mathrm{H_2O}})}{\tilde{c}_{\mathrm{r}}} K_{\mathrm{S1}}^{\mathrm{C,A}}$	−316	−13.9
$K_{\mathrm{E8}}^{\mathrm{C,A}} = \frac{\tilde{k}_{\mathrm{r}}}{\tilde{c}_{\mathrm{r}} \tilde{\rho}_{\mathrm{r}} \tilde{u}_{2,\mathrm{r}}}$	9.54	2.58
$K_{\mathrm{M1}}^{\mathrm{C,A}} = \frac{\tilde{p}_{\mathrm{r}}}{\tilde{\rho} \tilde{u}_{2,\mathrm{r}}^2}$	3.59×10^{6}	3.01×10^{6}
$K_{\mathrm{M2}}^{\mathrm{C,A}} = \frac{\tilde{H}_{\mathrm{GDL}}^2}{\tilde{\kappa}} \varepsilon\,\mathrm{Sc}$	0.616	0.818
$K_{\mathrm{M3}}^{\mathrm{C,A}} = 2\,\mathrm{Sc}$	3280	4360

Table B.13
Reference values. Fluid properties for $\tilde{T} = 343.15\,\mathrm{K}$ and $\tilde{p} = 1\,\mathrm{bar}$.

Parameter [*unit*], reference	Symbol	Value
PEMFC temperature [K]	$\tilde{T}_\mathrm{r}$	343.15
Inlet velocity [m s^{-1}]	$\tilde{u}_{1,\mathrm{in}}$	0.1
Molar mass O_2 [kg mol^{-1}], [59]	$\mathscr{M}^{\mathrm{O_2}}$	31.9988×10^{-3}
Molar mass H_2 [kg mol^{-1}], [59]	$\mathscr{M}^{\mathrm{H_2}}$	2.016×10^{-3}
Dynamic viscosity air [Pa s], [59]	$\tilde{\mu}_\mathrm{g}^{\mathrm{air}}$	20.56×10^{-6}
Dynamic viscosity H_2 [Pa s], [60]	$\tilde{\mu}_\mathrm{g}^{\mathrm{H_2}}$	9.813×10^{-6}
Density air [kg m^{-3}], [59]	$\tilde{\rho}_\mathrm{g}^{\mathrm{air}}$	1.015
Density H_2 [kg m^{-3}], [60]	$\tilde{\rho}_\mathrm{g}^{\mathrm{H_2}}$	0.0706
Density liquid H_2O [kg m^{-3}], [59]	$\tilde{\rho}_\mathrm{l}$	977.75
Specific heat capacity air [J kg^{-1} K^{-1}], [59]	$\tilde{c}_\mathrm{g}^{\mathrm{air}}$	1009
Specific heat capacity H_2 [J kg^{-1} K^{-1}], [60]	$\tilde{c}_\mathrm{g}^{\mathrm{H_2}}$	14 419
Specific heat capacity N_2 [J kg^{-1} K^{-1}], [60]	$\tilde{c}_\mathrm{g}^{\mathrm{N_2}}$	1042
Specific heat capacity H_2O [J kg^{-1} K^{-1}], [59]	$\tilde{c}_\mathrm{g}^{\mathrm{H_2O}}$	1987
Specific heat capacity liquid H_2O [J kg^{-1} K^{-1}], [59]	$\tilde{c}_\mathrm{l}$	4188
Enthalpy of evaporation [J kg^{-1}], [59]	$\tilde{h}_\mathrm{lg}$	2333×10^3
Entropy change [J mol^{-1} K^{-1}], [61]	$\Delta\tilde{S}^\mathrm{C}$	−163.5
Thermal conductivity air [W m^{-1} K^{-1}], [59]	$\tilde{k}_\mathrm{air}$	0.029 51
Thermal conductivity H_2 [W m^{-1} K^{-1}], [60]	$\tilde{k}_{\mathrm{H_2}}$	0.206 88
Binary diffusion coefficient O_2–H_2O [m^2 s^{-1}], [23]	$\tilde{\mathscr{D}}_{\mathrm{O_2}-\mathrm{H_2O}}$	26.52×10^{-6}
Binary diffusion coefficient H_2–H_2O [m^2 s^{-1}], [23]	$\tilde{\mathscr{D}}_{\mathrm{H_2}-\mathrm{H_2O}}$	112.36×10^{-6}
Surface tension liquid H_2O [N m^{-1}], [59]	$\tilde{\zeta}_\mathrm{l}$	64.48×10^{-3}
Reference ionic conductivity [S m^{-1}]	$\tilde{\sigma}_\mathrm{r}$	0.2
Reference current density [A m^{-2}], [23]	$\tilde{i}_\mathrm{r}$	14 000

Because of Eq. (C.2), only two species mass balance (SMB) equations are required, i.e. for the reactant species $\alpha = \mathrm{H_2}, \mathrm{O_2}$ and $\mathrm{H_2O}$,

$$\int_{\tilde{V}} \frac{\partial((1-s_\mathrm{l})\tilde{\rho}_\mathrm{g}\xi_\mathrm{g}^{\alpha})}{\partial\tilde{t}}\,\mathrm{d}\tilde{V} + \oint_{\partial\tilde{V}} (1-s_\mathrm{l})\tilde{\rho}_\mathrm{g}\tilde{\mathbf{u}}_\mathrm{g}\xi_\mathrm{g}^{\alpha}\,\mathrm{d}\tilde{S} + \oint_{\partial\tilde{V}} \tilde{\mathbf{j}}_\mathrm{g}^{\alpha}\,\mathrm{d}\tilde{S} = 0\,, \tag{C.5}$$

$$\int_{\tilde{V}} \frac{\partial((1-s_\mathrm{l})\tilde{\rho}_\mathrm{g}\xi_\mathrm{g}^{\mathrm{H_2O}})}{\partial\tilde{t}}\,\mathrm{d}\tilde{V} + \oint_{\partial\tilde{V}} (1-s_\mathrm{l})\tilde{\rho}_\mathrm{g}\tilde{\mathbf{u}}_\mathrm{g}\xi_\mathrm{g}^{\mathrm{H_2O}}\,\mathrm{d}\tilde{S} + \oint_{\partial\tilde{V}} \tilde{\mathbf{j}}_\mathrm{g}^{\mathrm{H_2O}}\,\mathrm{d}S = -\int_{\tilde{V}} \tilde{m}_\mathrm{l}\,\mathrm{d}\tilde{V}\,. \tag{C.6}$$

It is further assumed that H_2, O_2 and N_2 are unsoluble in the liquid phase, such that $\xi_\mathrm{l}^{\mathrm{H_2O}} = 1$. Consequently, using Eq. (C.1), the liquid phase mass balance (LMB) can be written as

$$\int_{\tilde{V}} \frac{\partial(s_\mathrm{l}\tilde{\rho}_\mathrm{l})}{\partial\tilde{t}}\,\mathrm{d}\tilde{V} + \oint_{\partial\tilde{V}} s_\mathrm{l}\tilde{\rho}_\mathrm{l}\tilde{\mathbf{u}}_\mathrm{l}\,\mathrm{d}\tilde{S} = \int_{\tilde{V}} \tilde{m}_\mathrm{l}\,\mathrm{d}\tilde{V}\,. \tag{C.7}$$

Adding up the LMB and GMB, Eqs. (C.4) and (C.7), and applying the definitions for the multiphase mixture density $\tilde{\rho}_\mathrm{m}$ and velocity $\tilde{u}_\mathrm{m}$, Eq. (1), yields the total mass balance of the multiphase mixture (TMB),

$$\int_{\tilde{V}} \frac{\partial\tilde{\rho}_\mathrm{m}}{\partial\tilde{t}}\,\mathrm{d}\tilde{V} + \oint_{\partial\tilde{V}} \tilde{\rho}_\mathrm{m}\tilde{\mathbf{u}}_\mathrm{m}\,\mathrm{d}\tilde{S} = 0\,. \tag{C.8}$$

To model non-isothermal effects, one additional equation for the conservation of energy is required. The enthalpies of the gas/liquid phases $\tilde{h}_\mathrm{g}/\tilde{h}_\mathrm{l}$ and individual gas phase species $\tilde{h}_\mathrm{g}^{\gamma}$ are defined as follows,

$$\begin{aligned} &\tilde{h}_\mathrm{g} = \textstyle\sum_\gamma \xi_\mathrm{g}^{\gamma}\tilde{h}_\mathrm{g}^{\gamma}\,, && \tilde{h}_\mathrm{g}^{\alpha} = \tilde{c}_\mathrm{g}^{\alpha}(\tilde{T}-\tilde{T}_0)\,, \quad \alpha = \mathrm{H_2}, \mathrm{O_2} \\ &\tilde{h}_\mathrm{l} = \tilde{c}_\mathrm{l}(\tilde{T}-\tilde{T}_0)\,, && \tilde{h}_\mathrm{g}^{\mathrm{N_2}} = \tilde{c}_\mathrm{g}^{\mathrm{N_2}}(\tilde{T}-\tilde{T}_0)\,, \\ & && \tilde{h}_\mathrm{g}^{\mathrm{H_2O}} = \tilde{c}_\mathrm{l}(\tilde{T}_\mathrm{sat}-\tilde{T}_0) + \tilde{h}_\mathrm{lg} + \tilde{c}_\mathrm{g}^{\mathrm{H_2O}}(\tilde{T}-\tilde{T}_\mathrm{sat})\,. \end{aligned} \tag{C.9}$$

Here, $\tilde{c}_\mathrm{g}^{\gamma}$ and $\tilde{c}_\mathrm{l}$ denote the isobaric specific heat capacity of gaseous species γ and liquid H_2O, respectively, and $\tilde{h}_\mathrm{lg}$ is the latent heat of evaporation. $\tilde{T}$, $\tilde{T}_\mathrm{sat}$, and $\tilde{T}_0 = 298.15\,\mathrm{K}$ further denote the fluid's temperature, the saturation temperature (at which condensation occurs for a given partial pressure of H_2O in the gas phase), and the arbitrarily chosen reference temperature. Considering the individual phase mass balances, Eqs. (C.4) and (C.7), together with their associated enthalpies from Eq. (C.9), the total energy balance of the liquid and gas phase (= multiphase mixture) reads

$$\begin{aligned} &\int_{\tilde{V}} \frac{\partial(s_\mathrm{l}\tilde{\rho}_\mathrm{l}\tilde{h}_\mathrm{l} + (1-s_\mathrm{l})\tilde{\rho}_\mathrm{g}\tilde{h}_\mathrm{g})}{\partial\tilde{t}}\,\mathrm{d}\tilde{V} + \oint_{\partial\tilde{V}} (s_\mathrm{l}\tilde{\rho}_\mathrm{l}\tilde{h}_\mathrm{l}\tilde{\mathbf{u}}_\mathrm{l} + (1-s_\mathrm{l})\tilde{\rho}_\mathrm{g}\tilde{h}_\mathrm{g}\tilde{\mathbf{u}}_\mathrm{g})\,\mathrm{d}\tilde{S} = \\ &-\oint_{\partial\tilde{V}} \left(\sum_\gamma \tilde{\mathbf{j}}_\mathrm{g}^{\alpha}\tilde{h}_\mathrm{g}^{\gamma} + \tilde{\mathbf{q}}_\mathrm{m}\right)\mathrm{d}\tilde{S} + \int_{\tilde{V}} \tilde{m}_\mathrm{l}(\tilde{h}_\mathrm{l} - \tilde{h}_\mathrm{g}^{\mathrm{H_2O}})\,\mathrm{d}\tilde{V}\,. \end{aligned} \tag{C.10}$$

The two left hand side terms account for the accumulation and convective transport of the multiphase mixture's enthalpy, whereas the first right hand side term describes energy transport associated with the diffusive mass fluxes $\tilde{\mathbf{j}}_\mathrm{g}^{\gamma}$, in the gas phase Eq. (4), and the heat flux $\tilde{\mathbf{q}}_\mathrm{m}$ due to thermal

conduction in the multiphase mixture, Eq. (7). The last right hand side term constitutes the heat source due to phase change processes of H_2O and arises by considering Eq. (C.3). Throughout this work, material parameters such as the specific heat capacities and the latent heat of evaporation $\Delta\tilde{h}_{\mathrm{lg}} = \tilde{h}_{\mathrm{l}} - \tilde{h}_{\mathrm{g}}^{\mathrm{H_2O}}$ are assumed constant in the expected operating range of the PEMFC.

Appendix D. Governing model equations

D.1. Conservation of mass

To derive the continuity equation for the gas channel, Eq. (C.8) is applied to the red dashed control volume $\tilde{CV}$ shown in Fig. 2. Within the quasi-2D multiphase mixture framework the density $\tilde{\rho}_{\mathrm{m}}$ in the gas channel only depends on $\tilde{x}_1$ and we therefore obtain

$$\begin{aligned} 0 \;=\; & \tilde{W}_{\mathrm{GC}}\tilde{H}_{\mathrm{GC}} \int_{\tilde{x}_1^*}^{\tilde{x}_1^*+\Delta\tilde{x}_1} \frac{\partial\bar{\tilde{\rho}}_{\mathrm{m}}(\tilde{x}_1,\tilde{t})}{\partial\tilde{t}}\,\mathrm{d}\tilde{x}_1 - \int_0^{\tilde{W}_{\mathrm{GC}}}\int_0^{\tilde{H}_{\mathrm{GC}}} \tilde{\rho}_{\mathrm{m}}(\tilde{x}_1,\tilde{t})\tilde{u}_{\mathrm{m},1}(\tilde{\mathbf{x}},\tilde{t})\Big|_{\tilde{x}_1=\tilde{x}_1^*}\mathrm{d}\tilde{x}_2\,\mathrm{d}\tilde{x}_3 \\ & + \int_0^{\tilde{W}_{\mathrm{GC}}}\int_0^{\tilde{H}_{\mathrm{GC}}} \tilde{\rho}_{\mathrm{m}}(\tilde{x}_1,\tilde{t})\tilde{u}_{\mathrm{m},1}(\tilde{\mathbf{x}},\tilde{t})\Big|_{\tilde{x}_1=\tilde{x}_1^*+\Delta\tilde{x}_1}\mathrm{d}\tilde{x}_2\,\mathrm{d}\tilde{x}_3 + \int_0^{\tilde{W}_{\mathrm{GC}}}\int_{\tilde{x}_1^*}^{\tilde{x}_1^*+\Delta\tilde{x}_1} \tilde{\rho}_{\mathrm{m}}(\tilde{x}_1,\tilde{t})\tilde{u}_{\mathrm{m},2}(\tilde{\mathbf{x}},\tilde{t})\Big|_{\tilde{x}_2=\tilde{H}_{\mathrm{GC}}}\mathrm{d}\tilde{x}_1\,\mathrm{d}\tilde{x}_3\,. \end{aligned} \tag{D.1}$$

Due to the continuity of the total mixture mass flux through the interface between the gas channel and the GDL at $\tilde{x}_2 = \tilde{H}_{\mathrm{GC}}$, the last term can be written in terms of GDL variables

$$\int_0^{\tilde{W}_{\mathrm{GC}}}\int_{\tilde{x}_1^*}^{\tilde{x}_1^*+\Delta\tilde{x}_1} \tilde{\rho}_{\mathrm{m}}(\tilde{x}_1,\tilde{t})\tilde{u}_{\mathrm{m},2}(\tilde{\mathbf{x}},\tilde{t})\Big|_{\tilde{x}_2=\tilde{H}_{\mathrm{GC}}}\mathrm{d}\tilde{x}_1\,\mathrm{d}\tilde{x}_3 = \int_0^{\tilde{W}_{\mathrm{GDL}}}\int_{\tilde{x}_1^*}^{\tilde{x}_1^*+\Delta\tilde{x}_1} \varepsilon\bar{\tilde{\rho}}_{\mathrm{m}}^{\mathrm{GDL}}(\tilde{x}_1,\tilde{t})\tilde{u}_{\mathrm{m},2}^{\mathrm{GDL}}(\tilde{\mathbf{x}},\tilde{t})\Big|_{\tilde{x}_2=\tilde{H}_{\mathrm{GC}}}\mathrm{d}\tilde{x}_1\,\mathrm{d}\tilde{x}_3\,. \tag{D.2}$$

To evaluate the volume integral in Eq. (D.1), the GC density $\bar{\tilde{\rho}}(\tilde{x}_1,\tilde{t})$ is approximated with the value at the centre of the control volume $\bar{\tilde{\rho}}(\tilde{x}_1+\Delta\tilde{x}_1/2,\tilde{t})$, since $\Delta\tilde{x}_1/\tilde{L} \ll 1$. Further, using the definition of the cross-sectional averaged velocity $\bar{\tilde{u}}_{\mathrm{m},1}(\tilde{x}_1,\tilde{t})$, Eq. (2), and analogue for $\bar{\tilde{u}}_{\mathrm{m},2}^{\mathrm{GDL}}(\tilde{x}_2,\tilde{t})$, yields:

$$\begin{aligned} 0 \;=\; & \tilde{W}_{\mathrm{GC}}\tilde{H}_{\mathrm{GC}}\left\{\Delta\tilde{x}_1\frac{\partial\bar{\tilde{\rho}}_{\mathrm{m}}(\tilde{x}_1,\tilde{t})}{\partial\tilde{t}}\Big|_{\tilde{x}_1=\tilde{x}_1^*+\Delta\tilde{x}_1/2} + \left[\bar{\tilde{\rho}}_{\mathrm{m}}(\tilde{x}_1,\tilde{t})\bar{\tilde{u}}_{\mathrm{m},1}(\tilde{x}_1,\tilde{t})\Big|_{\tilde{x}_1=\tilde{x}_1^*+\Delta\tilde{x}_1} - \bar{\tilde{\rho}}_{\mathrm{m}}(\tilde{x}_1,\tilde{t})\bar{\tilde{u}}_{\mathrm{m},1}(\tilde{x}_1,\tilde{t})\Big|_{\tilde{x}_1=\tilde{x}_1^*}\right]\right\} \\ & + \tilde{W}_{\mathrm{GDL}}\Delta\tilde{x}_1\varepsilon\bar{\tilde{\rho}}_{\mathrm{m}}^{\mathrm{GDL}}(\tilde{x}_1,\tilde{t})\bar{\tilde{u}}_{\mathrm{m},2}^{\mathrm{GDL}}(\tilde{x}_1,\tilde{t})\Big|_{\tilde{x}_2=\tilde{H}_{\mathrm{GC}}}\,. \end{aligned} \tag{D.3}$$

The final differential form for the quasi-1D continuity equation is found by Taylor series expansion of the time derivative and the square bracket at $\tilde{x}_1^*$:

$$\frac{\partial\bar{\tilde{\rho}}_{\mathrm{m}}}{\partial\tilde{t}} + \frac{\partial(\bar{\tilde{\rho}}_{\mathrm{m}}\bar{\tilde{u}}_{\mathrm{m},1})}{\partial\tilde{x}_1} = -\frac{\tilde{W}_{\mathrm{GDL}}}{\tilde{W}_{\mathrm{GC}}\tilde{H}_{\mathrm{GC}}}\,\varepsilon\bar{\tilde{\rho}}_{\mathrm{m}}^{\mathrm{GDL}}\bar{\tilde{u}}_{\mathrm{m},2}^{\mathrm{GDL}}\,. \tag{D.4}$$

A non-dimensional form of Eq. (D.4) is obtained by introducing characteristic variables for the mixture density $\bar{\tilde{\rho}}_{\mathrm{m}}$, the mixture velocity $\bar{\tilde{u}}_{\mathrm{m}}$, the spatial coordinate $\tilde{x}_1$, and the time $\tilde{t}$:

$$\bar{\tilde{\rho}}_{\mathrm{m}} = \tilde{\rho}_{\mathrm{air}}\rho_{\mathrm{m}}\,,\quad \bar{\tilde{u}}_{\mathrm{m},1} = \tilde{u}_{1,\mathrm{r}}u_{\mathrm{m},1}\,,\quad \tilde{x}_1 = \tilde{L}x_1\,,\quad \tilde{t} = \frac{\tilde{L}}{\tilde{u}_{1,\mathrm{r}}}t\,,\quad \bar{\tilde{\rho}}_{\mathrm{m}}^{\mathrm{GDL}} = \tilde{\rho}_{\mathrm{air}}\rho_{\mathrm{m}}^{\mathrm{GDL}}\,,\quad \bar{\tilde{u}}_{\mathrm{m},2}^{\mathrm{GDL}} = \frac{\tilde{\mathscr{D}}_{\mathrm{O_2,H_2O}}}{\tilde{H}_{\mathrm{GDL}}}u_{\mathrm{m},2}\,. \tag{D.5}$$

The dimensionless form of the continuity equation then finally reads

$$\frac{\partial\rho_{\mathrm{m}}}{\partial t} + \frac{\partial(\rho_{\mathrm{m}}u_{\mathrm{m},1})}{\partial x_1} = -K_{\mathrm{T1}}\,\varepsilon\rho_{\mathrm{m}}^{\mathrm{GDL}}u_{\mathrm{m},2}^{\mathrm{GDL}}\,, \tag{D.6}$$

where the bar indicating averaged quantities have been omitted for better readability and K_{T1} represents the dimensionless group formed by the introduction of characteristic reference quantities,

$$K_{\mathrm{T1}} = \frac{\tilde{W}_{\mathrm{GDL}}\tilde{L}\tilde{\mathscr{D}}_{\mathrm{O_2,H_2O}}}{\tilde{W}_{\mathrm{GC}}\tilde{H}_{\mathrm{GC}}\tilde{u}_{1,\mathrm{r}}}\,. \tag{D.7}$$

In a similar manner, the continuity equation for the GDL is found by evaluating Eq. (C.8) for a GDL control volume. Since there exist no side-walls between individual inner slices, the velocity profile and the density are assumed to depend on $\tilde{x}_2$ only and thus the GDL effectively is treated fully 1D. Here, the coupling with the GC is implemented in terms of boundary conditions at the corresponding interface, see Section 2.6. The dimensionless form of the TMB for the GDL finally reads

$$\frac{\partial\rho_{\mathrm{m}}}{\partial t} + \frac{\partial(\rho_{\mathrm{m}}u_{\mathrm{m},2})}{\partial x_2} = 0\,. \tag{D.8}$$

D.2. Liquid phase mass balance

D.2.1. Gas channel

The procedure to obtain the quasi-1D formulation of the liquid phase mass balance for the gas channel is equivalent to that of the total mass balance. Therefore, it will only be briefly discussed here. Evaluating the integrals of Eq. (C.7) for a small gas channel volume element in a similar fashion to the TMB under the assumption of constant liquid water density $\tilde{\rho}_{\mathrm{l}}$ yields

$$\tilde{\rho}_{\mathrm{l}}\left[\frac{\partial\bar{s}_{\mathrm{l}}}{\partial\tilde{t}} + \frac{\partial(\bar{s}_{\mathrm{l}}\bar{\tilde{u}}_{\mathrm{l},1})}{\partial\tilde{x}_1}\right] = \bar{\tilde{m}}_{\mathrm{l}} - \frac{1}{\tilde{H}_{\mathrm{GC}}}\left[\bar{s}_{\mathrm{l}}\bar{\tilde{\rho}}_{\mathrm{l}}\bar{\tilde{u}}_{\mathrm{l},2}\right]\Big|_{\tilde{x}_2=\tilde{H}_{\mathrm{GC}}}\,, \tag{D.9}$$

where the last right hand side term represents the liquid water mass flux at the gas channels boundary adjacent to the GDL. Applying the coupling condition, Eq. (52), that ensures the conservation of liquid mass across the gas channel–GDL interface, and the relationship between the liquid phase and the multiphase mixture velocity in the GDL, Eq. (26), then gives

$$\tilde{\rho}_{\mathrm{l}}\left[\frac{\partial \bar{s}_{\mathrm{l}}}{\partial \tilde{t}}+\frac{\partial(\bar{s}_{\mathrm{l}}\bar{\tilde{u}}_{\mathrm{m},1})}{\partial \tilde{x}_1}\right]=\bar{\tilde{m}}_{\mathrm{l}}-\frac{\tilde{W}_{\mathrm{GDL}}}{\tilde{W}_{\mathrm{GC}}\tilde{H}_{\mathrm{GC}}}\left[\varepsilon\bar{\zeta}_{\mathrm{l}}\bar{\tilde{\rho}}_{\mathrm{m}}\bar{\tilde{u}}_{\mathrm{m},2}+\bar{\tilde{\psi}}_{\mathrm{l},2}\right]_{\mathrm{GDL}}, \tag{D.10}$$

where the right hand side bracket contains only GDL variables and the homogeneous flow condition, $\tilde{u}_{\mathrm{m},1}=\tilde{u}_{\mathrm{l},1}=\tilde{u}_{\mathrm{g},1}$. By means of the characteristic reference values in Table B.8, the dimensionless formulation for the liquid phase mass balance in the gas channel finally yields

$$\frac{\partial s_{\mathrm{l}}}{\partial t}+\frac{\partial(s_{\mathrm{l}}u_{\mathrm{m},1})}{\partial x_1}=K_{\rho}\dot{m}_{\mathrm{l}}-\left[K_{\mathrm{L}1}\varepsilon\zeta_{\mathrm{l}}\rho_{\mathrm{m}}u_{\mathrm{m},2}+K_{\mathrm{L}2}\psi_{\mathrm{l}}\right]_{\mathrm{GDL}}. \tag{D.11}$$

D.2.2. Gas diffusion layer

Evaluating the integral form of the liquid phase mass balance, Eq. (C.7), for a small control volume $\tilde{CV}$ of the GDL yields a differential form similar to Eq. (D.9), in which the coupling source term vanishes. With the definition of the phase velocity and the introduction of characteristic reference quantities one finds the dimensionless form of the LMB in the GDL,

$$\varepsilon\frac{\partial s_{\mathrm{l}}}{\partial t}+\varepsilon\frac{\partial\left(\zeta_{\mathrm{l}}\rho_{\mathrm{m}}u_{\mathrm{m},2}\right)}{\partial x_2}+K_{\mathrm{L}1}\frac{\partial\psi_{\mathrm{l},2}}{\partial x_2}=\varepsilon K_{\rho}\dot{m}_{\mathrm{l}}, \tag{D.12}$$

where the porosity ε accounts for the pore space available to the fluid and the dimensionless capillary diffusion flux is given by

$$\psi_{\mathrm{l},2}=\frac{\zeta_{\mathrm{l}}(1-\zeta_{\mathrm{l}})\mathscr{J}'(s_{\mathrm{l}})}{\nu_{\mathrm{m}}}\frac{\partial s_{\mathrm{l}}}{\partial x_2}. \tag{D.13}$$

D.3. Gas phase mass balance

Identical to the LMB one finds for the mass balance of the gas phase GMB,

$$\frac{\partial(1-\bar{s}_{\mathrm{l}})\bar{\tilde{\rho}}_{\mathrm{g}}}{\partial \tilde{t}}+\frac{\partial((1-\bar{s}_{\mathrm{l}})\bar{\tilde{\rho}}_{\mathrm{g}}\bar{\tilde{u}}_{\mathrm{m},1})}{\partial \tilde{x}_1}=-\bar{\tilde{m}}_{\mathrm{l}}-\frac{1}{\tilde{H}_{\mathrm{GC}}}\left[\bar{\tilde{\rho}}_{\mathrm{g}}\bar{\tilde{u}}_{\mathrm{g},2}\right]\Big|_{\tilde{x}_2=\tilde{H}_{\mathrm{GC}}}, \tag{D.14}$$

where the right hand side coupling term again can be expressed with GDL variables only using the conservation of the gas mass across the GC-GDL interface,

$$\frac{\partial(1-\bar{s}_{\mathrm{l}})\bar{\tilde{\rho}}_{\mathrm{g}}}{\partial \tilde{t}}+\frac{\partial((1-\bar{s}_{\mathrm{l}})\bar{\tilde{\rho}}_{\mathrm{g}}\bar{\tilde{u}}_{\mathrm{m},1})}{\partial \tilde{x}_1}=-\bar{\tilde{m}}_{\mathrm{l}}-\frac{\tilde{W}_{\mathrm{GDL}}}{\tilde{W}_{\mathrm{GC}}\tilde{H}_{\mathrm{GC}}}\left[\varepsilon(1-\zeta_{\mathrm{l}})\bar{\tilde{\rho}}_{\mathrm{m}}\bar{\tilde{u}}_{\mathrm{m},2}-\bar{\tilde{\psi}}_{\mathrm{l},2}\right]_{\mathrm{GDL}}. \tag{D.15}$$

The GMB is further used to simplify the gas species mass balances, however, it does not appear as a governing equation in the LIT model implementation.

D.4. Species mass balance

D.4.1. Gas channel

Evaluating the integral formulation of the species balance for reactant $\alpha=\mathrm{H}_2,\mathrm{O}_2$, Eq. (C.5), follows the same approach shown for the mass balances above. On the cathode side one finds for reactant O_2:

$$\frac{\partial((1-\bar{s}_{\mathrm{l}})\bar{\tilde{\rho}}_{\mathrm{g}}\bar{\tilde{\xi}}_{\mathrm{g}}^{\mathrm{O}_2})}{\partial \tilde{t}}+\frac{\partial((1-\bar{s}_{\mathrm{l}})\bar{\tilde{\rho}}_{\mathrm{g}}\bar{\tilde{\xi}}_{\mathrm{g}}^{\mathrm{O}_2}\bar{\tilde{u}}_{\mathrm{g},1})}{\partial \tilde{x}_1}+\frac{\partial\bar{\tilde{j}}_{\mathrm{g},1}^{\mathrm{O}_2}}{\partial \tilde{x}_1}=-\frac{1}{\tilde{H}_{\mathrm{GC}}}\left[(1-\bar{s}_{\mathrm{l}})\bar{\tilde{\rho}}_{\mathrm{g}}\bar{\tilde{\xi}}_{\mathrm{g}}^{\mathrm{O}_2}\tilde{u}_{\mathrm{g},2}+\tilde{j}_{\mathrm{g},2}^{\mathrm{O}_2}\right]\Big|_{\tilde{x}_2=\tilde{H}_{\mathrm{GC}}}, \tag{D.16}$$

and for gaseous $\mathrm{H_2O}$:

$$\frac{\partial((1-\bar{s}_{\mathrm{l}})\bar{\tilde{\rho}}_{\mathrm{g}}\bar{\tilde{\xi}}_{\mathrm{g}}^{\mathrm{H_2O}})}{\partial \tilde{t}}+\frac{\partial((1-\bar{s}_{\mathrm{l}})\bar{\tilde{\rho}}_{\mathrm{g}}\bar{\tilde{\xi}}_{\mathrm{g}}^{\mathrm{H_2O}}\bar{\tilde{u}}_{\mathrm{g},1})}{\partial \tilde{x}_1}+\frac{\partial\bar{\tilde{j}}_{\mathrm{g},1}^{\mathrm{H_2O}}}{\partial \tilde{x}_1}=-\tilde{m}_{\mathrm{l}}-\frac{1}{\tilde{H}_{\mathrm{GC}}}\left[(1-\bar{s}_{\mathrm{l}})\bar{\tilde{\rho}}_{\mathrm{g}}\bar{\tilde{\xi}}_{\mathrm{g}}^{\mathrm{H_2O}}\tilde{u}_{\mathrm{g},2}+\tilde{j}_{\mathrm{g},2}^{\mathrm{H_2O}}\right]\Big|_{\tilde{x}_2=\tilde{H}_{\mathrm{GC}}}. \tag{D.17}$$

The assumption of homogeneous flow together with the coupling condition for the GC-GDL interface, Eq. (53), further yields for O_2

$$\frac{\partial((1-\bar{s}_{\mathrm{l}})\bar{\tilde{\rho}}_{\mathrm{g}}\bar{\tilde{\xi}}_{\mathrm{g}}^{\mathrm{O}_2})}{\partial \tilde{t}}+\frac{\partial((1-\bar{s}_{\mathrm{l}})\bar{\tilde{\rho}}_{\mathrm{g}}\bar{\tilde{\xi}}_{\mathrm{g}}^{\mathrm{O}_2}\bar{\tilde{u}}_{\mathrm{m},1})}{\partial \tilde{x}_1}+\frac{\partial\bar{\tilde{j}}_{\mathrm{g},1}^{\mathrm{O}_2}}{\partial \tilde{x}_1}=-\frac{\tilde{W}_{\mathrm{GDL}}}{\tilde{W}_{\mathrm{GC}}\tilde{H}_{\mathrm{GC}}}\left[\varepsilon(1-\bar{\zeta}_{\mathrm{l}})\bar{\tilde{\rho}}_{\mathrm{m}}\bar{\tilde{\xi}}_{\mathrm{g}}^{\mathrm{O}_2}\bar{\tilde{u}}_{\mathrm{m},2}-\bar{\tilde{\psi}}_{\mathrm{l},2}\bar{\tilde{\xi}}_{\mathrm{g}}^{\mathrm{O}_2}+\bar{\tilde{j}}_{\mathrm{g},2}^{\mathrm{O}_2}\right]_{\mathrm{GDL}}, \tag{D.18}$$

where the bracket on the right hand side contains only GDL variables. This can further be simplified by applying the GMB, Eq. (D.15), to yield

$$(1-\bar{s})\bar{\tilde{\rho}}_{\mathrm{g}}\left[\frac{\partial\bar{\tilde{\xi}}_{\mathrm{g}}^{\mathrm{O}_2}}{\partial \tilde{t}}+\bar{\tilde{u}}_{\mathrm{m},1}\frac{\partial\bar{\tilde{\xi}}_{\mathrm{g}}^{\mathrm{O}_2}}{\partial \tilde{x}_1}\right]+\frac{\partial\bar{\tilde{j}}_{\mathrm{g},1}^{\mathrm{O}_2}}{\partial \tilde{x}_1}=\bar{\tilde{m}}_{\mathrm{l}}\bar{\xi}^{\mathrm{O}_2}-\frac{\tilde{W}_{\mathrm{GDL}}}{\tilde{W}_{\mathrm{GC}}\tilde{H}_{\mathrm{GC}}}\bar{j}_{\mathrm{g},2}^{\mathrm{O}_2}\Big|_{\mathrm{GDL}}. \tag{D.19}$$

Introducing characteristic reference quantities finally yields the O_2 species mass balance in dimensionless form,

$$(1-\bar{s}_{\mathrm{l}})\rho_{\mathrm{g}}\left[\frac{\partial\xi_{\mathrm{g}}^{\mathrm{O}_2}}{\partial t}+u_{\mathrm{m},1}\frac{\partial\xi_{\mathrm{g}}^{\mathrm{O}_2}}{\partial x_1}\right]+K_{\mathrm{S}1}\frac{\partial j_{\mathrm{g},1}^{\mathrm{O}_2}}{\partial x_1}=\dot{m}_{\mathrm{l}}\xi^{\mathrm{O}_2}-K_{\mathrm{S}2}j_{\mathrm{g},2}^{\mathrm{O}_2}\Big|_{\mathrm{GDL}}. \tag{D.20}$$

In a similar manner one finds the dimensionless species mass balance for gaseous $\mathrm{H_2O}$ in the gas channel:

$$(1-\bar{s}_{\mathrm{l}})\bar{\rho}_{\mathrm{g}}\left[\frac{\partial\xi_{\mathrm{g}}^{\mathrm{H_2O}}}{\partial \tilde{t}}+u_{\mathrm{m},1}\frac{\partial\xi_{\mathrm{g}}^{\mathrm{H_2O}}}{\partial x_1}\right]+K_{\mathrm{S}2}\frac{\partial j_{\mathrm{g},1}^{\mathrm{H_2O}}}{\partial x_1}=\dot{m}_{\mathrm{l}}\left(\xi_{\mathrm{g}}^{\mathrm{H_2O}}-1\right)-K_{\mathrm{S}2}j_{\mathrm{g},2}^{\mathrm{H_2O}}\Big|_{\mathrm{GDL}}. \tag{D.21}$$

D.4.2. Gas diffusion layer

Evaluating the integral formulation of the species mass balance for gaseous H_2O, Eq. ((C.1), for a small GDL $\tilde{CV}$ yield the differential form,

$$\varepsilon\frac{\partial((1-\bar{s}_\mathrm{l})\tilde{\rho}_\mathrm{g}\xi_\mathrm{g}^{\mathrm{H_2O}})}{\partial\tilde{t}}+\varepsilon\frac{\partial((1-\bar{s}_\mathrm{l})\tilde{\rho}_\mathrm{g}\xi_\mathrm{g}^{\mathrm{H_2O}}\tilde{u}_{\mathrm{g},2})}{\partial\tilde{x}_2}=-\varepsilon\tilde{\dot{m}}_\mathrm{l}-\frac{\partial j_2^{\mathrm{H_2O}}}{\partial\tilde{x}_2}\ . \tag{D.22}$$

The dimensionless formulation is found by applying Eq. (26) and introducing characteristic reference quantities,

$$\varepsilon\frac{\partial((1-\bar{s}_\mathrm{l})\rho_\mathrm{g}\xi_\mathrm{g}^{\mathrm{H_2O}})}{\partial t}+\varepsilon\frac{\partial((1-\zeta_\mathrm{l})\rho_\mathrm{m}\xi_\mathrm{g}^{\mathrm{H_2O}}u_{\mathrm{m},2})}{\partial x_2}=-\varepsilon\dot{m}_\mathrm{l}-\frac{\partial j_{\mathrm{g},2}^{\mathrm{H_2O}}}{\partial x_2}+\frac{\partial(\psi_{\mathrm{l},2}\xi_\mathrm{g}^{\mathrm{H_2O}})}{\partial x_2}\ . \tag{D.23}$$

Similarly, for reactant species α one finds

$$\varepsilon\frac{\partial((1-\bar{s}_\mathrm{l})\rho_\mathrm{g}\xi_\mathrm{g}^{\alpha})}{\partial t}+\varepsilon\frac{\partial((1-\zeta_\mathrm{l})\rho_\mathrm{m}\xi_\mathrm{g}^{\alpha}u_{\mathrm{m},2})}{\partial x_2}=-\frac{\partial j_{\mathrm{g},2}^{\alpha}}{\partial x_2}+\frac{\partial(\psi_{\mathrm{l},2}\xi_\mathrm{g}^{\alpha})}{\partial x_2}\ . \tag{D.24}$$

D.5. Energy balance

D.5.1. Gas channel

Similar to the equations for the conservation of mass, the quasi-1D formulation of the energy balance for the GC is found by evaluating Eq. (C.10) for a small channel volume element (see Fig. 2). Due to the assumption of a constant temperature in $\tilde{x}_2$- and $\tilde{x}_3$-direction, heat fluxes depend on $\tilde{x}_1$ only. Therefore, evaluating the surface integral for the heat flux $\tilde{\mathbf{q}}_\mathrm{m}(\tilde{x}_1,\tilde{t})$ in the multiphase mixture yields:

$$\oint_{\tilde{CV}}\tilde{\mathbf{q}}_\mathrm{m}(\tilde{x}_1,\tilde{t})\,\mathrm{d}\tilde{S}=+\tilde{W}_\mathrm{GC}\tilde{H}_\mathrm{GC}\left(\tilde{q}_{\mathrm{m},1}(\tilde{x}_1,\tilde{t})\,\Big|_{\tilde{x}_1=\tilde{x}_1^*+\Delta\tilde{x}_1}-\tilde{q}_{\mathrm{m},1}(\tilde{x}_1,\tilde{t})\,\Big|_{\tilde{x}_1=\tilde{x}_1^*}\right) \tag{D.25}$$

$$-\tilde{W}_\mathrm{GC}\int_{\tilde{x}_1^*}^{\tilde{x}_1^*+\Delta\tilde{x}_1}\tilde{q}_{\mathrm{m},2}(\tilde{x}_1,\tilde{t})\,\Big|_{\tilde{x}_2=0}\,\mathrm{d}\tilde{x}_1+\tilde{W}_\mathrm{GC}\int_{\tilde{x}_1^*}^{\tilde{x}_1^*+\Delta\tilde{x}_1}\tilde{q}_{\mathrm{m},2}(\tilde{x}_1,\tilde{t})\,\Big|_{\tilde{x}_2=\tilde{H}_\mathrm{GC}}\,\mathrm{d}\tilde{x}_1 \tag{D.26}$$

$$-\tilde{H}_\mathrm{GC}\int_{\tilde{x}_1^*}^{\tilde{x}_1^*+\Delta\tilde{x}_1}\tilde{q}_{\mathrm{m},3}(\tilde{x}_1,\tilde{t})\,\Big|_{\tilde{x}_3=0}\,\mathrm{d}\tilde{x}_1+\tilde{H}_\mathrm{GC}\int_{\tilde{x}_1^*}^{\tilde{x}_1^*+\Delta\tilde{x}_1}\tilde{q}_{\mathrm{m},3}(\tilde{x}_1,\tilde{t})\,\Big|_{\tilde{x}_1=\tilde{W}_\mathrm{GC}}\,\mathrm{d}\tilde{x}_1\ . \tag{D.27}$$

Here, the first line represents Fourier's heat fluxes, Eq. (7), the second and third line account for the heat fluxes between the fluid and the adjacent BP/GDL, Eq. (14). To evaluate the integrals, the heat fluxes $\bar{\tilde{q}}_{\mathrm{m},a}(\tilde{x}_1,\tilde{t})$ are approximated with the respective value at the centre of the control volume, $\bar{\tilde{q}}_{\mathrm{m},a}(\tilde{x}_1+\Delta x_1/2,\tilde{t})$, since $\Delta\tilde{x}_1/\tilde{L}\ll 1$. The evaluation of the integrals for the enthalpy fluxes due to mass transport by convection and diffusion is similar to the respective mass balance equations using the definition of the cross-sectional averaged velocity, Eq. (2). Further, applying Taylor series expansions at $\tilde{x}_1^*$ yields the differential form of the energy balance

$$\frac{\partial(\bar{s}_\mathrm{l}\bar{\tilde{\rho}}_\mathrm{l}\bar{\tilde{h}}_\mathrm{l}+(1-\bar{s}_\mathrm{l})\bar{\tilde{\rho}}_\mathrm{g}\bar{\tilde{h}}_\mathrm{g})}{\partial\tilde{t}}+\frac{\partial(\bar{s}_\mathrm{l}\bar{\tilde{\rho}}_\mathrm{l}\bar{\tilde{h}}_\mathrm{l}\bar{\tilde{u}}_{\mathrm{m},1}+(1-\bar{s}_\mathrm{l})\bar{\tilde{\rho}}_\mathrm{g}\bar{\tilde{h}}_\mathrm{g}\bar{\tilde{u}}_{\mathrm{m},1})}{\partial\tilde{x}_1}+\sum_\gamma\frac{\partial(\bar{\tilde{j}}_{\mathrm{g},1}^{\gamma}\bar{\tilde{h}}_\mathrm{g}^{\gamma})}{\partial\tilde{x}_1}+\frac{\partial\bar{\tilde{q}}_{\mathrm{m},1}}{\partial\tilde{x}_1}=$$

$$\bar{\tilde{m}}_\mathrm{l}\left(\bar{\tilde{h}}_\mathrm{l}-\bar{\tilde{h}}_\mathrm{g}\right)-\frac{1}{\tilde{H}_\mathrm{GC}}\bar{\tilde{q}}_{\mathrm{m},2}^{\mathrm{BP}}-\frac{1}{\tilde{H}_\mathrm{GC}}\bar{\tilde{q}}_{\mathrm{m},2}^{\mathrm{GDL}}-\frac{2}{\tilde{W}_\mathrm{GC}}\bar{\tilde{q}}_{\mathrm{m},2}^{\mathrm{BP}}-\frac{1}{\tilde{H}_\mathrm{GC}}\left[\bar{s}_\mathrm{l}\bar{\tilde{\rho}}_\mathrm{l}\bar{\tilde{h}}_\mathrm{l}\bar{\tilde{u}}_{\mathrm{l},2}+(1-s_\mathrm{l})\bar{\tilde{\rho}}_\mathrm{g}\bar{\tilde{h}}_\mathrm{g}\bar{\tilde{u}}_{\mathrm{g},\mathrm{g}}+\sum_\gamma\bar{\tilde{j}}_{\mathrm{g},2}^{\gamma}\bar{\tilde{h}}_\mathrm{g}^{\gamma}\right]\Big|_{\tilde{x}_2=\tilde{H}_\mathrm{GC}}\ . \tag{D.28}$$

This equation can be simplified by applying the definition of the enthalpies, Eq. (C.9), as well as the closure condition for the diffusive fluxes, Eq. (5), and inserting the mass balances for the liquid phase, as well as that for the gaseous species O_2 and H_2O, Eqs. (D.9), (D.16), and (D.17), respectively, to yield

$$\bar{\tilde{\rho}}_\mathrm{m}\bar{\tilde{c}}_\mathrm{m}\left[\frac{\partial\bar{\tilde{T}}}{\partial\tilde{t}}+\bar{\tilde{u}}_{\mathrm{m},1}\frac{\partial\bar{\tilde{T}}}{\partial\tilde{x}_1}\right]+(1-\bar{s}_\mathrm{l})\bar{\tilde{\rho}}_\mathrm{g}\bar{\xi}_\mathrm{g}^{\mathrm{H_2O}}\left(\bar{\tilde{c}}_\mathrm{l}-\bar{\tilde{c}}_\mathrm{g}^{\mathrm{H_2O}}\right)\left[\frac{\partial\bar{\tilde{T}}_\mathrm{sat}}{\partial\tilde{t}}+\bar{\tilde{u}}_{\mathrm{m},1}\frac{\partial\bar{\tilde{T}}_\mathrm{sat}}{\partial\tilde{x}_1}\right]-\frac{\partial}{\partial x_1}\left(\tilde{k}_\mathrm{m}\frac{\partial\tilde{T}}{\partial x_1}\right)=$$

$$-\bar{\tilde{j}}_{\mathrm{g},1}^{\mathrm{H_2O}}\left[\left(\bar{\tilde{c}}_\mathrm{g}^{\mathrm{H_2O}}-\bar{\tilde{c}}_\mathrm{g}^{\mathrm{N_2}}\right)\frac{\partial\bar{\tilde{T}}}{\partial\tilde{x}_1}+\left(\bar{\tilde{c}}_\mathrm{l}-\bar{\tilde{c}}_\mathrm{g}^{\mathrm{H_2O}}\right)\frac{\partial\bar{\tilde{T}}_\mathrm{sat}}{\partial\tilde{x}_1}\right]-\bar{\tilde{j}}_{\mathrm{g},1}^{\mathrm{O_2}}\left(\bar{\tilde{c}}_\mathrm{g}^{\mathrm{O_2}}-\bar{\tilde{c}}_\mathrm{g}^{\mathrm{N_2}}\right)\frac{\partial\bar{\tilde{T}}}{\partial\tilde{x}_1}$$

$$-\frac{2\tilde{\alpha}}{\tilde{W}_\mathrm{GC}}\left(\bar{\tilde{T}}-\tilde{T}^{\mathrm{BP}}\right)-\frac{\tilde{\alpha}}{\tilde{H}_\mathrm{GC}}\left(\bar{\tilde{T}}-\tilde{T}^{\mathrm{BP}}\right)-\frac{\tilde{\alpha}_\mathrm{GDL}}{\tilde{H}_\mathrm{GC}}\left(\bar{\tilde{T}}-\tilde{T}^{\mathrm{GDL}}\right). \tag{D.29}$$

Here, $\tilde{c}_\mathrm{m}$ is the mixture-averaged isobaric specific heat capacity defined by

$$\tilde{\rho}_\mathrm{m}\tilde{c}_\mathrm{m}=s_\mathrm{l}\tilde{\rho}_\mathrm{l}\tilde{c}_\mathrm{l}+(1-s_\mathrm{l})\tilde{\rho}_\mathrm{g}\sum_\gamma\xi_\mathrm{g}^{\gamma}c_\mathrm{g}^{\gamma}\ , \tag{D.30}$$

and $\tilde{\alpha}$ is the heat transfer coefficient between the fluid and gas channel side walls. By means of characteristic reference quantities, the dimensionless form of the multiphase mixture energy balance in the GC finally reads

$$\rho_\mathrm{m}c_\mathrm{m}\left[\frac{\partial T}{\partial t}+u_{\mathrm{m},1}\frac{\partial T}{\partial x_1}\right]+K_{\mathrm{E1}}\,(1-s_\mathrm{l})\rho_\mathrm{g}\xi_\mathrm{g}^{\mathrm{H_2O}}\left[\frac{\partial T_\mathrm{sat}}{\partial t}+u_{\mathrm{m},1}\frac{\partial T_\mathrm{sat}}{\partial x_1}\right]+K_{\mathrm{E2}}\,j_{\mathrm{g},1}^{\mathrm{O_2}}\frac{\partial T}{\partial x_1}+j_{\mathrm{g},1}^{\mathrm{H_2O}}\left[K_{\mathrm{E3}}\frac{\partial T}{\partial x_1}+K_{\mathrm{E4}}\frac{\partial T_\mathrm{sat}}{\partial x_1}\right]$$

$$=-(K_{\mathrm{E5}}+K_{\mathrm{E6}})(T-T^{\mathrm{BP}})-K_{\mathrm{E7}}(T-T^{\mathrm{GDL}})\,, \tag{D.31}$$

where the term accounting for Fourier's thermal conduction has been dropped due to its associated negligibly small dimensionless group, e.g. at the cathode side,

$$K_\mathrm{F}=\frac{\tilde{k}_\mathrm{r}}{\tilde{L}\,\tilde{\rho}_\mathrm{r}\,\tilde{u}_{\mathrm{l},\mathrm{r}}\,\tilde{c}_\mathrm{r}}=5.66\times10^{-3}\,. \tag{D.32}$$

D.5.2. Gas diffusion layer

Within the GDL, the enthalpy of the porous matrix

$$\tilde{h}_{\mathrm{GDL}} = \tilde{c}_{\mathrm{GDL}}(\tilde{T} - \tilde{T}_0) \ , \tag{D.33}$$

has to be additionally accounted for in the first term of the energy balance, Eq. (C.10). Here, $\tilde{c}_{\mathrm{GDL}}$ represents the isobaric specific heat capacity of the GDL material. Due to the absence of sidewalls the evaluation of the integrals is straightforward. Similar to the approach applied to the gas channel, the resulting differential form is further simplified by applying the definitions for the species and phase enthalpies, Eq. (C.9), as well as the corresponding species and mass balances, Eqs. (D.12), (D.23) and (D.24). Due to capillary effects a further enthalpy transport mechanism in addition to convection and Fickian diffusion appears in the energy balance via the capillary diffusion flux $\tilde{\psi}_{\mathrm{l}}$ by applying Eq. (26).

By means of characteristic reference quantities the nondimensional form of the energy balance for the GDL finally yields,

$$\begin{aligned}(1-\varepsilon)K_{\mathrm{E1}}\frac{\partial T}{\partial t} - K_{\mathrm{E8}}\frac{\partial}{\partial x_2}\left(k_{\mathrm{m}}\frac{\partial T}{\partial x_2}\right) + \varepsilon\rho_{\mathrm{m}}c_{\mathrm{m}}\left[\frac{\partial T}{\partial t} + \gamma_{\mathrm{c}}u_{\mathrm{m},2}\frac{\partial T}{\partial x_2}\right] + K_{\mathrm{E2}}\,\varepsilon\xi_{\mathrm{g}}^{\mathrm{H_2O}}\left[(1-s_{\mathrm{l}})\rho_{\mathrm{g}}\frac{\partial T_{\mathrm{sat}}}{\partial t} + (1-\zeta_{\mathrm{l}})\rho_{\mathrm{m}}u_{\mathrm{m},2}\frac{\partial T_{\mathrm{sat}}}{\partial x_2}\right] \\ = -K_{\mathrm{E3}}\,j_{\mathrm{g},2}^{\alpha}\frac{\partial T}{\partial t} - j_{\mathrm{g},2}^{\mathrm{H_2O}}\left[K_{\mathrm{E4}}\frac{\partial T}{\partial x_2} + K_{\mathrm{E2}}\frac{\partial T_{\mathrm{sat}}}{\partial x_2}\right] + \psi_{\mathrm{l},2}\left[\left(K_{\mathrm{E5}}c_{\mathrm{g}} - K_{\mathrm{E6}}\right)\frac{\partial T}{\partial x_2} + K_{\mathrm{E7}}\,\xi_{\mathrm{g}}^{\mathrm{H_2O}}\frac{\partial T_{\mathrm{sat}}}{\partial x_2}\right] \ ,\end{aligned} \tag{D.34}$$

where γ_{c} represents a correction factor for the advection of enthalpy

$$\gamma_{\mathrm{c}} = \frac{\zeta_{\mathrm{l}}c_{\mathrm{l}} + (1-\zeta_{\mathrm{l}})c_{\mathrm{g}}}{c_{\mathrm{m}}} \ . \tag{D.35}$$

Here, c_{g} denotes the (dimensionless) mass-averaged isobaric specific heat capacity of the gas phase.

D.6. Momentum balance

D.6.1. Gas channel

The integral formulation of the momentum conservation for a multiphase mixture under the assumption of homogeneous flow reads, [26],

$$\int_{\tilde{C}\tilde{V}} \frac{\partial(\tilde{\rho}_{\mathrm{m}}\tilde{\mathbf{u}}_{\mathrm{m}})}{\partial\tilde{t}}\,\mathrm{d}\tilde{V} + \oint_{\partial\tilde{C}\tilde{V}} \tilde{\rho}_{\mathrm{m}}\tilde{\mathbf{u}}_{\mathrm{m}}(\tilde{\mathbf{u}}_{\mathrm{m}}\cdot\mathbf{n})\,\mathrm{d}\tilde{S} = -\oint_{\partial\tilde{C}\tilde{V}} \tilde{p}\,\mathbf{n}\,\mathrm{d}\tilde{S} + \oint_{\partial\tilde{C}\tilde{V}} \tilde{\mu}_{\mathrm{g}}(\tilde{\nabla}\otimes\tilde{\mathbf{u}}_{\mathrm{m}} + (\tilde{\nabla}\otimes\tilde{\mathbf{u}}_{\mathrm{m}})^{T})\cdot\mathbf{n}\,\mathrm{d}\tilde{S} \ . \tag{D.36}$$

Note that friction forces only affect the continuous gas phase, consequently the gas mixture dynamic viscosity $\tilde{\mu}_{\mathrm{g}}$ appears in the last term rather than the multiphase mixture viscosity. Formally, the above equation is identical to the one used in the derivation of the model for isothermal single-phase conditions, except that the gas density and the gas velocity are replaced by their multiphase mixture counterparts. For a detailed derivation of the quasi-1D formulation of the equation of motion in the gas channel, the interested reader is referred to the original publication [23]. The non-dimensional governing equation of motion reads

$$\frac{\partial\rho_{\mathrm{m}}}{\partial t} + F_{\mathrm{u}}\frac{\partial(\rho_{\mathrm{m}}u_{\mathrm{m},1}^2)}{\partial x_1} + K_{\mathrm{M1}}\frac{\partial p}{\partial x_1} = -K_{\mathrm{M2}}\mu_{\mathrm{g}}u_{\mathrm{m},1} \ . \tag{D.37}$$

Here, F_{u} is a shape factor that accounts for the quadratic velocity term when performing cross-sectional averaging; for details see e.g. Spurk and Aksel [58].

D.6.2. Gas diffusion layer

The derivation of the equation of motion in the multiphase mixture model in capillary porous media is solely based on a simple Darcy law [38],

$$\frac{\partial\tilde{p}}{\partial\tilde{x}_2} = \frac{\tilde{\mu}_{\mathrm{m}}}{\tilde{\kappa}_{\perp}}\varepsilon\tilde{\rho}_{\mathrm{m}}\tilde{u}_{\mathrm{m},2} \ , \tag{D.38}$$

which neglects inertia and fluid friction effects, but allows a simple relationship between the multiphase mixture and the phase velocity, Eq. (26). In the model for isothermal single-phase conditions also inertia and friction terms are considered, and the pressure drop due to the GDL's porosity appears as an additional source term in the integral formulation of the momentum balance, see [23]. An order of magnitude estimate indicates that this term dominates due to the large ratio $\tilde{H}_{\mathrm{GDL}}^2/\tilde{\kappa}_{\perp} \gg 1$ between the square of the height and the hydraulic permeability of the GDL. It is therefore assumed, that the dimensionless equation of motion,

$$\frac{\partial\rho_{\mathrm{m}}}{\partial t} + \frac{\partial(\rho_{\mathrm{m}}u_{\mathrm{m},2}^2)}{\partial x_2} + K_{\mathrm{M1}}\frac{\partial p}{\partial x_2} = -K_{\mathrm{M2}}\,\mu_{\mathrm{m}}u_{\mathrm{m},2} + K_{\mathrm{M3}}\frac{\partial}{\partial x_2}\left(\mu_{\mathrm{m}}\frac{\partial u_{\mathrm{m},2}}{\partial x_2}\right) \ , \tag{D.39}$$

also holds in the context of the multiphase mixture model considered here.

It should also be noted that the source term $\tilde{S}_{\mathrm{phase}} = \tilde{m}_{\mathrm{l}}\tilde{u}_{2,\mathrm{r}}$ in the equation of motion accounting for momentum changes due to phase change processes is negligibly small compared to the Darcy term in the GDL [27,28]. In the gas channel, the magnitude of the phase change contribution is comparable with the other terms, as indicated by order of magnitude estimates. However, all simulations performed in the present work showed that the values of the (dimensionless) phase change rate turned out to be consistently extremely small, $|\dot{m}_{\mathrm{l}}| < 10^{-3}$. Consequently, the simplified equation of motion is considered sufficiently valid within the scope of the current model.

Data availability

Model-generated data are available on request. The model itself cannot be shared due to confidentiality agreements.

References

[1] Wang X, Ma Y, Gao J, Li T, Jiang G, Sun Z. Review on water management methods for proton exchange membrane fuel cells. Int J Hydrog Energy 2021;46(22):12206–29. http://dx.doi.org/10.1016/j.ijhydene.2020.06.211.

[2] Jiao K, Li X. Water transport in polymer electrolyte membrane fuel cells. Prog Energy Combust Sci 2011;37(3):221–91. http://dx.doi.org/10.1016/j.pecs.2010.06.002.

[3] Cai F, Cai S, Tu Z. Proton exchange membrane fuel cell (PEMFC) operation in high current density (HCD): Problem, progress and perspective. Energy Convers Manag 2024;307:118348. http://dx.doi.org/10.1016/j.enconman.2024.118348.

[4] Hu D, Wang Y, Li J, Yang Q, Wang J. Investigation of optimal operating temperature for the PEMFC and its tracking control for energy saving in vehicle applications. Energy Convers Manag 2021;249:114842. http://dx.doi.org/10.1016/j.enconman.2021.114842.

[5] Dafalla AM, Jiang F. Stresses and their impacts on proton exchange membrane fuel cells: A review. Int J Hydrog Energy 2018;43(4):2327–48. http://dx.doi.org/10.1016/j.ijhydene.2017.12.033.

[6] Yuan H, Dai H, Wei X, Ming P. Model-based observers for internal states estimation and control of proton exchange membrane fuel cell system: A review. J Power Sources 2020;468:228376. http://dx.doi.org/10.1016/j.jpowsour.2020.228376.

[7] Wang Y, Li H, Feng H, Han K, He S, Gao M. Simulation study on the PEMFC oxygen starvation based on the coupling algorithm of model predictive control and PID. Energy Convers Manag 2021;249:114851. http://dx.doi.org/10.1016/j.enconman.2021.114851.

[8] Vrlić M, Pernsteiner D, Schirrer A, Hametner C, Jakubek S. Reduced-dimensionality nonlinear distributed-parameter observer for fuel cell systems. Energy Rep 2023;10:1–14. http://dx.doi.org/10.1016/j.egyr.2023.06.006.

[9] Fuchs B, Altmann F, Vrlić M, et al. Nonlinear distributed-parameter observer design for efficient estimation of internal temperature profiles in polymer electrolyte membrane fuel cells. Nonlinear Dynam 2025. http://dx.doi.org/10.1007/s11071-025-11108-0.

[10] Amphlett JC, Mann RF, Peppley BA, Roberge PR, Rodrigues A. A model predicting transient responses of proton exchange membrane fuel cells. J Power Sources 1996;61(1):183–8. http://dx.doi.org/10.1016/S0378-7753(96)02360-9.

[11] Sankar K, Aguan K, Jana AK. A proton exchange membrane fuel cell with an airflow cooling system: Dynamics, validation and nonlinear control. Energy Convers Manag 2019;183:230–40. http://dx.doi.org/10.1016/j.enconman.2018.12.072.

[12] Kim Y-B. Improving dynamic performance of proton-exchange membrane fuel cell system using time delay control. J Power Sources 2010;195(19):6329–41. http://dx.doi.org/10.1016/j.jpowsour.2010.04.042.

[13] Abdin Z, Webb C, Gray E. PEM fuel cell model and simulation in Matlab–Simulink based on physical parameters. Energy 2016;116:1131–44. http://dx.doi.org/10.1016/j.energy.2016.10.033.

[14] Tao J, Wei X, Ming P, Wang X, Jiang S, Dai H. Order reduction, simplification and parameters identification for cold start model of PEM fuel cell. Energy Convers Manag 2022;274:116465. http://dx.doi.org/10.1016/j.enconman.2022.116465.

[15] del Real AJ, Arce A, Bordons C. Development and experimental validation of a PEM fuel cell dynamic model. J Power Sources 2007;173(1):310–24. http://dx.doi.org/10.1016/j.jpowsour.2007.04.066.

[16] Fu H, Shen J, Sun L, Lee KY. Fuel cell humidity modeling and control using cathode internal water content. Int J Hydrog Energy 2021;46(15):9905–17. http://dx.doi.org/10.1016/j.ijhydene.2020.04.283.

[17] Ziegler C, Yu HM, Schumacher JO. Two-phase dynamic modeling of PEMFCs and simulation of cyclo-voltammograms. J Electrochem Soc 2005;152(8):A1555. http://dx.doi.org/10.1149/1.1946408.

[18] Siegel JB. Experiments and modeling of PEM fuel cells for dead-ended anode operation [Ph.D. thesis], University of Michigan; 2010.

[19] Goshtasbi A, García-Salaberri P, Chen J, Talukdar K, Sanchez DG, Ersal T. Through-the-membrane transient phenomena in PEM fuel cells: A modeling study. J Electrochem Soc 2019;166(7):F3154–68. http://dx.doi.org/10.1149/2.0181907jes.

[20] Kang S. Quasi-three dimensional dynamic modeling of a proton exchange membrane fuel cell with consideration of two-phase water transport through a gas diffusion layer. Energy 2015;90:1388–400. http://dx.doi.org/10.1016/j.energy.2015.06.076.

[21] Kravos A, Kregar A, Penga Z, Barbir F, Katrašnik T. Real-time capable transient model of liquid water dynamics in proton exchange membrane fuel cells. J Power Sources 2022;541:231598. http://dx.doi.org/10.1016/j.jpowsour.2022.231598.

[22] Dannenberg K, Ekdunge P, Lindbergh G. Mathematical model of the PEMFC. J Appl Electrochem 2000;30(12):1377–87. http://dx.doi.org/10.1023/A:1026534931174.

[23] Murschenhofer D, Kuzdas D, Braun S, Jakubek S. A real-time capable quasi-2D proton exchange membrane fuel cell model. Energy Convers Manag 2018;162:159–75. http://dx.doi.org/10.1016/j.enconman.2018.02.028.

[24] Wang B, Wu K, Yang Z, Jiao K. A quasi-2D transient model of proton exchange membrane fuel cell with anode recirculation. Energy Convers Manag 2018;171:1463–75. http://dx.doi.org/10.1016/j.enconman.2018.06.091.

[25] Altmann F. On multiphase flow and the dynamic temperature distribution in proton exchange membrane fuel cells [M.S. thesis], TU Wien; 2022, http://dx.doi.org/10.34726/hss.2022.96214.

[26] Brennen CE. Fundamentals of multiphase flow. Cambridge: Cambridge University Press; 2005, http://dx.doi.org/10.1017/CBO9780511807169.

[27] Gurau V, Edwards RV, Mann JA, Zawodzinski TA. A look at the multiphase mixture model for PEM fuel cell simulations. Electrochem Solid-State Lett 2008;11(8):B132. http://dx.doi.org/10.1149/1.2929658.

[28] Wang C-Y. Comment on "A look at the multiphase mixture model for PEM fuel cell simulations" [Electrochem. Solid-State Lett. , 11, B132 (2008)]. Electrochem Solid-State Lett 2008;12(2):S2. http://dx.doi.org/10.1149/1.3041157.

[29] Gurau V. Response to "Comment on 'A look at the multiphase mixture model for PEM fuel cell simulations'" [Electrochem. Solid-State Lett., 11, B132 (2008)]. Electrochem Solid-State Lett 2008;12(2):S4. http://dx.doi.org/10.1149/1.3041657.

[30] Taylor R, Krishna R. Multicomponent mass transfer. New York, NY: John Wiley & Sons; 1993.

[31] Fuller EN, Schettler PD, Giddings JC. New method for prediction of binary gas-phase diffusion coefficients. Ind Eng Chem 1966;58(5):18–27. http://dx.doi.org/10.1021/ie50677a007.

[32] Fink C. Modelling and simulation of multiphase transport phenomena in porous media with application to PEM fuel cells [Ph.D. thesis], TU Graz; 2009.

[33] Ziegler C. Modeling and simulation of the dynamic behavior of portable proton exchange membrane fuel cells [Ph.D. thesis], Universität Konstanz; 2005.

[34] Springer TE, Zawodzinski TA, Gottesfeld S. Polymer electrolyte fuel cell model. J Electrochem Soc 1991;138(8):2334–42. http://dx.doi.org/10.1149/1.2085971.

[35] Baehr HD, Stephan K. Heat and mass transfer. 2nd ed.. Berlin, Germany: Springer; 2006, http://dx.doi.org/10.1007/3-540-29527-5.

[36] Kulikovsky AA. Analytical modelling of fuel cells. Amsterdam, Netherlands: Elsevier; 2010, http://dx.doi.org/10.1016/B978-0-444-53560-3.00019-3.

[37] Hill A, Straughan B. Poiseuille flow in a fluid overlying a highly porous material. Adv Water Resour 2009;32(11):1609–14. http://dx.doi.org/10.1016/j.advwatres.2009.08.007.

[38] Wang C, Cheng P. A multiphase mixture model for multiphase, multicomponent transport in capillary porous media—I. Model development. Int J Heat Mass Transfer 1996;39(17):3607–18. http://dx.doi.org/10.1016/0017-9310(96)00036-1.

[39] Leverett MC. Capillary behavior in porous solids. Trans AIME 1941;142:152–69. http://dx.doi.org/10.2118/941152-G.

[40] Ramousse J, Lottin O, Didierjean S, Maillet D. Heat sources in proton exchange membrane (PEM) fuel cells. J Power Sources 2009;192(2):435–41. http://dx.doi.org/10.1016/j.jpowsour.2009.03.038.

[41] Burheim O, Vie P, Pharoah J, Kjelstrup S. Ex situ measurements of through-plane thermal conductivities in a polymer electrolyte fuel cell. J Power Sources 2010;195(1):249–56. http://dx.doi.org/10.1016/j.jpowsour.2009.06.077.

[42] Barbir F. PEM fuel cells: Theory and practice. 2nd ed.. San Diego, CA: Academic Press; 2012.

[43] Cao T-F, Mu Y-T, Ding J, Lin H, He Y-L, Tao W-Q. Modeling the temperature distribution and performance of a PEM fuel cell with thermal contact resistance. Int J Heat Mass Transfer 2015;87:544–56. http://dx.doi.org/10.1016/j.ijheatmasstransfer.2015.04.010.

[44] Ge S, Li X, Yi B, Hsing I-M. Absorption, desorption, and transport of water in polymer electrolyte membranes for fuel cells. J Electrochem Soc 2005;152:A1149. http://dx.doi.org/10.1149/1.1899263.

[45] Trefethen LN. Spectral methods in MATLAB. Philadelphia, PA: Society for Industrial and Applied Mathematics; 2000, http://dx.doi.org/10.1137/1.9780898719598.

[46] Scheichl S, Braun S, Kluwick A. On a similarity solution in the theory of unsteady marginal separation. Acta Mech 2008;201(1):153–70. http://dx.doi.org/10.1007/s00707-008-0079-6.

[47] Sheu TWH, Lin RK. Newton linearization of the incompressible Navier–Stokes equations. Internat J Numer Methods Fluids 2004;44(3):297–312. http://dx.doi.org/10.1002/fld.639.
[48] The MathWorks, Inc. MATLAB version R2022a. Natick, Massachusetts: The MathWorks, Inc.; 2022, URL https://www.mathworks.com.
[49] AVL List GmbH. AVL FIRE™ M user manual R2023.1. 2023, URL https://www.avl.com/en/simulation-solutions/software-offering/simulation-tools-a-z/avl-fire-m.
[50] Fink C, Gößling S, Karpenko-Jereb L, Urthaler P. CFD simulation of an industrial PEM fuel cell with local degradation effects. Fuel Cells 2020;20(4):431–52. http://dx.doi.org/10.1002/fuce.201900197.
[51] Fink C, Fouquet N. Three-dimensional simulation of polymer electrolyte membrane fuel cells with experimental validation. Electrochim Acta 2011;56(28):10820–31. http://dx.doi.org/10.1016/j.electacta.2011.05.041.
[52] Benkovic D, Fink C, Iranzo A. Qualitative and quantitative determination of liquid water distribution in a PEM fuel cell. Int J Hydrog Energy 2024;52:1360–70. http://dx.doi.org/10.1016/j.ijhydene.2023.09.161.
[53] Karpenko-Jereb L, Sternig C, Fink C, Hacker V, Theiler A, Tatschl R. Theoretical study of the influence of material parameters on the performance of a polymer electrolyte fuel cell. J Power Sources 2015;297:329–43. http://dx.doi.org/10.1016/j.jpowsour.2015.07.011.
[54] The MathWorks, Inc. Global optimization toolbox: User's guide. Natick, Massachusetts: The MathWorks, Inc.; 2024, URL https://www.mathworks.com/help/gads/particle-swarm-optimization-algorithm.html.
[55] Wang Y, Wang C-Y. Transient analysis of polymer electrolyte fuel cells. Electrochim Acta 2005;50(6):1307–15. http://dx.doi.org/10.1016/j.electacta.2004.08.022.
[56] Wang Q, Tang F, Li B, Dai H, Zheng JP, Zhang C, Ming P. Study on the thermal transient of cathode catalyst layer in proton exchange membrane fuel cell under dynamic loading with a two-dimensional model. Chem Eng J 2022;433:133667. http://dx.doi.org/10.1016/j.cej.2021.133667.
[57] Wang Q, Tang F, Li B, Dai H, Zheng JP, Zhang C, Ming P. Numerical analysis of static and dynamic heat transfer behaviors inside proton exchange membrane fuel cell. J Power Sources 2021;488:229419. http://dx.doi.org/10.1016/j.jpowsour.2020.229419.
[58] Spurk JH, Aksel N. Fluid nechanics. 2nd ed.. Berlin, Germany: Springer; 2008.
[59] Stephan P, Kabelac S, Kind M, Mewes D, Schaber K, Wetzel T, editors. VDI-Wärmeatlas. 12th ed.. Berlin Heidelberg: Springer Vieweg; 2019, http://dx.doi.org/10.1007/978-3-662-52989-8.
[60] National Institute of Standards and Technology. Thermophysical properties of fluid systems. 2025, https://webbook.nist.gov/chemistry/fluid/. [Accessed 1 April 2025].
[61] Wu H, Li X, Berg P. On the modeling of water transport in polymer electrolyte membrane fuel cells. Electrochim Acta 2009;54(27):6913–27. http://dx.doi.org/10.1016/j.electacta.2009.06.070.